

Development of Engineered Magnetic Materials for Antenna Applications

by

Kevin Buell

A dissertation submitted in partial fulfillment
of the requirements for the degree of
Doctor of Philosophy
(Electrical Engineering)
in The University of Michigan
2005

Doctoral Committee:

Professor Kamal Sarabandi, Chair
Professor John W. Halloran
Professor Anthony W. England
Associate Professor Amir Mortazawi

© Kevin Buell 2005
All Rights Reserved

To my father whose accomplishments have made my successes possible.

ACKNOWLEDGEMENTS

The secret to creativity is knowing how to hide your sources.

Albert Einstein

Personally, I prefer recognizing here those to whom my success is more rightfully attributed.

First, and most importantly- I must acknowledge my mother, who taught me to believe in myself. Thank you, Mom.

I would like to acknowledge the support, guidance and encouragement provided by Ronald Guttman, the professor for my undergraduate microwave engineering course at Rensselaer Polytechnic Institute (RPI) and the reason I chose this field of study. Doctor Guttman was a teacher, a mentor, and a friend.

Of course, I also must acknowledge the support and guidance of my doctoral committee; Kamal Sarabandi, John Halloran, Anthony England, and Amir Mortazawi. Of particularly outstanding value has been the guidance of my Kamal Sarabandi, my committee chairman.

Doctor Sarabandi is truly a genius of the first order and perhaps the most intelligent person I have ever met. Many times during my doctoral studies I have felt like a child playing in the shadow of a giant. This gentle giant has sheltered me and guided me through numerous technological mine fields, using the trip to teach me and help me develop my own understanding of Electromagnetics in particular and research in a broader sense. For this I am immeasurably grateful.

Originally it was intended for Doctor Hossein Mosallaei to be a member of my thesis committee. As he has left the University of Michigan to accept a teaching position at Northeastern University, he is no longer officially a member of my committee. Nonetheless, he should be recognized as having served as a virtual co-advisor for the last years of my research. It was work supervised by Doctor Sarabandi and Doctor Mosallaei for which I have twice been recognized with the IEEE Antennas and Propagation Society *Best Student Paper* award in 2003 and 2005, the only student ever so honored. I could not have done it without him.

I have been extremely fortunate to receive generous financial support from numerous sources. First, I would also acknowledge the financial support of the University of Michigan and the National Science Foundation for the joint fellowship which initiated and sustained my doctoral studies for the majority of my graduate career. The second major source of support which I wish to recognize is the Motorola corporation whose fellowship funded me for the 2001-2002 academic year. Finally, the Intel Foundation PhD Fellowship has generously funded the final year of my Doctoral research during the 2004-2005 academic year and perhaps as importantly has provided me with mentoring by the Intel CTO.

TABLE OF CONTENTS

DEDICATION	ii
ACKNOWLEDGEMENTS	iii
LIST OF TABLES	viii
LIST OF FIGURES	ix
CHAPTERS	
1 Introduction	1
1.1 Overview	1
1.2 Background	2
1.3 Method	5
1.4 Applications of Magneto-Dielectrics	7
1.4.1 Elements of Research; Material Development, Characterization, and Application	20
1.5 Chapter Outline	21
1.5.1 Chapter 1: Introduction	21
1.5.2 Chapter 2: Natural Magnetic Materials	21
1.5.3 Chapter 3: Metamaterials	22
1.5.4 Chapter 4: Material Characterization	22
1.5.5 Chapter 5: A miniaturized Patch Antenna on Magnetic Metamaterial Substrate	24
1.5.6 Chapter 6: Patch Antenna over Reactive Impedance Surface	25
1.5.7 Chapter 7: Electromagnetic MetaMaterial Insulator	25
1.5.8 Chapter 8: Metamaterial Insulator enabled Superdirective Array	26
1.5.9 Chapter 9: Conclusion	26
2 Natural Magnetic Materials	27
2.1 Chapter Introduction	27
2.2 Understanding Natural Magnets	28
2.3 New Advances in Natural Magnets	34

2.3.1	Application of Impedance Matched Materials	34
2.3.2	Z-Phase Hexaferrite	42
2.4	Chapter Conclusions	42
3	Metamaterials	44
3.1	Chapter Introduction	44
3.2	Meta-Materials Background	45
3.2.1	The split ring resonator for permeability (μ_r)	45
3.2.2	The metallic dipole for permittivity (ϵ_r)	48
3.2.3	Left-Handed Medium and the Negative Index of Refraction	48
3.3	Embedded Circuit Spiral Resonator Metamaterial	50
3.3.1	Benefits of Magnetic Materials	51
3.3.2	Embedded Circuit Meta-Materials	54
3.3.3	Effective Medium Operation	56
3.3.4	Equivalent Circuit Model	57
3.4	Chapter Conclusions	73
4	Material Characterization	74
4.1	Chapter Introduction	74
4.2	Waveguide Characterization Toolkit	75
4.2.1	Effectiveness of the waveguide characterization toolkit	80
4.3	Resonant Cavity Method	81
4.3.1	Frequency Extended Perturbation Technique	85
4.3.2	Hybrid Perturbation Technique	92
4.4	A comment on Measuring Anisotropic materials	103
4.5	Chapter Conclusions	105
5	A miniaturized Patch Antenna on Magnetic Metamaterial Substrate	107
5.1	Chapter Introduction	107
5.2	Metamaterial Design and Fabrication	108
5.3	Metamaterial Performance	110
5.3.1	Antenna Performance	114
5.4	Chapter Conclusions	121
6	Patch Antenna Over Reactive Impedance Surface	123
6.1	Chapter Introduction	123
6.2	Motivation	124
6.3	Patch Antenna over the RIS Substrate	124
6.4	Fabrication	134
6.5	Measurement	134
6.6	Chapter Conclusions	136
7	Electromagnetic MetaMaterial Insulator	138
7.1	Chapter Introduction	138

7.1.1	Preview of Metamaterial Insulators	138
7.2	Theory of Metamaterial Insulators	139
7.3	Theoretical Isolation Performance	142
7.4	Metamaterial Insulator Design, Fabrication, and Measurement	146
7.5	Improving Isolation Bandwidth	148
7.6	Chapter Conclusions	149
8	Metamaterial Insulator Enabled Superdirective Array	152
8.1	Chapter Introduction	152
8.2	Motivation and Background	153
8.2.1	Superdirectivity	154
8.2.2	Patch Coupling	155
8.2.3	Sensitivity Factor	155
8.2.4	Scan Blindness	157
8.3	Design for Superdirective Beam-Forming	158
8.3.1	Single Element	158
8.3.2	Linear Array	159
8.4	Array Measurement	163
8.4.1	Comment on the choice of excitation coefficients . . .	164
8.5	Limits of Superdirectivity	165
8.5.1	Efficiency	165
8.6	Chapter Conclusions	167
9	Conclusion	169
9.1	Summary of Results	169
9.2	Future Work	172
9.3	Closing Thoughts	172
	APPENDIX	173
	BIBLIOGRAPHY	177

LIST OF TABLES

Table

2.1	Diamagnetic Materials	30
2.2	Paramagnetic Materials	30
2.3	Ferromagnetic Materials	31
2.4	AntiFerromagnetic Materials	32
2.5	Impedance Matched Material Embedded Four-Point Antenna	42
4.1	Teflon Measurement	80
4.2	Measured Permittivity and Permeability of Materials	103
4.3	Measured Loss Factors of Aluminum-Oxide	103
5.1	Antenna Parameters	117
5.2	Miniaturization and Efficiency	117

LIST OF FIGURES

Figure

1.1	Incomplete magnetic spin cancelation in magnetite (Fe_3O_4) resulting in a net magnetism	6
1.2	Probe Fed Microstrip Patch Antenna on a High Permittivity Substrate $\epsilon_r = 25.0$ $\tan\delta_e=0.001$	8
1.3	The Impedance bandwidth of probe Fed Microstrip Patch Antenna on a High Permittivity Substrate $\epsilon_r = 25.0$ is 0.64% and exhibits a low ($\eta=77\%$) efficiency.	8
1.4	Radiation Pattern of antenna in Figure 1.2. Notice that the pattern is highly symmetric in E and H planes.	9
1.5	Probe Fed Microstrip Patch Antenna on an Impedance Matched Magneto-Dielectric Substrate $\epsilon_r = \mu_r = 5.0$ $\tan\delta_e = \tan\delta_m=0.001$	12
1.6	The Impedance bandwidth of probe Fed Microstrip Patch Antenna on an Impedance Matched Magneto-Dielectric Substrate $\epsilon_r = \mu_r = 5.0$ is 7.94% and exhibits a high ($\eta=99\%$) efficiency.	13
1.7	Radiation Pattern of antenna in Figure 1.5.	13
1.8	High Permittivity Dielectric Resonator Antenna ($L_x=L_y=0.15\lambda_0=26.67\text{mm}$, $L_z=0.091\lambda_0=6.67\text{mm}$) $\epsilon_r = 25.0$, $\mu_r = 1.0$ $\tan\delta_e=0.001, \tan\delta_m=0$	14
1.9	The Impedance bandwidth of probe Fed High Permittivity DRA $\epsilon_r = 25.0$ is 2.75% and exhibits a low ($\eta=77\%$) efficiency.	15
1.10	Radiation Pattern of DRA in Figure 1.8.	15
1.11	Magneto-Dielectric Resonator Antenna ($L_x=L_y=0.15\lambda_0=26.67\text{mm}$, $L_z=0.091\lambda_0=6.67\text{mm}$) $\epsilon_r = 5.0$, $\mu_r = 5.0$ $\tan\delta_e=\tan\delta_m=0.001$	16
1.12	The Impedance bandwidth of probe Magneto-Delectric Resonator Antenna ($\epsilon_r = 5.0, \mu_r = 5.0$) is 12.08%	16
1.13	Radiation Pattern of MDRA in Figure 1.11.	17
1.14	A 'woodpile' structure of permeable ($\epsilon_r=1, \mu_r=16$) and dielectric ($\epsilon_r=16, \mu_r=1$) materials stacked in alternation to achieve an electromagnetic band-gap phenomenon.	18
1.15	Transmission through a dielectric-air woodpile, a permeable-air woodpile, and a dielectric-permeable woodpile.	19

2.1	The permeability of natural materials is caused by either the orbital or electron spin magnetic moment. Of the two, the electronic spin magnetic moment is much stronger and when present and uncanceled is the source of observable magnetic properties.	29
2.2	The Spin Magnetic Moment of Diamagnetic materials with no applied field and in the presence of an externally applied magnetic field. . .	30
2.3	The Spin Magnetic Moment of Paramagnetic materials in with no applied field and in the presence of an externally applied magnetic field.	31
2.4	The Spin Magnetic Moment of Ferromagnetic materials in the absence of an applied magnetic field.	33
2.5	The Spin Magnetic Moment of AntiFerromagnetic materials in the absence of an applied magnetic field.	34
2.6	Magnetic permeability of yttrium and calcium-vanadium garnets in the region below and around resonance.	35
2.7	Magnetic loss levels of yttrium and calcium-vanadium garnets in the region below and around resonance.	36
2.8	Simplified 2D structure of Magnetite.	37
2.9	Magnetite structure in 3D.	37
2.10	The four point antenna is a crossed bow-tie antenna developed by the Virginia Tech Antenna Group.	38
2.11	The four point antenna one quarter wavelength above a PEC ground plane.	39
2.12	The four point antenna embedded in an impedance matched material block.	40
2.13	The impedance bandwidths of a four-point antenna embedded in impedance matched materials.	41
2.14	The radiation patterns of a four-point antenna embedded in impedance matched materials.	41
2.15	The permeability of the Z-phase hexaferrite was measured and found to be non-dispersive below approx 500 Mhz. The measurement also showed that it is low-loss.	43
3.1	The split-ring resonator proposed by Pendry et. al. ([1]).	45
3.2	The unit-cell geometry for an isotropic split-ring resonator metamaterial.	46
3.3	Complex Permeability of a bulk medium composed of split-ring resonator metamaterials.	47
3.4	In most natural materials at microwave frequencies both ϵ_r and μ_r are positive.	49
3.5	A medium with metallic inclusions in the shape of the greek letter "omega". The "omega" medium exhibits enhancement of both the magnetic and dielectric properties over the host material in certain frequency regions, determined by the circuit resonances.	55

3.6	The metamaterial unit cell. Δ_x , Δ_y , and Δ_z is the unit cell size. In this diagram $N = 2$ is the number of wraps of the spiral. To achieve permeability enhancement, the magnetic field shall be aligned along the Y axis (normal to the page) and the electric field shall align along either the X or Z axis.	57
3.7	Infinite Metamaterial Medium. A passive 2D XZ array of elements shown in Fig. 5.2. These circuit boards can be stacked in the Y dimension to approximate an infinite magnetic medium.	59
3.8	Previous Magnetic embedded circuits A) Split-Ring Resonator B) Square LC Resonator C) 'Omega' Medium Resonator.	59
3.9	The spiral loop equivalent lumped-element circuit model.	61
3.10	Transmission-line equivalent model for magnetic metamaterial.	61
3.11	Geometry for (3.5) to calculate capacitance of two flat coplanar metallic strips.	63
3.12	The air gap caused by substrate warpage decreases the effective capacitance of the spiral resonator, increasing the metamaterial resonance frequency.	65
3.13	A higher order spiral loop equivalent circuit model.	67
3.14	FEM boundary conditions to test resonance frequency.	68
3.15	Relative Permittivity, and Permeability of metamaterial. At 250 MHz $\epsilon_{r(meta)} = 9.8$, $\mu_{r(meta)} = 3.1$, and $Tan\delta_m$ 0.014.	69
3.16	Patch antenna over Magnetic Metamaterial Substrate. Length ' L_{patch} ' is the resonant length and indicates orientation of radiating current.	72
4.1	Sample under test in waveguide.	75
4.2	Sample position and thickness are variables in the material characterization equations.	76
4.3	Comparison of predicted and measured scattering parameters for sample material (Teflon). The good match indicates that the material characterization properties determined by the waveguide toolkit are accurate.	81
4.4	The electric field distribution in a short cavity (TM010 Dominant mode). The maximum electric field magnitude is at the cavity center.	82
4.5	The magnetic field distribution in a short cavity (TM010 Dominant mode). The maximum magnetic field magnitude is near the cavity edge.	83
4.6	Cavity response (S21) of a resonant cavity when empty and when perturbed by a dielectric (teflon) sample.	87
4.7	Dielectric constant of Teflon, measured by the frequency extended perturbation method.	88
4.8	The permittivity and permeability of an embedded circuit resonator predicted by the models developed in this thesis.	88

4.9	The system response of an empty cavity is compared to the perturbed response due to an embedded-circuit metamaterial resonator sample predicted by 4.15. The prediction is validated by HFSS simulations.	89
4.10	The permeability determined by 4.17 from the HFSS simulations is compared to the permeabilities used for those simulations.	90
4.11	Embedded Circuit Resonator Metamaterial.	91
4.12	The dispersive metamaterial permeability measured by the FEPM is compared to that predicted by the metamaterial model.	92
4.13	Flowchart showing the steps of the hybrid characterization method.	96
4.14	Percent shift shift in resonant frequency with sample in a cavity, for various possible material permittivities and permeabilities.	97
4.15	Shift shift in Q-factor with sample in a cavity, for various possible material electric and magnetic loss factors.	99
4.16	Electrical currents on the wall and lid of a cylindrical cavity in TM ₀₁₀ mode.	100
4.17	Employing a Choke-Flange significantly improves cavity Q-factor, and the accuracy of material loss factor measurement.	101
4.18	Stacked isotropic layers are examples of uniaxial anisotropies.	105
5.1	2x24 cm strip of RO-4003 with 12 resonant loop unit cells	108
5.2	The metamaterial unit cell. Δ_x , Δ_y , and Δ_z is the unit cell size. In this diagram $N = 2$ is the number of wraps of the spiral. To achieve permeability enhancement, the magnetic field shall be aligned along the Y axis (normal to the page) and the electric field shall align along either the X or Z axis.	109
5.3	Free space Transmissivity/Reflectivity test of metamaterial substrate to identify resonance frequency.	111
5.4	Relative Permittivity, and Permeability of metamaterial. At 250 MHz $\epsilon_{r(meta)} = 9.8$, $\mu_{r(meta)} = 3.1$, and $Tan\delta_m$ 0.014.	112
5.5	Miniaturized microstrip patch antenna on a magnetic metamaterial substrate operating at 250 MHz. The resonant length $L_{patch} = 0.077\lambda = 9.3cm$	115
5.6	Electric and Magnetic field configurations in region beneath microstrip patch antenna. The electric field is aligned along the Z axis and the magnetic field is aligned along the Y axis normal to the page as shown.	115
5.7	Measured antenna gain pattern for patch antenna over magnetic metamaterial substrate at 250 MHz.	118
5.8	Return loss at 250 MHz for probe-fed patch antenna over magnetic metamaterial substrate.	119
5.9	Radiation Efficiency of a patch at 250 MHz verses substrate material loss tangent on modeled metamaterial substrate.	121
6.1	A Reactive Impedance Surface (RIS) composed of small metallic patches over a PEC backed dielectric substrate.	125
6.2	A Reactive Impedance Surface (RIS) Unit Cell.	126

6.3	Capacitance between Reactive Impedance Surface (RIS) Unit Cells.	126
6.4	A Parallel Inductive effect from the phase delay of the traveling through the underlying substrate.	127
6.5	The equivalent circuit model for the parallel capacitance and inductance in a RIS.	127
6.6	Normalized Surface Impedance at Normal Incidence	128
6.7	Normalized Surface Impedance at Oblique Incidence	129
6.8	RIS Surface impedance for 1.86 GHz patch antenna.	131
6.9	Impedance bandwidth of patch antenna over RIS and equivalent conventional substrate.	132
6.10	Radiation pattern for miniaturized patch over RIS.	133
6.11	The elements of the RIS patch antenna.	135
6.12	The final assembled Patch antenna on RIS.	136
6.13	Experimentally measured impedance bandwidth	137
6.14	Experimentally measured radiation Pattern	137
7.1	Embedded Circuit (EC) Metamaterial Resonators consist of a planar metalized spiral in a dielectric host medium. The insulator operating frequency is tuned by the spiral resonance and for our design the insulators are $0.05\lambda_0$	140
7.2	The anisotropic permittivity (ϵ_{reff}) and permeability (μ_{reff}) exhibit a band-stop region immediately above resonance when $\mu_{reff} < 0$ and $\epsilon_{reff} > 0$	141
7.3	The transmission (S21) and reflection (S11) at an infinite wall clearly shows an insulating region where nearly all the energy is reflected. This occurs immediately above the 2.0 Ghz spiral resonance	142
7.4	Source and observation points on a high dielectric substrate. Metamaterial insulator are shown half-way between the source and observation points, d/λ_0 from each.	143
7.5	Magnitude of electric field induced at the observation point in Figure 7.4.	144
7.6	Two adjacent patches aligned to produce a strong trapped substrate wave and maximize mutual coupling. The insulator wall of spiral resonators suppresses this coupling	145
7.7	With the insulators removed, on a solid substrate the coupling (S21) between the two adjacent probe feeds is strong. The input matching (S11) indicates a well tuned patch.	146
7.8	When the insulators are returned, a slight shift in resonant frequency occurs but the input matching (S11) is still good. More importantly, the insulators provide excellent suppression of mutual coupling (S21).	147
7.9	Embedded Circuit Metamaterial Resonators designed for a 2.0 GHz resonant frequency.	148
7.10	A physical experiment similar to the simulation of Fig. 7.6 for validating the effectiveness of metamaterial insulators.	149

7.11	The input matching (S11) and mutual coupling (S21) of the two patches in Fig. 7.10 with metamaterial insulators removed, leaving an air-gap between substrates.	150
7.12	The input matching (S11) and mutual coupling (S21) of the two patches in Fig. 7.10 with metamaterial insulators. Even without tuning, the metamaterial insulators provide excellent suppression of mutual coupling.	150
7.13	Typical insulation provided by an infinite wall of EC spirals. The -10dB isolation bandwidth is more than doubled by adding a second isolation layer tuned to a slightly different frequency.	151
8.1	Coupling: Scattering parameter S21 measured at the feed ports of two patches in an E-plane orientated array, simulated for various spatial periods.	156
8.2	A patch antenna between metamaterial insulators is the basic antenna element which will be used to build a densely-packed antenna array. The insulators contain the energy in the local region, improving front-to-back ratio of the individual antenna and preventing mutual coupling in densely packed arrays.	158
8.3	A densely packed five element linear patch array $1.18\lambda_0$ with metamaterial insulators to suppress mutual coupling	159
8.4	The calculated E-field pattern of the array in Fig. 8.3 under uniform excitation and a squinted (superdirective) beam. The response of an ideal 5-element array of isotropic radiators of the same geometry is included for reference	160
8.5	The lowest possible SideLobe Level for a given (first null) beamwidth is plotted as the solid line. Several optimized sidelobe levels for a given beamwidth achievable for our metamaterial insulator enabled array is indicated for several beamwidths	162
8.6	Simulations of Anti-Jamming null placement directly at broadside can readily provide 40 dB nulls, with -10dB jamming suppression across a 20 degree beamwidth. Reception in the remainder of the array field of view remains good.	163
8.7	The anti-jamming null can be steered to any angle while maintaining an excellent near-isotropic reception pattern in the alternate hemisphere of the antenna field of view	164
8.8	$1.18\lambda_0$ five-element metamaterial enabled patch array for 2GHz operation	168
8.9	The broadside main-beam exhibits superdirectivity at 2.12GHz. Although the antennas and feed network were design for 2.0 GHz, metamaterial insulators resonated at 2.1GHZ, so the array was measured untuned in the insulating region at 2.12GHz.	168

CHAPTER 1

Introduction

*If we knew what it was we were doing, it would not be called
research, would it?*

Albert Einstein

1.1 Overview

The purpose of this research is to develop new materials with desirable electromagnetic properties that are not currently available to microwave engineers. One unifying theme of the materials that we have investigated is that these new materials should be moderately low loss magnetic materials for microwave applications. Specific properties we have investigated are impedance matched materials, tuned enhanced permeability, reactive impedance surfaces, and negative permeability electromagnetic band-gap materials. The development of new, superior antennas is the application employed to prove these new materials. In this chapter, preliminary evidence which indicated that pursuing such an endeavor would be promising is considered.

Both natural and engineered materials are considered. In the natural regime, composite materials whose processing allows us to push the limits of currently available materials are investigated. It is generally the case that natural materials are unacceptably high-loss in the microwave region or possess no magnetic properties

whatsoever. It to be possible that modern composites of magnetic materials exist whose low-loss magnetic properties by proper processing can be extended into the microwave region .

For engineered materials, a much more exciting possibility exists. It is possible to achieve magnetic permeability in an otherwise non-magnetic material by employing electromagnetically small embedded-circuit inclusions. By tailoring the parameters of these embedded-circuits, it should be possible to control the magnetic properties of the effective medium.

For engineered surfaces, fully-reflecting purely reactive impedance surfaces offer the intriguing possibility of tunable reflections optimized for their particular application.

Once a material suspected to possess desirable magnetic properties is identified, then its magnetic properties must be tested and characterized. To meet this need new methods and tools are developed which are appropriate for characterizing magnetic materials in the microwave region.

Lastly, several antennas and arrays designed with these new materials whose properties appear promising were created and tested to determine the utility of these materials to solving real engineering problems.

1.2 Background

The Maxwell Equations describe electromagnetic field behavior in terms of electric and magnetic intensities and their respective flux densities. Electric charge and the electric current which results from charge motion are ultimately the source of all electromagnetic fields and are included as the source terms in the Maxwell Equations.

$$\nabla \cdot \mathbf{D}(\vec{r}, t) = \rho(\vec{r}, t) \quad (1.1)$$

$$\nabla \times \mathbf{E}(\vec{r}, t) = -\frac{\delta}{\delta t} \mathbf{B}(\vec{r}, t) \quad (1.2)$$

$$\nabla \cdot \mathbf{B}(\vec{r}, t) = 0 \quad (1.3)$$

$$\nabla \times \mathbf{H}(\vec{r}, t) = \mathbf{J}(\vec{r}, t) + \frac{\delta}{\delta t} \mathbf{D}(\vec{r}, t) \quad (1.4)$$

Equations 1.1-1.4 are the most general differential form of Maxwell's Equations in three-dimensional vector notation. This form is valid at all points in space, under all circumstances. If the time-harmonic condition is assumed, and positional notation \vec{r} is suppressed, the differential point-form of Maxwell's Equations may be integrated over a space or volume to yield equations 1.5-1.8.

$$\oint_s \mathbf{D} \cdot d\mathbf{S} = Q \quad (1.5)$$

$$\oint_c \mathbf{E} \cdot d\mathbf{L} = -\int_s \frac{\delta \mathbf{B}}{\delta t} \cdot d\mathbf{S} \quad (1.6)$$

$$\oint_s \mathbf{B} \cdot d\mathbf{S} = 0 \quad (1.7)$$

$$\oint_c \mathbf{H} \cdot d\mathbf{L} = \int_s (\mathbf{J} + \frac{\delta \mathbf{D}}{\delta t}) \cdot d\mathbf{S} \quad (1.8)$$

From these equations the interaction between electromagnetic fields and their environments can be determined. In the art of electrical engineering we progress by controlling this electromagnetic environment to elicit desirable field conditions.

To describe the medium in which fields exist the constitutive relationships are

required.

$$\mathbf{D} = \bar{\epsilon}\mathbf{E} \quad (1.9)$$

$$\mathbf{B} = \bar{\mu}\mathbf{H} \quad (1.10)$$

$$\mathbf{J}_c = \bar{\sigma}\mathbf{E} \quad (1.11)$$

Equations 1.9-1.11 are the most general form of the constitutive relations. The constitutive relations describe the manner by which the field and flux density terms of the Maxwell Equations interact with their medium. For a simple, isotropic medium equations 1.12-1.14 hold.

$$\bar{\epsilon} = \epsilon \quad (1.12)$$

$$\bar{\mu} = \mu \quad (1.13)$$

$$\bar{\sigma} = \sigma \quad (1.14)$$

It should be noted that ϵ and μ are complex where $\epsilon = \epsilon' - j\epsilon''$ and $\mu = \mu' - j\mu''$.

Most physically realizable materials, and all of the ones I will be discussing in this thesis, possess principal axes which allows them to be described by a diagonal matrix (such as 1.15), a much simplified form which is preferable for most uses. This is achieved by diagonalization, or the rotation of coordinates to a new axis (x',y',z') where only diagonal entries are non-zero and all off-axis entries are zero (1.15).

$$\bar{\epsilon} = \begin{bmatrix} \epsilon_x & 0 & 0 \\ 0 & \epsilon_y & 0 \\ 0 & 0 & \epsilon_z \end{bmatrix} \quad (1.15)$$

When two of the three parameters are equal, the medium is described as uniaxial

($\epsilon_x = \epsilon_y \neq \epsilon_z$) and of course if all three parameters are equal the simple medium form holds (Eq. 1.12).

1.3 Method

The majority of electrical engineering is dedicated to determining the physical arrangement of materials to force the desired electromagnetic field response. That is, electrical engineering is highly interested in producing the \mathbf{E} and \mathbf{H} terms of the Maxwell equations by controlling the circuit geometries.

In contrast this research endeavor focuses on the development of materials themselves. That is, our interest is in producing materials with desirable ϵ and μ . In particular the majority focus for this thesis is on expanding the currently limited range of magnetic (or μ) materials.

Several classes of natural materials exhibit magnetic properties. The most common magnets are the ferromagnetic transition metals, iron, cobalt, nickel and some rare earth metals such as gadolinium. These metals are highly conductive and therefore useless as magneto-dielectrics. Ferrimagnetics are ceramics exhibiting permanent magnetization. Unlike the ferromagnetic metals, many ferrites exhibit useful magneto-dielectric properties at low frequencies. The prototypical ferrite is Fe_3O_4 , the mineral magnetite (Figure 1.1).

In a ferrimagnetic ceramic a permanent magnetic moment is established by alignment of the atomic magnetic moments of uncanceled electron spin. There is some cancelation in ferrimagnetics due to electron-spin anti-alignment, but it is incomplete and the resulting saturation magnetization (M_s) is lower than for ferromagnetics.

The ferrites which are the most promising prospects for ceramic ferrites for offering low-loss operation in the microwave region are the hexagonal ferrites and garnets. The descriptors 'hexagonal ferrites' and 'garnets' refer to the geometric crystal structure

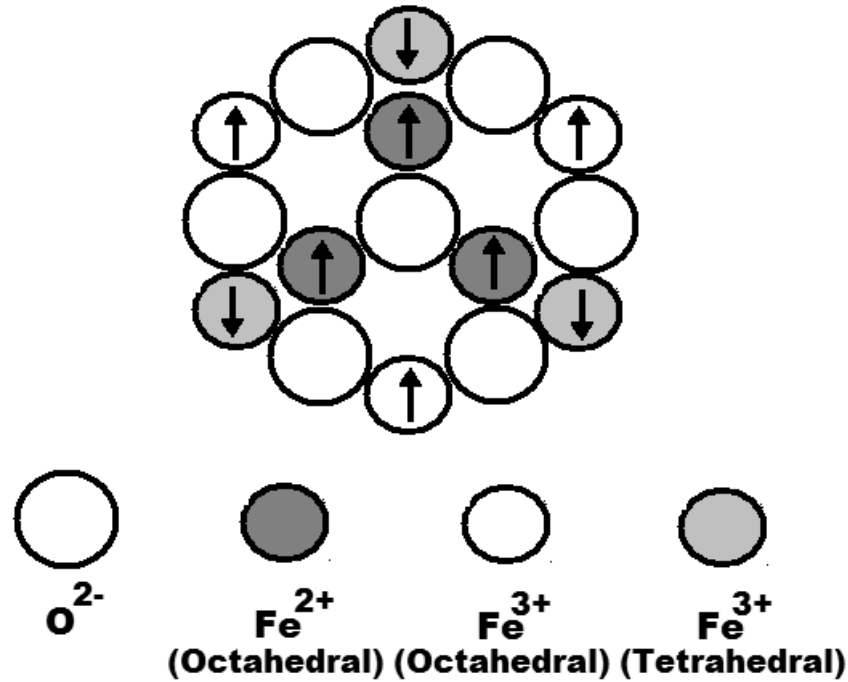


Figure 1.1: Incomplete magnetic spin cancellation in magnetite (Fe_3O_4) resulting in a net magnetism .

that the ceramic forms, and for our purposes the most important classes are Yttrium iron garnets ($Y_3Fe_5O_{12}$) and several groups of hexagonal ferrites exhibiting Z-axis symmetry, which will be referred to as 'Z-type' hexaferrites.

Unfortunately, low loss magnetic materials do not currently exist for use at microwave frequencies. The reason for this due to the gyromagnetic resonances exhibited by the mechanical atomic system. At excitation frequencies far below magnetic resonance the magnetic materials align their internal magnetic fields to track the applied field. The resulting magnetic permeability (μ_r) is observed to be relatively constant with changing frequency in this low frequency region. As the excitation frequency is increased and the resonant frequency is approached, the atomic system tracks the excitation field less effectively. At frequencies well above the resonance frequency, the atomic system is completely unable to track the excitation field and the magnetic orientations become random. This failure to track an excitation field makes the material effectively non-magnetic high above resonance and μ_r approaches 1.

In the frequency region around resonance, the atomic system attempts to track the excitation field but the mechanically induced phase lag results in a dramatic amplification of the magnetic susceptibility. Unfortunately, this magnetic enhancement is invariably coupled with a dramatic increase in magnetic loss as well, and the material becomes unusable for low-loss applications at frequencies significantly below where this amplification sets in. Figure ?? shows the typical frequency response of permeability and magnetic loss tangent for a modern high-frequency hexaferrite. Unfortunately, low loss magnetic materials do not currently exist for use at microwave frequencies.

1.4 Applications of Magneto-Dielectrics

Patch Antennas

Potential benefits of magnetic materials are dramatic. Consider the case of a patch antenna, conventionally fabricated with dielectric substrates to achieve miniaturization (1.2). Due to wave impedance mismatches at the substrate/freespace boundary energy is trapped in the substrate, unable to radiate. Such a condition leads to low impedance bandwidth ($BW=0.64\%$) and low radiation efficiency ($\eta=77\%$)

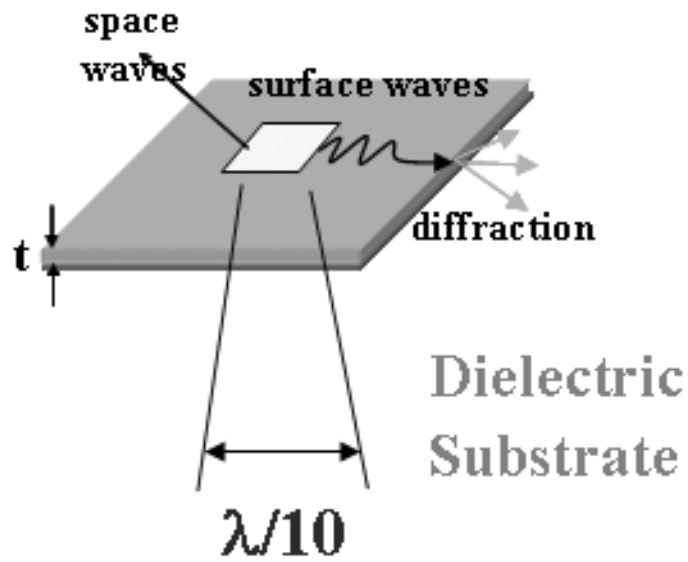


Figure 1.2: Probe Fed Microstrip Patch Antenna on a High Permittivity Substrate $\epsilon_r = 25.0 \tan\delta_e=0.001$.

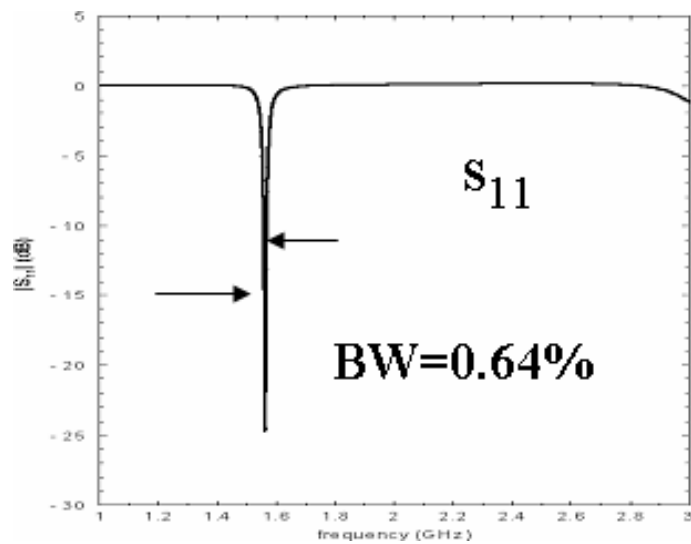


Figure 1.3: The Impedance bandwidth of probe Fed Microstrip Patch Antenna on a High Permittivity Substrate $\epsilon_r = 25.0$ is 0.64% and exhibits a low ($\eta=77\%$) efficiency.

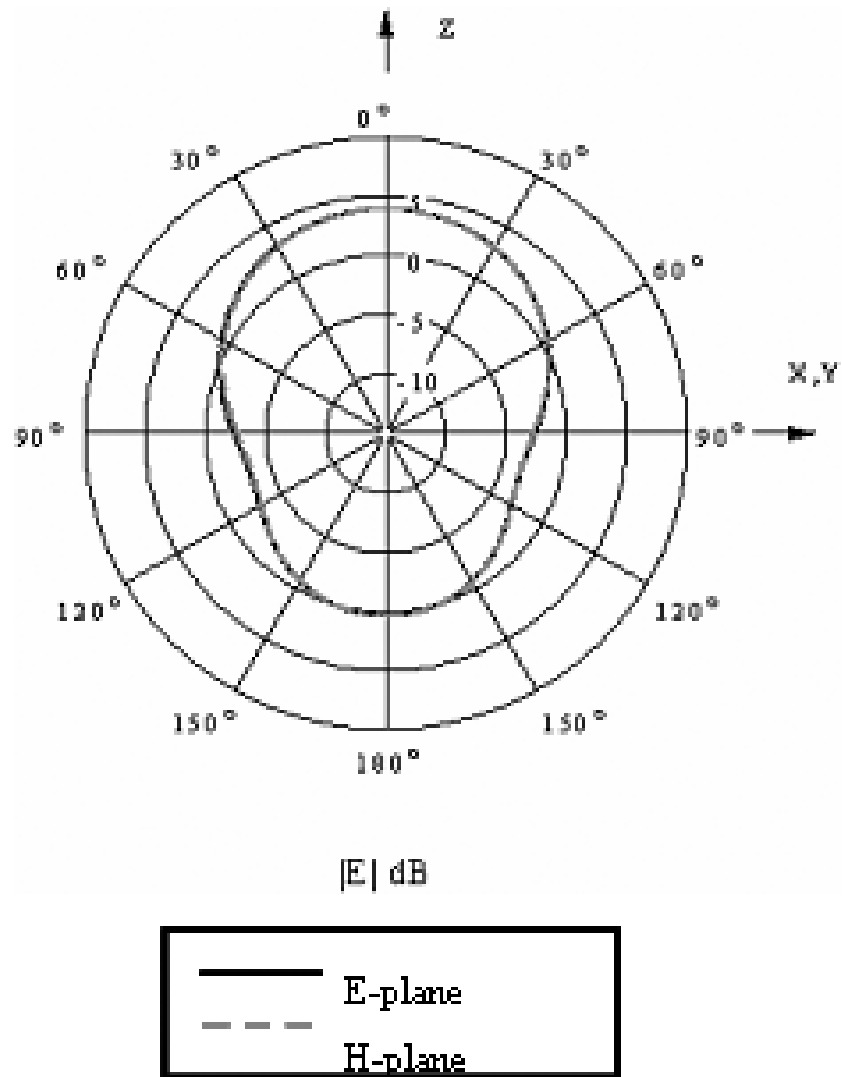


Figure 1.4: Radiation Pattern of antenna in Figure 1.2. Notice that the pattern is highly symmetric in E and H planes.

Equation 1.16 gives the transmission coefficient for electromagnetic plane-waves at normal incidence to a material interface. Although the circumstance of energy trapped in a dielectric substrate of a patch antenna is not this simple due to near-field and orientation issues, this relationship simply exhibits the basic condition that if the impedances are equal on both sides of the interface, maximum transmission occurs whereas if the wave impedances are vastly different very little energy will escape.

$$T = \frac{2\eta_2}{\eta_1 + \eta_2} \quad (1.16)$$

$$Z_w = \eta = \sqrt{\frac{\mu}{\epsilon}} \quad (1.17)$$

To understand the effect of material choice on the amount of energy that is trapped, the wave impedance must be determined.

For plane-waves exiting a material into free space, $\eta_2 = \eta_0$ in equation 1.17 because in free space $\mu = \mu_0$ and $\epsilon = \epsilon_0$. For a simple dielectric material such as the classic substrate of the patch antenna,

$$\epsilon = \epsilon_r \epsilon_0 \quad (1.18)$$

$$\mu = \mu_r \mu_0 \quad (1.19)$$

and the wave impedance mismatch in the substrate and in free space is determined by the ratio between the relative permeabilities and permittivities of the substrate material (1.17). Common current technologies employ purely dielectric materials where $\mu_r = 1$, and the impedance mismatch ratio is equal to the square root of the dielectric relative permittivity.

The trapping of high levels of energy in the near field dramatically reduces the antenna Quality Factor 'Q' and bandwidth. The reduced bandwidth indicates a fast-changing slope of the antenna input reactance, and this significantly increases the difficulty in matching the input impedance with a feed network.

In a practical example a miniaturization factor of five might be desired for a given antenna application. To achieve this miniaturization, the propagation of electromagnetic energy in the material must be slowed by a factor of five. To state it another way, the wave propagation constant κ in the material must be increased by a factor of five relative to free-space.

$$\kappa = \omega\sqrt{\mu\epsilon} \quad (1.20)$$

As equation 1.20 indicates, if the material is non-magnetic ($\mu_r = 1$) then a relative permittivity of twenty-five ($\epsilon_r = 25$) would be needed to achieve this miniaturization, but such a substrate would also exhibit a dramatic wave-impedance mismatch to free-space of 5:1.

By maintaining a constant $\mu_r\epsilon_r$ product, the propagation constant and miniaturization goals can be met. By separately controlling the $\frac{\mu_r}{\epsilon_r}$ ratio the wave impedance mismatch can be minimized. For example, if $\mu_r = \epsilon_r = 5$ the miniaturization factor goal of 5 would be achieved (1.20) but the impedance mismatch to free-space would disappear. (see equations 1.16-1.19)

Under many circumstances, significant performance improvements can be achieved by magneto-dielectric materials over more classical dielectrics.

For an aggressively miniaturized $\lambda/10$ patch antenna with a probe feed on a low-loss substrate ($\tan\delta_e = 0.001$) a non-magnetic $\epsilon_r=25$ material can provide the required x5 miniaturization factor (Fig. 1.2). Simulation predicts a $-10dB$ insertion-loss bandwidth of 0.64% (Fig. 1.3) and 77% efficiency with a well-matched probe feed. In contrast, with a magneto-dielectric of the same geometry where $\mu_r=\epsilon_r=5$ and

$\tan\delta_m=\tan\delta_e=0.001$ the same miniaturization factor (x5) is achieved (Fig. 1.5). Due primarily to the matched wave impedance to free space, simulation of this magneto-dielectric predicts a $-10dB$ insertion-loss bandwidth of 7.94% (Fig. 1.6) and 99% efficiency with a well-matched probe feed. In this case, bandwidth was increased by a factor of greater than ten and inefficiency was reduced by a factor better than 20.

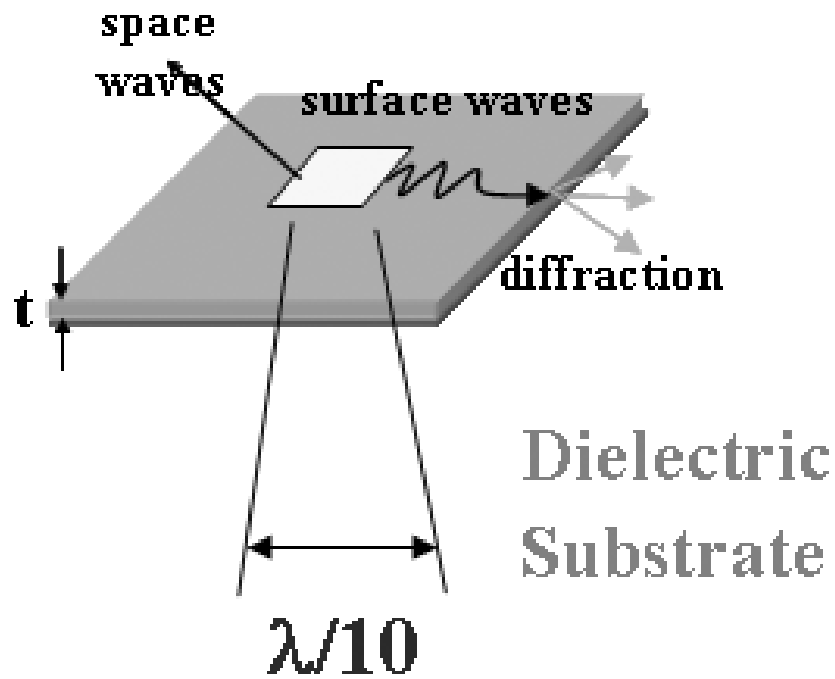


Figure 1.5: Probe Fed Microstrip Patch Antenna on an Impedance Matched Magneto-Dielectric Substrate $\epsilon_r = \mu_r = 5.0 \tan\delta_e = \tan\delta_m=0.001$.

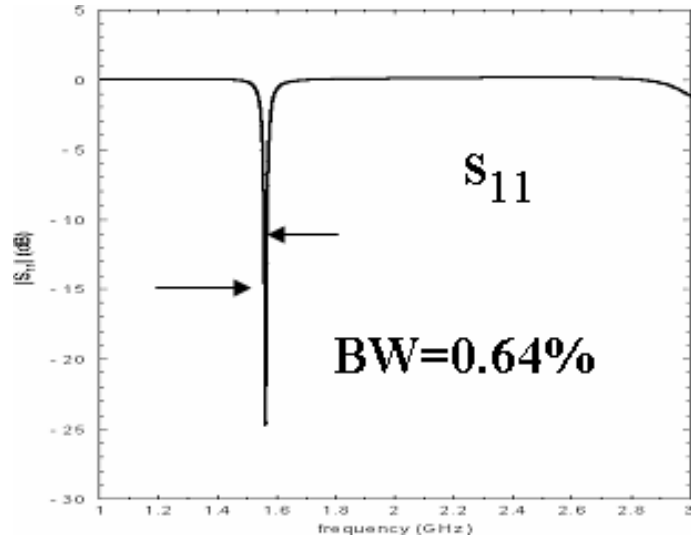


Figure 1.6: The Impedance bandwidth of probe Fed Microstrip Patch Antenna on an Impedance Matched Magneto-Dielectric Substrate $\epsilon_r = \mu_r = 5.0$ is 7.94% and exhibits a high ($\eta=99\%$) efficiency.

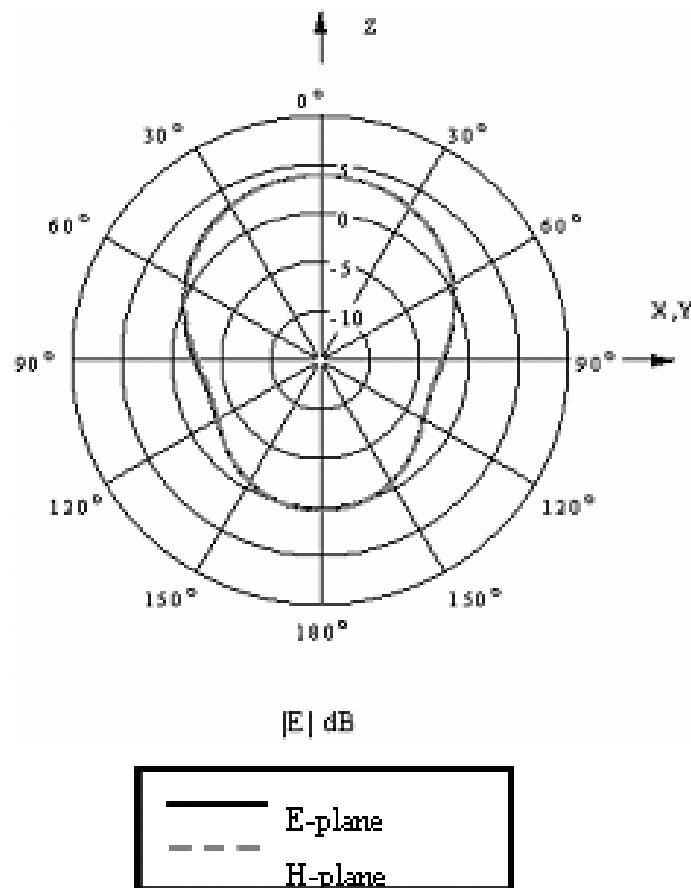


Figure 1.7: Radiation Pattern of antenna in Figure 1.5.

Dielectric Resonator Antennas

Promising results are implied by simulation for other applications as well. For a dielectric resonator antenna simulation, bandwidth was increased from 2.75% to 12.08%, an improvement factor of better than 4.5 simultaneous with improved efficiency when magneto-dielectrics were employed.

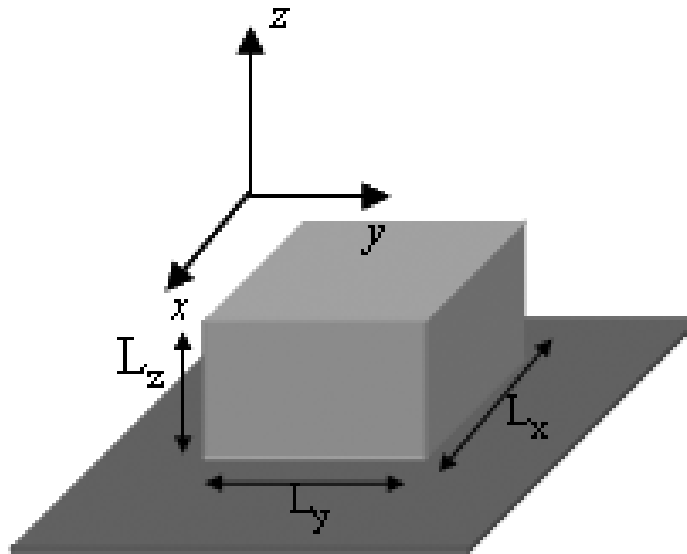


Figure 1.8: High Permittivity Dielectric Resonator Antenna
($L_x=L_y=0.15\lambda_0=26.67\text{mm}$, $L_z=0.091\lambda_0=6.67\text{mm}$) $\epsilon_r = 25.0$, $\mu_r = 1.0$
 $\tan\delta_e=0.001,\tan\delta_m=0$.

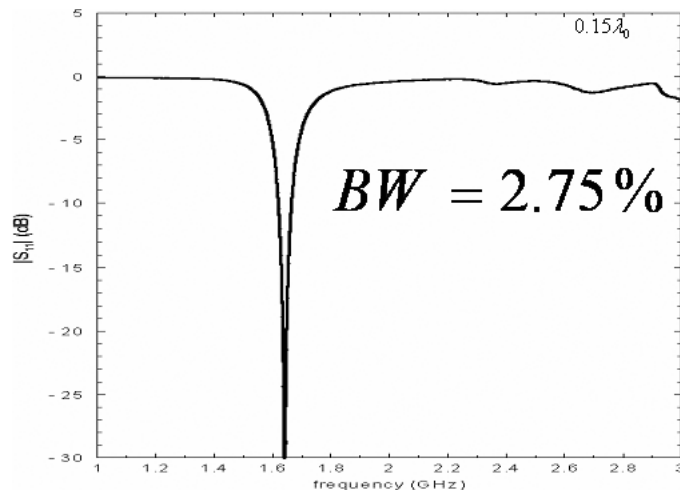


Figure 1.9: The Impedance bandwidth of probe Fed High Permittivity DRA $\epsilon_r = 25.0$ is 2.75% and exhibits a low ($\eta=77\%$) efficiency.

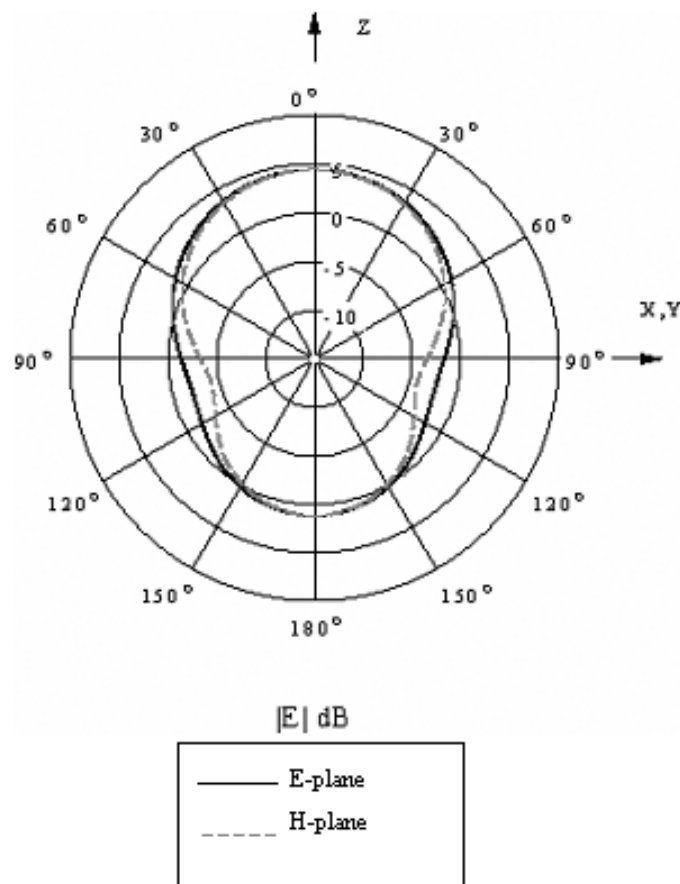


Figure 1.10: Radiation Pattern of DRA in Figure 1.8.

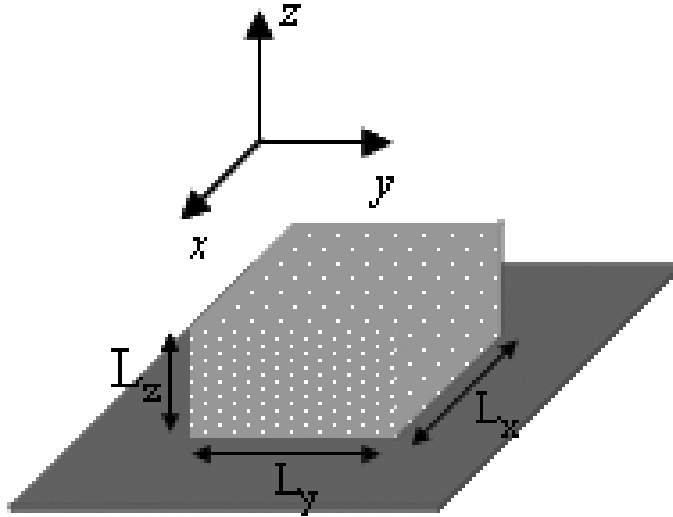


Figure 1.11: Magneto-Dielectric Resonator Antenna ($L_x=L_y=0.15\lambda_0=26.67\text{mm}$, $L_z=0.091\lambda_0=6.67\text{mm}$) $\epsilon_r = 5.0$, $\mu_r = 5.0$ $\tan\delta_e=\tan\delta_m=0.001$

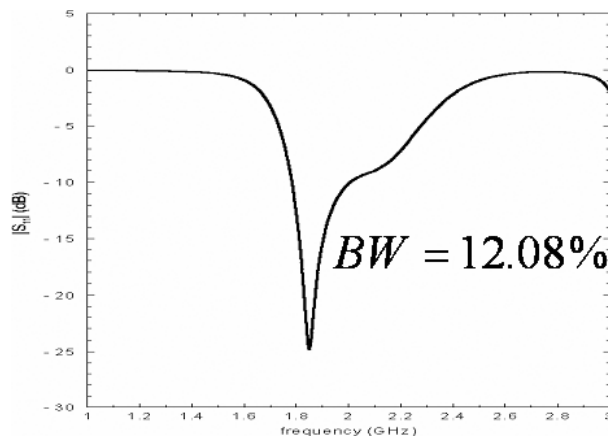


Figure 1.12: The Impedance bandwidth of probe Magneto-Dielectric Resonator Antenna ($\epsilon_r = 5.0, \mu_r = 5.0$) is 12.08%

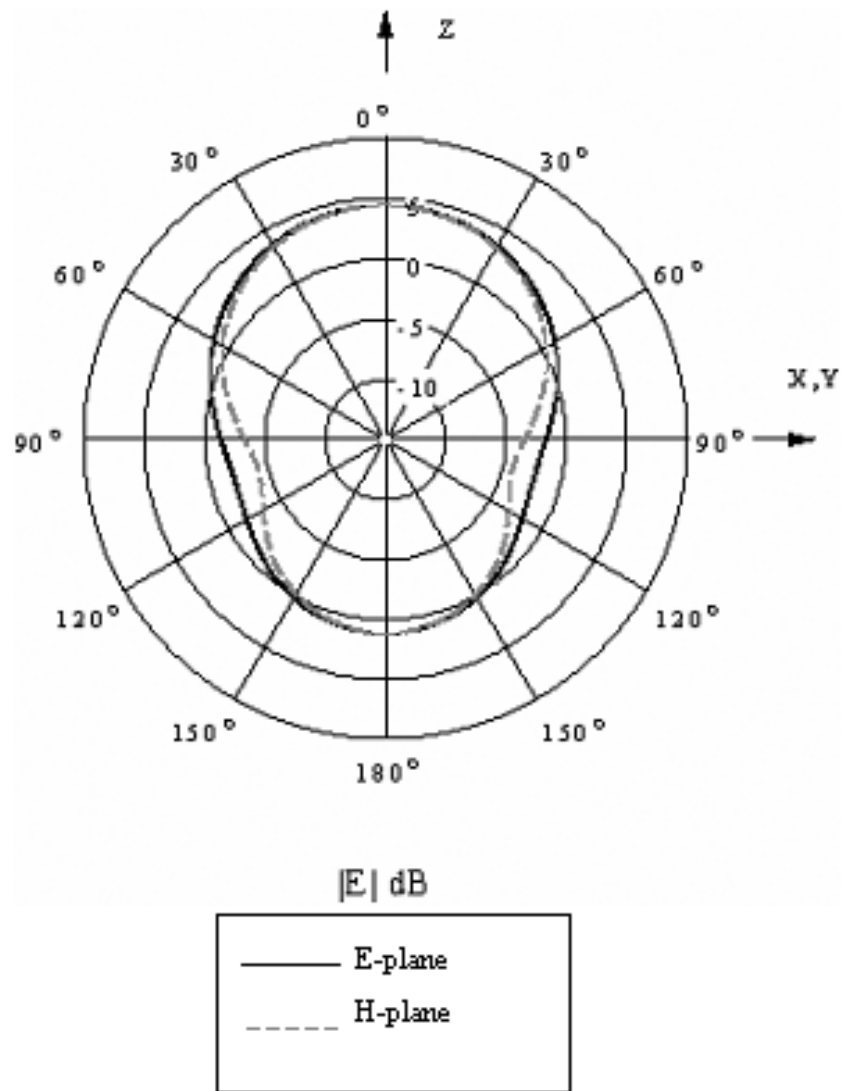


Figure 1.13: Radiation Pattern of MDRA in Figure 1.11.

Electromagnetic Insulators

Electromagnetic band-gap materials can benefit from magneto-dielectrics as well. By incorporating $\mu_r = 16$ material into a $\epsilon_r = 16$ design, simulated band-stop performance was improved from -20dB to -44dB.

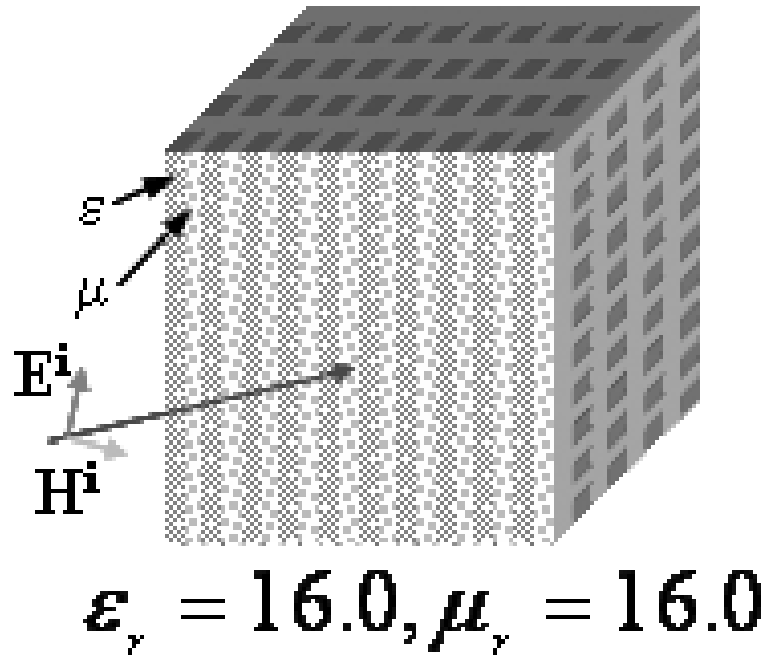


Figure 1.14: A 'woodpile' structure of permeable ($\epsilon_r=1, \mu_r=16$) and dielectric ($\epsilon_r=16, \mu_r=1$) materials stacked in alternation to achieve an electromagnetic band-gap phenomenon.

As these examples clearly show, there is opportunity for a dramatic improvement in a broad range of existing microwave technologies if practical low-loss magneto-dielectrics can be developed.

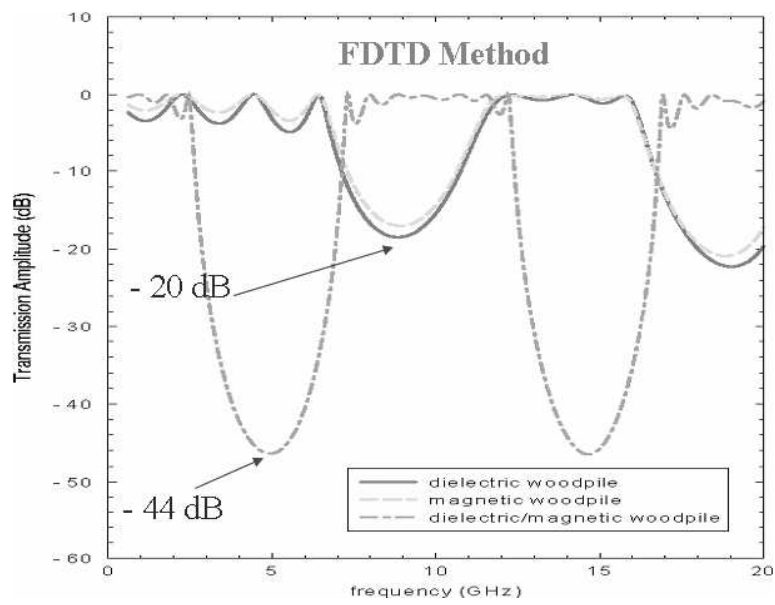


Figure 1.15: Transmission through a dielectric-air woodpile, a permeable-air woodpile, and a dielectric-permeable woodpile.

1.4.1 Elements of Research; Material Development, Characterization, and Application

Material Development

Our goal is to develop materials which possess appreciable magnetic properties in the microwave region. The desirable material properties should be defined quantitatively in order to determine the effectiveness of the effort. A relative permeability $\mu_r \geq 1.5$ would be a useful magneto-dielectric or if $\mu_r < 0$, a useful electromagnetic band-gap material. A low-loss magnetic material is one whose magnetic and electric loss tangents are each 2.0×10^{-2} or lower. The frequency range of our interest begins at approximately 100 MHz and extends to approximately 40 GHz, but since useful materials exist at the lower end of this region and miniaturization is often undesirable in the high GHz region, our goal will be to develop useful low-loss magnetic materials for application in the 200 MHz to 10 GHz range.

In this thesis, permeability enhanced ($\mu_r \geq 1.5$) and negative permeability materials were both developed.

Characterization

When a candidate material is proposed it must be characterized to identify its constitutive properties $\epsilon = \epsilon' - j\epsilon''$, $\mu = \mu' - j\mu''$, and σ . With moderately low-loss dielectric materials in the microwave region σ is treated to be zero, and any conductor losses are incorporated in the ϵ'' term.

With these material properties known, the candidate can be considered as a design option in applications with confidence in what the resulting electromagnetic response will be.

In this thesis, new tools and methods of characterization which are suitable to measuring the new materials are developed.

Application

Once a new material is developed and has been characterized it must be proven useful to merit consideration. The principle application chosen for newly developed materials in this endeavor is antennas. Planar antennas and superdirective antenna arrays are designed and fabricated to prove the properties of the new materials in actual applications.

1.5 Chapter Outline

1.5.1 Chapter 1: Introduction

In chapter one I have introduced the motivation and goals of this research. Materials exhibiting useful magnetic properties such as permeability enhancement, impedance matching, and EBG operation will be developed. In order to measure the electromagnetic properties of these materials, new techniques and tools for magnetic material characterization will be developed. Lastly, these materials will be applied to solving common problems in the design of practical antennas and antenna arrays.

1.5.2 Chapter 2: Natural Magnetic Materials

A basic introduction to the source and nature of magnetism in natural materials will be presented. The limitations of modern magnetic materials will be discussed and chief among these is that in the microwave region magnetic materials exhibit either too high a loss tangent, or no magnetism at all ($\mu_r = 1$). This condition is due to the gyromagnetic resonances in these materials occurring at frequencies which are not far enough above the desired operating frequency. The benefits of impedance matched embedded antennas are discussed and progress towards their development is described.

Hexaferrites (A Natural Composite)

By exposing a Z-type HexaFerrite composite to extremely high magnetic bias fields during processing, the orientation-dependent permeability was enhanced. Several different processing attempts produced materials with promising permeability levels along an XY orientation up to 400 MHz, the magnetic loss tangent of these materials is unacceptable for high efficiency designs, but may be acceptable for some applications.

To test this material, a patch antenna was fabricated and measured. As predicted the antenna efficiency was low, probably due to the high loss factor.

1.5.3 Chapter 3: Metamaterials

In chapter 3 Metamaterials, materials engineered to possess desirable electromagnetic properties, will be introduced and explained in some detail. Modern metamaterial research will be discussed and popular applications will be introduced.

Embedded Circuit Spiral Resonator

We have developed a new form of metamaterial, the embedded circuit spiral resonator which exhibits both enhanced permeability ($\mu_r \geq 1.5$) and electromagnetic band gap ($\mu_r < 0$) properties. Design equations and an equivalent circuit model are introduced. Methods of electromagnetically simulating such metamaterials will be exhibited and shown to validate the models we have developed. Later in this thesis, the Embedded Circuit Spiral resonator proves itself to be both a highly versatile and useful device for microwave applications.

1.5.4 Chapter 4: Material Characterization

Various material characterization methods and tools were developed for this chapter. Experimentation validates these material characterization techniques as being

effective.

Waveguide Toolkit

With four unknown parameters μ' , μ'' , and ϵ' , ϵ'' to be determined, four independent measurement values are required for full material characterization at a given frequency. Measuring the magnitude and phase of a reflected and transmitted wave through a material to be characterized is the most straightforward method. A software tool was developed which extracts complex permittivity and permeability values from the scattering parameters of a sample in a waveguide.

Frequency Extended Perturbation Method

Perturbation methods of material characterization in resonant structures are highly accurate, and therefore are popular for the precise material characterization. In this research, a theory predicting off-resonance behavior was developed and tested. Simulation and measurement indicate that the off-resonance behavior of sample perturbed systems can be predicted accurately if the sample characteristics are known.

The inverse problem of determining the sample characteristics by comparing the sample loaded and unloaded resonant structure behavior was also addressed. It was found that for low-loss materials, or for materials where the loss was approximately constant in the bandwidth surrounding the structural resonance, the materials characteristics can be determined within reasonable error.

Hybrid Perturbation Method

Resonance cavity perturbation methods provide highly accurate measurement of purely dielectric materials. Existing materials which exhibit magnetic properties invariably also exhibit dielectric properties. If a real sample of physical size is placed in a standard resonance cavity at the maximum of the magnetic field, the resonance shift

observed will be a combination of the contributions from the materials dielectric and magnetic properties and the magnetic properties can not be determined by existing methods.

A hybrid method combining 'classical' perturbation method techniques with numeric simulation 'curve-fitting' procedures was developed which overcomes many of the deficiencies of measuring magnetic materials by the perturbation method. The resonant behavior of the cavity and sample are simulated for various combinations of sample permittivity and permeability in both the electric-field maximum and magnetic-field maximum geometries. Matching the experimentally observed response to the simulations, the sample permittivity and permeability can be uniquely identified.

1.5.5 Chapter 5: A miniaturized Patch Antenna on Magnetic Metamaterial Substrate

Embedded circuit spiral resonators were assembled to realize one-dimensional permeability enhancement. For applications where only a single field orientation exists, such as is the case under a patch antenna the magnetic property from a uniform array of embedded resonators is ideal.

Magnetic substrates were fabricated from our embedded circuit designs on commercially available low-loss dielectrics. The magnetic properties of the substrate varied in the $mu_r = 1.5 - 4$ range in the useful frequency region below the resonant frequency of the embedded circuits.

A patch antenna was printed on the top of the magnetic substrate, and by varying the radiating frequency and orientation the theoretical model for the magnetic substrate was validated. This experimentation validates the embedded circuit spiral resonator metamaterials, although loss factors are higher than would be desirable. The frequency and orientation dependence of the substrate permeability, and its im-

pact on miniaturization and efficiency, was validated to match the trends predicted by the model.

1.5.6 Chapter 6: Patch Antenna over Reactive Impedance Surface

This experimental work validates the theoretical analysis of K. Sarabandi in showing that the interaction between a radiating element and a lossless reflecting backplane can be minimized by judicious choice of a reactive surface impedance. This work is particularly significant in that it proves that neither the classic PEC nor recently popular PMC is an optimal backplane for an antenna.

Induced currents on both PEC and PMC backplanes generate a maximum field magnitude at the position of the source. This causes strong source/image coupling and significantly decreases antenna efficiency and bandwidth. By engineering the choice of backplane reactance, source/image interaction was minimized and efficiency/bandwidth maximized.

A patch antenna with RIS was designed, fabricated, and measured. To our knowledge the resulting efficiency, gain, and bandwidth were the highest reported in the literature.

1.5.7 Chapter 7: Electromagnetic MetaMaterial Insulator

Based on the same embedded circuit spiral resonator metamaterial design discussed above, a highly effective metamaterial insulator was designed, extensively simulated, then fabricated and measured. In the spectral region immediately above spiral resonance, the relative permeability of the medium is negative. In this negative permeability region, the material can not support propagating modes. Consequently, in this frequency region the metamaterial resonator acts as an excellent insulator,

providing over 20 dB of insulation.

1.5.8 Chapter 8: Metamaterial Insulator enabled Superdirective Array

A superdirective antenna array is one which exhibits higher directivity than a uniformly excited array of the same size (geometrically and in number of elements). One of the most significant obstacles to the effective implementation of superdirective arrays is the problem of mutual coupling between adjacent array elements.

By employing metamaterial insulators, the coupling between densely packed array elements is reduced by approximately 20dB. With the inter-element coupling substantially suppressed, it is shown to be practically possible to achieve superdirectivity and other complex beam forming with a physically small array.

In this chapter we have designed, fabricated, and measured a superdirective array employing metamaterial insulators to suppress mutual coupling. The measurements validate that superdirectivity was achieved.

1.5.9 Chapter 9: Conclusion

In chapter 9 the most important elements of this thesis are summarized. The implications of various aspects of this research are presented and possible topic areas of future research are discussed.

CHAPTER 2

Natural Magnetic Materials

I am never content until I have constructed a mechanical model of what I am studying. If I succeed in making one, I understand; otherwise I do not. lord Kelvin

2.1 Chapter Introduction

In this chapter I present a brief general introduction to the phenomenon behind magnetism of materials in the microwave frequency regime. An explanation of the source of magnetic permeability is described, and the phenomenon of gyromagnetic resonance is introduced. It is explained that this phenomenon results in the utility of most natural magnets for microwave applications to be minimal.

A new composite material developed in conjunction with the Trans-Tech corporation is presented at the end of this chapter. This material has the highly desirable property of being impedance matched in the VHF/UHF region for two of its three principle axis.

2.2 Understanding Natural Magnets

Due to the absence of magnetic monopoles, magnetic fields are described by Amperes Law as being produced by the motion of charges, either individually or in current form. The bulk permeability of a material is a quantitative description of how readily the material experiences magnetization, which is when an externally applied magnetic field causes the charges in a material to align their motion such that their magnetic moments align parallel or anti-parallel to the external magnetic field.

A circulating charge produces a magnetic moment (\mathbf{m}) in each atom, and the magnetic moments of atoms are the building blocks of natural magnetics (Fig. 2.1). The macroscopic magnetic properties of materials are the consequence of the magnetic moments associated with individual electrons. The magnitude of electron magnetic moments are many orders of magnitude stronger than nuclear magnetic moments produced by the movement of protons in the atomic nucleus due to the much greater nuclear masses. Each electron in an atom has magnetic moments that originate from two sources. One is related to its orbital motion around the nucleus; being a moving charge every electron may be considered to be a small current generating a very small magnetic field and having a magnetic moment along its axis of revolution. The second magnetic moment originates from the electron spin about its own axis. This spin magnetic moment is directed along the spin axis. Spin magnetic moments may only be in either an "up" direction or in an antiparallel "down" direction. By these means each electron in an atom may be thought of as being a small magnet having permanent orbital and spin magnetic moments.

The Magnetization Vector \mathbf{M} (Magnetic Polarization Vector) of a material is the average of the individual induced magnetic dipole moments of the atoms due to an externally applied magnetic field (\mathbf{H}_a).

How easily the material magnetizes, aligning its magnetic dipole moments to the externally applied magnetic field is quantified as its magnetic susceptibility (χ_m)

(dimensionless unit).

$$\mu_r = \mu_0(1 + \chi_m) \text{ (henries/meter)} \quad (2.1)$$

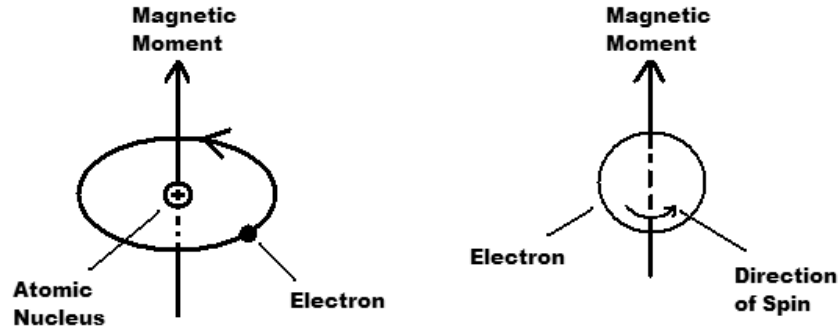


Figure 2.1: The permeability of natural materials is caused by either the orbital or electron spin magnetic moment. Of the two, the electronic spin magnetic moment is much stronger and when present and uncanceled is the source of observable magnetic properties.

In each individual atom, the orbital magnetic moments of electron pairs cancel each other; this cancellation also occurs for the paired spin moments. For example, the spin moment of an electron with spin "Up" will cancel that of one with spin "Down". The net magnetic moment, then, for an atom is just the sum of the magnetic moments of each of the constituent electrons, including both orbital and spin contributions. For an atom with completely filled electron shells or sub-shells, when all electrons are considered, there is total cancellation of both spin and orbital moments [2].

Diamagnetism and Paramagnetism

The types of magnetism naturally occurring include diamagnetism, paramagnetism, and ferromagnetism. In addition, antiferromagnetism and ferrimagnetism are considered to be subclasses of ferromagnetism. Diamagnetism is a very weak form of magnetism induced by the alignment of orbital magnetic moments in a direction opposite that of an applied field resulting in a very small negative susceptibility.

Diamagnetism persists only while an external field is applied. Paramagnetism occurs when atomic magnetic dipoles created by incomplete cancelation of electron spin are free to rotate and preferentially align with an external field. In Paramagnetism there is no interaction between adjacent dipoles, and the net susceptibility is very small but positive.

Table 2.1: Diamagnetic Materials

Material	Relative Permeability (μ_r)
Silver	0.99998
Lead	0.999983
Copper	0.999991

Table 2.2: Paramagnetic Materials

Material	Relative Permeability (μ_r)
Aluminum	1.00002
Nickel chloride	1.00004
Palladium	1.0008

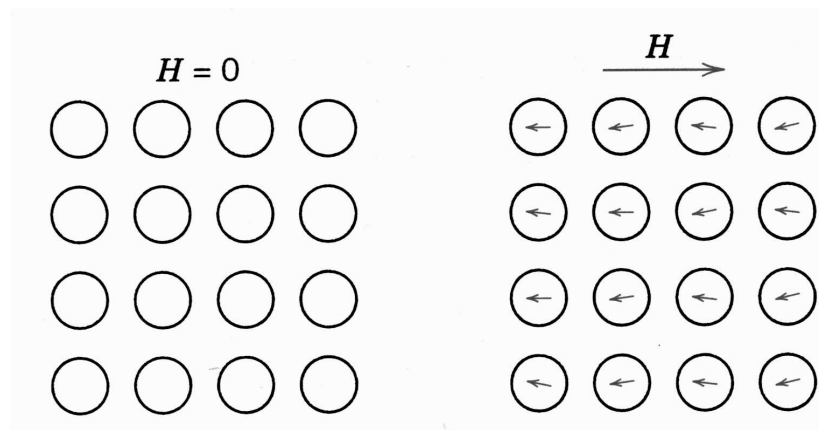


Figure 2.2: The Spin Magnetic Moment of Diamagnetic materials with no applied field and in the presence of an externally applied magnetic field.

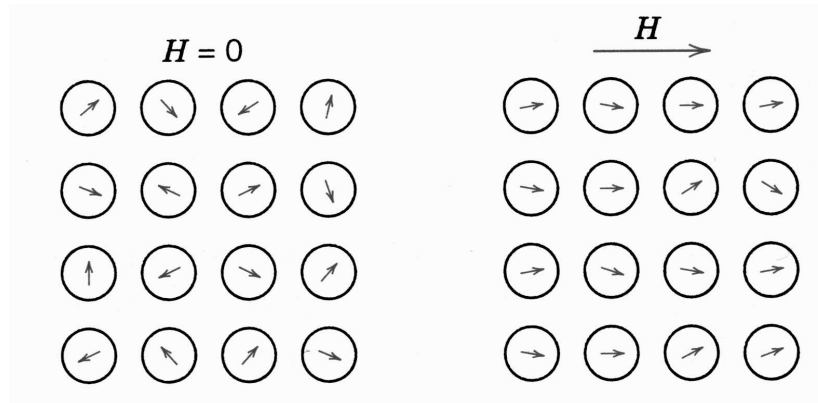


Figure 2.3: The Spin Magnetic Moment of Paramagnetic materials in with no applied field and in the presence of an externally applied magnetic field.

Ferromagnetism

Ferromagnetism is exhibited in some metallic materials such as iron, cobalt, or nickel when magnetic moments due to uncanceled electron spins of adjacent atoms interact to align with one another and produce magnetic susceptibilities as high as 10^6 . This strong magnetization is of limited use for magneto-dielectrics due the the high conductivity and ohmic loss of the metals. Anti-ferromagnetism occurs when the coupling interaction between adjacent atoms result in anti-parallel alignment. These magnetic moments cancel one another, and there is no net magnetic moment.

Table 2.3: Ferromagnetic Materials

Material	Relative Permeability (μ_r)	conductivity (σ)
Cobalt	250	1.72×10^7
Nickel	600	1.45×10^7
Iron	5,000	1.03×10^7

/clearpage

Table 2.4: AntiFerromagnetic Materials

Material	Relative Permeability (μ_r)
Manganese Oxide (MnO)	1.08
Terbium	1.095
Iron Oxide (FeO)	1.065

Ferrimagnetism

Finally, and most promisingly is Ferrimagnetism- a magnetism exhibited by some ceramics as a result of their complex crystal structure. In such ceramics there are parallel and antiparallel coupling interactions between the ions, similar to in anti-ferromagnetism, however the net ferrimagnetic moment arises from the incomplete cancelation of spin magnetic moments [2]. Most ferrimagnetics exhibit permeabilities and conductivities which are highly dependent on temperature and processing. Therefore, their properties are not suitable for tabulation- but there is promise that proper processing may enable desirable properties to be elicited from these materials.

In the presence of a magnetic field, the magnetic moments of a Ferrimagnetic material tend to become aligned with the applied field and to reinforce it by virtue of their own magnetic fields. Figures 2.6 and 2.7 show the complex magnetic permeabilities ($\mu = \mu' - j\mu''$) of yttrium and calcium-vanadium garnet ferrimagnetic ceramics as a function of frequency.

Gyromagnetic Resonance

The challenge to microwave applications arises from the inertia of atomic systems. Although the mass of an electron is small, it is not zero and the attempts of the electron magnetic dipole moments to track an externally applied magnetic field deteriorate and eventually fail altogether for inertial reasons as the excitation field approaches and passes the materials gyromagnetic resonance frequency. As frequency increases and gyromagnetic resonance is approached, the materials loss-factor

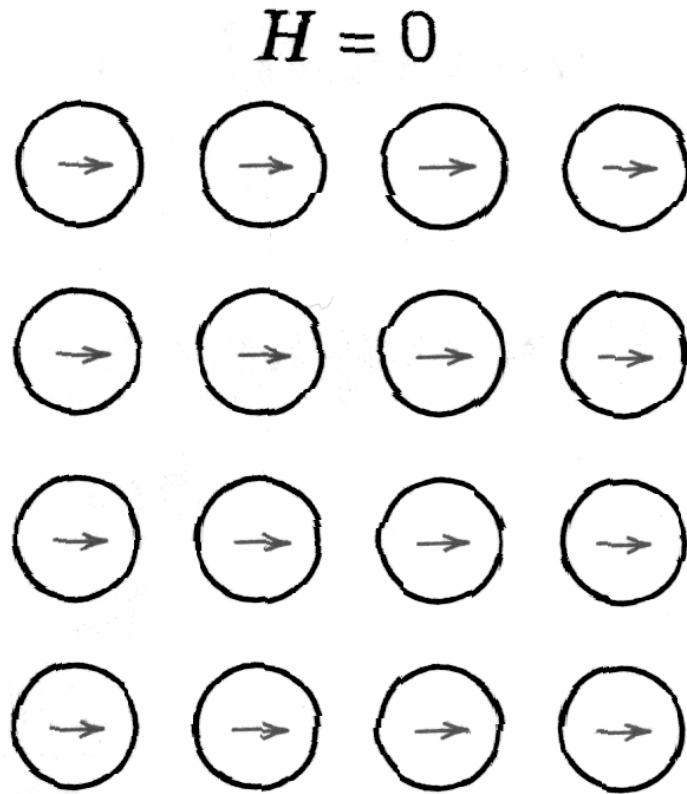


Figure 2.4: The Spin Magnetic Moment of Ferromagnetic materials in the absence of an applied magnetic field.

increases dramatically as exhibited in figure 2.7 and above resonance the material becomes essentially non-magnetic ($\mu_r=1$). Unfortunately for microwave engineers, it appears that magneto-dielectrics produced from natural materials exhibit gyro-magnetic resonance in the VHF-UHF region and are unusable for low-loss microwave applications.

If a mechanism similar to natural magnetics can be developed for microwave operation by synthetic means, low-loss operation may be pushed into the microwave region and low-loss microwave magneto-dielectrics may become a reality. Already, various researchers have proven that it is possible to replicate magnetic behavior by inserting electromagnetically small metallic inclusions into a natural dielectric. [[1], [3], [4], [5], and [6]]

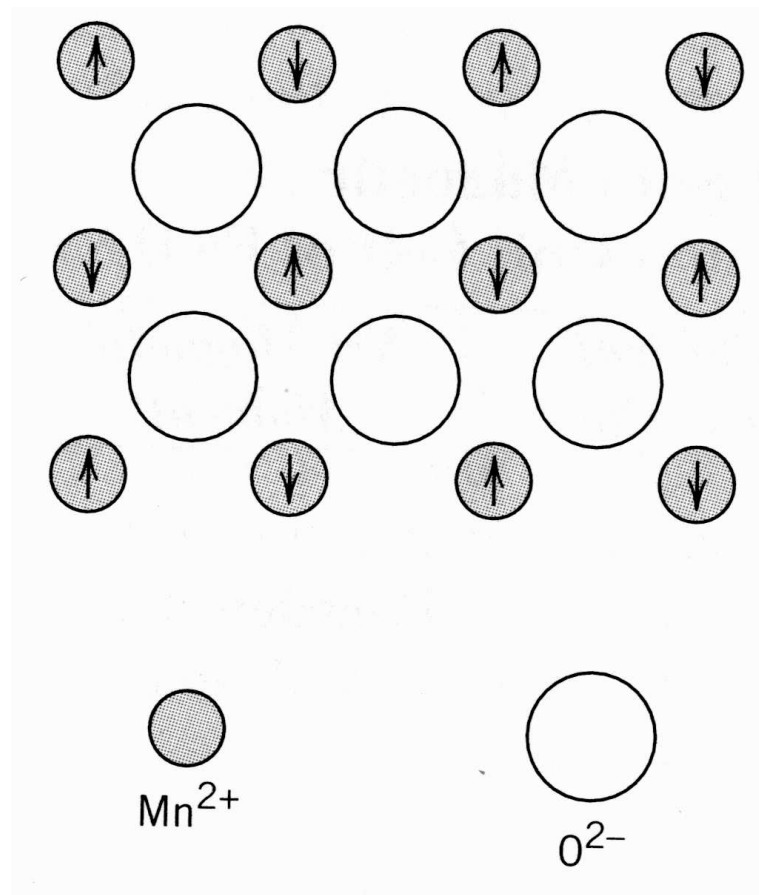


Figure 2.5: The Spin Magnetic Moment of AntiFerromagnetic materials in the absence of an applied magnetic field.

2.3 New Advances in Natural Magnets

With a goal of pushing the useful range of magnetically permeable materials to as high a frequency as possible, we engaged in joint development with engineers of the Trans-Tech Corporation. This endeavor resulted in a moderately low loss 2-Dimensional impedance matched ceramic for operation in the VHF/low UHF region.

2.3.1 Application of Impedance Matched Materials

When $\epsilon_r = \mu_r$, the material is described as impedance matched and if it is low-loss it is an excellent candidate for embedded antenna miniaturization.

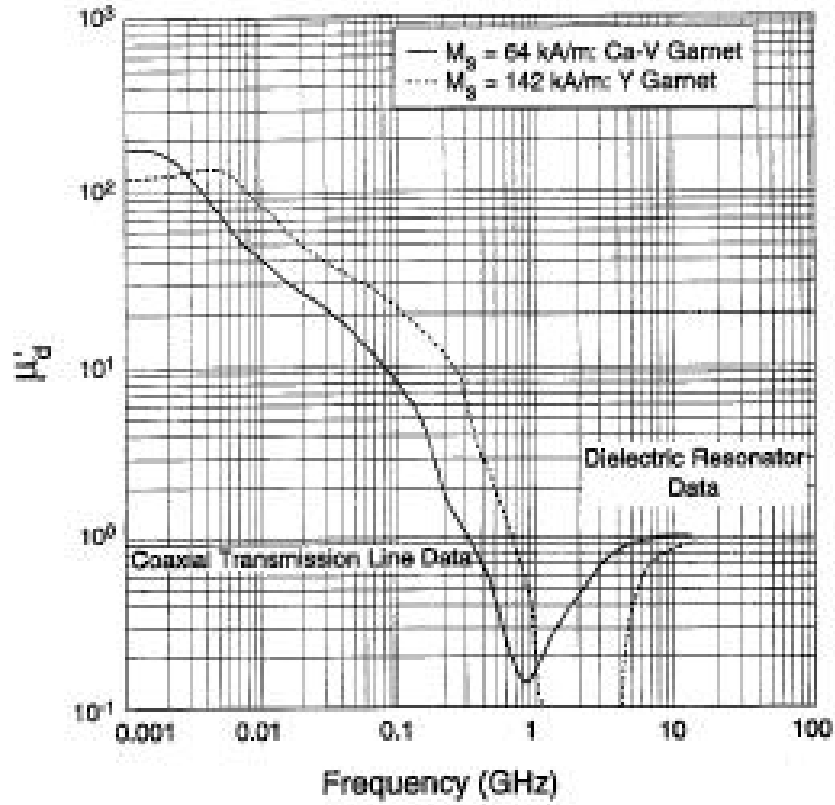


Figure 2.6: Magnetic permeability of yttrium and calcium-vanadium garnets in the region below and around resonance.

To test this concept, a high performance antenna was identified. The four-point antenna provides wide bandwidth, high gain, and a variety of polarizations [7]. The four-point antenna operates as a crossed bow-tie (Figure 2.10) and can be used a quarter wavelength above a PEC ground plane (Figure 2.11). When operating in free space, such an antenna can provide either linear or circular polarization, achieves 8-9dBi over its impedance bandwidth of 100%, and generates low Cross-Polarization ($< -30dB$).

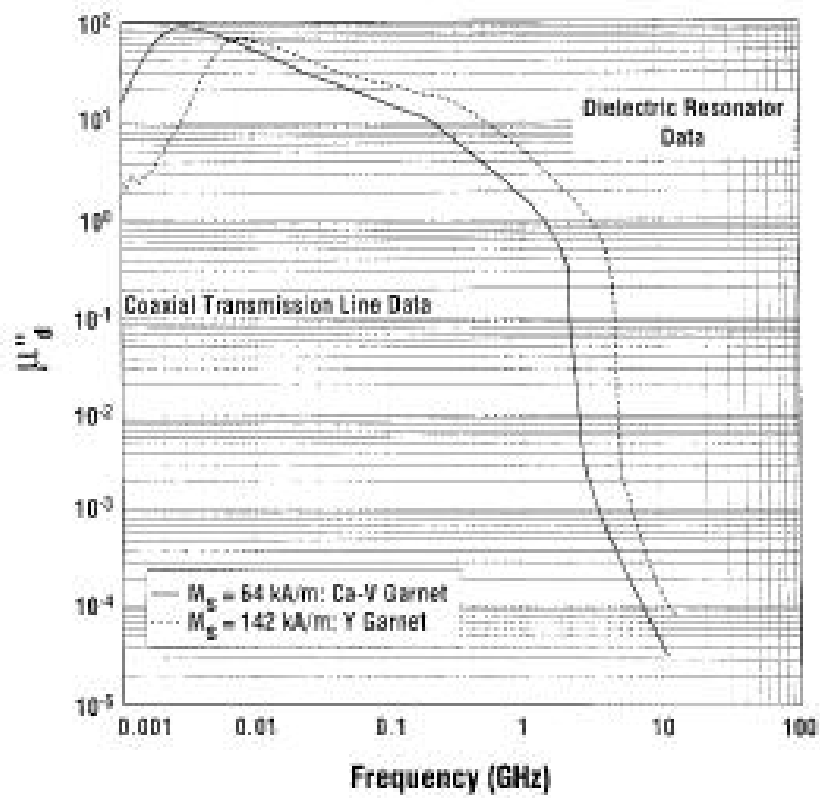


Figure 2.7: Magnetic loss levels of yttrium and calcium-vanadium garnets in the region below and around resonance.

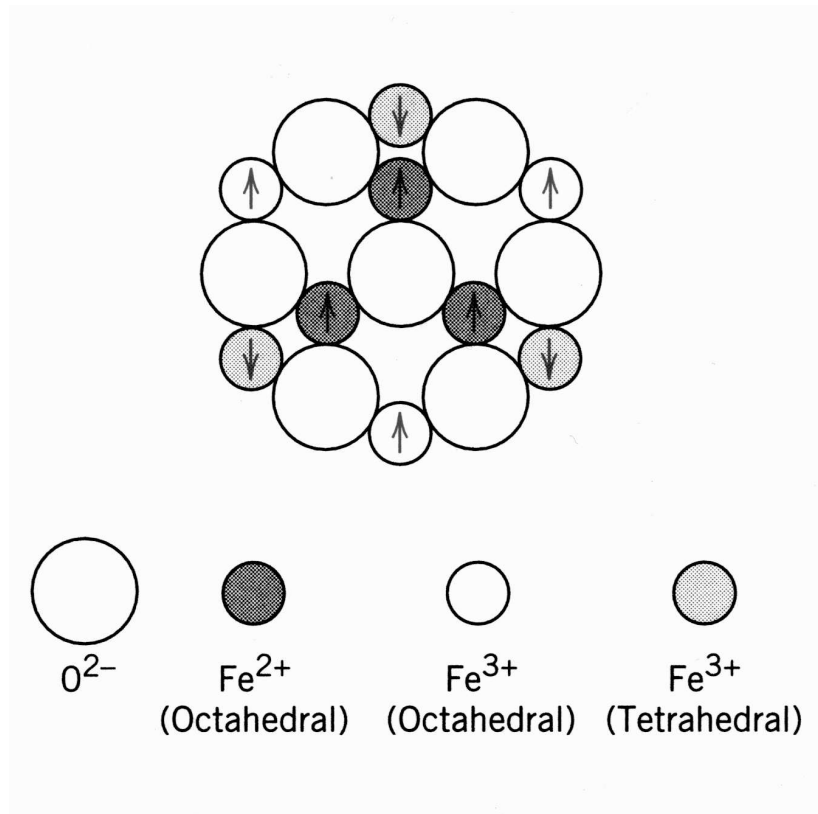


Figure 2.8: Simplified 2D structure of Magnetite.

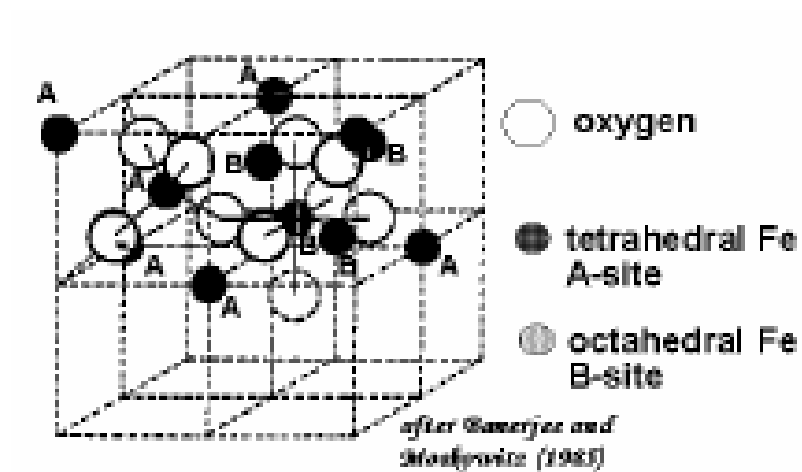


Figure 2.9: Magnetite structure in 3D.

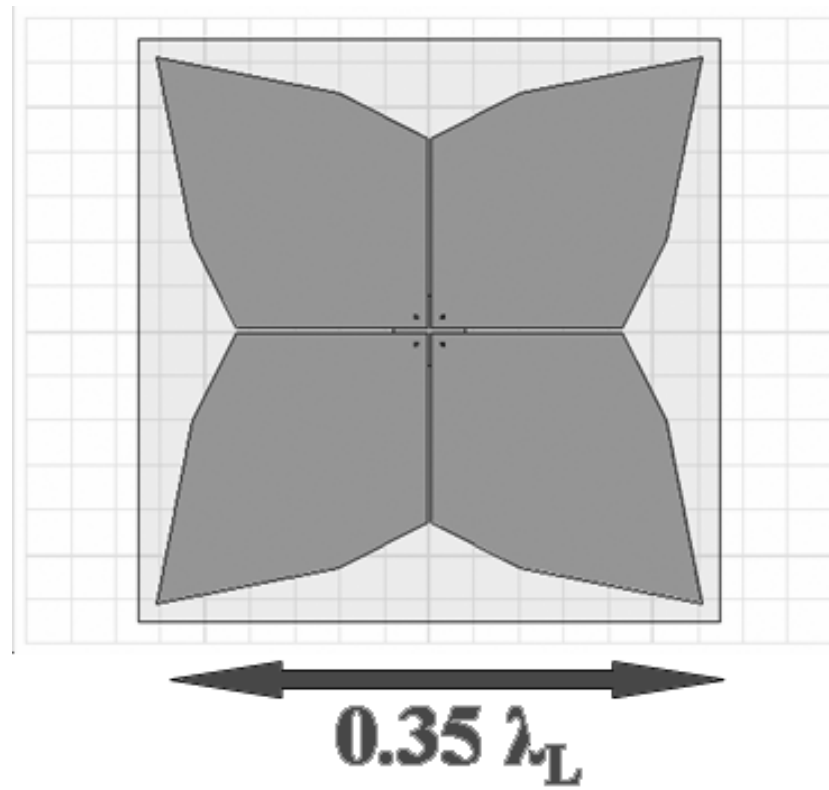


Figure 2.10: The four point antenna is a crossed bow-tie antenna developed by the Virginia Tech Antenna Group.

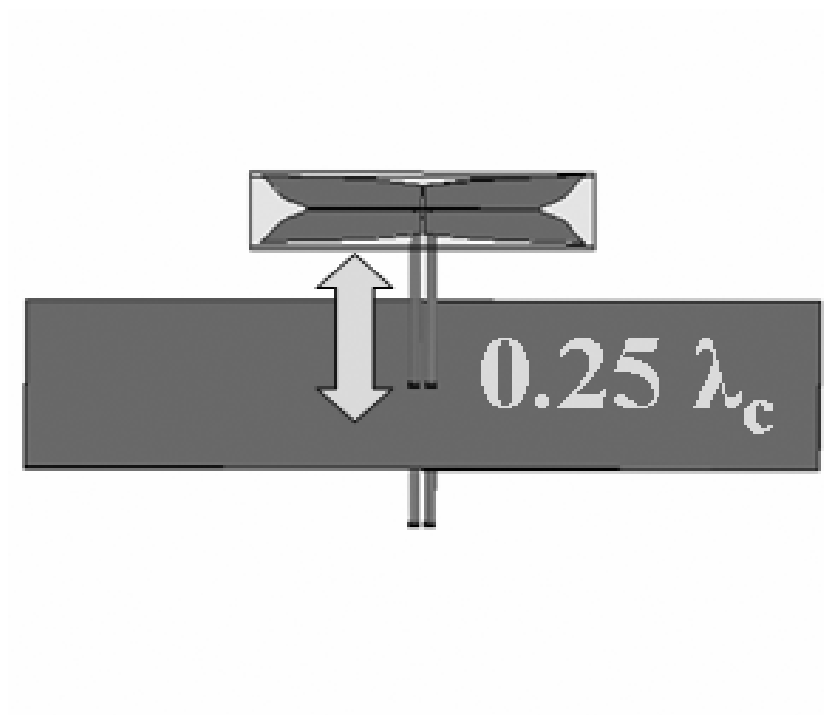


Figure 2.11: The four point antenna one quarter wavelength above a PEC ground plane.

If the four-point antenna is embedded in an isotropic, low loss, non-dispersive, impedance matched material (Figure 2.12) performance similar to the free-space performance will be achieved. Figure 2.13 shows that as the permittivity and permeability of an impedance matched material is increased to moderate values, the impedance bandwidth is unaffected and figure 2.14 shows that the radiation pattern integrity remains intact. As such, embedding an antenna in an impedance matched medium can achieve miniaturization without significant degradation in performance (Table 2.5).

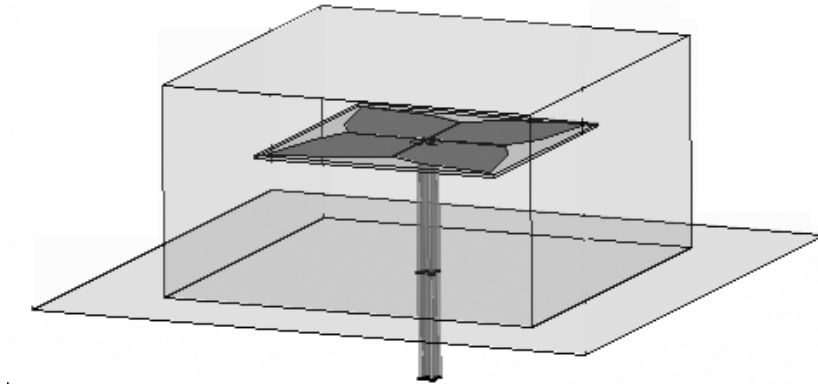


Figure 2.12: The four point antenna embedded in an impedance matched material block.

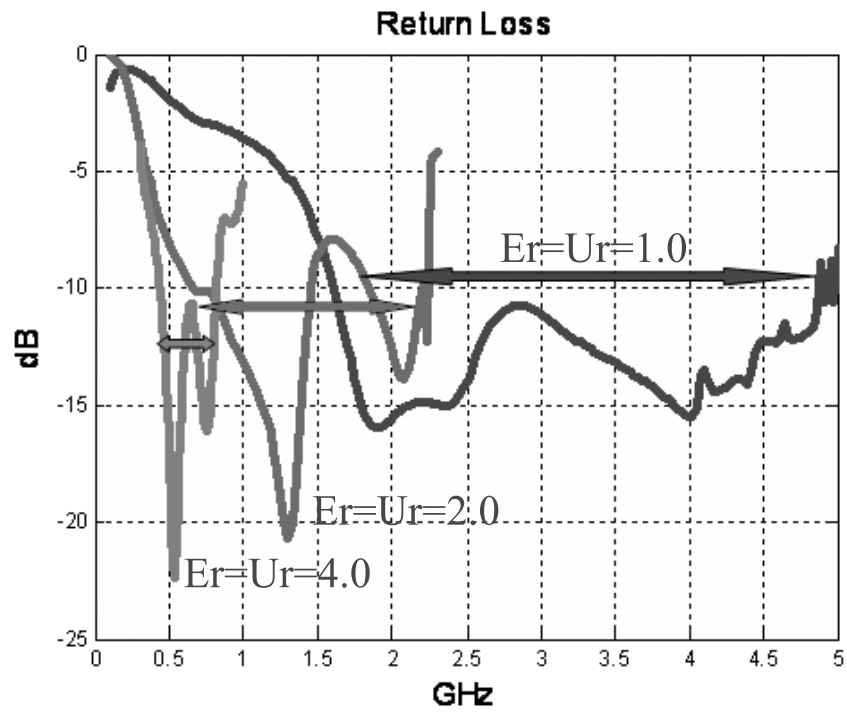


Figure 2.13: The impedance bandwidths of a four-point antenna embedded in impedance matched materials.

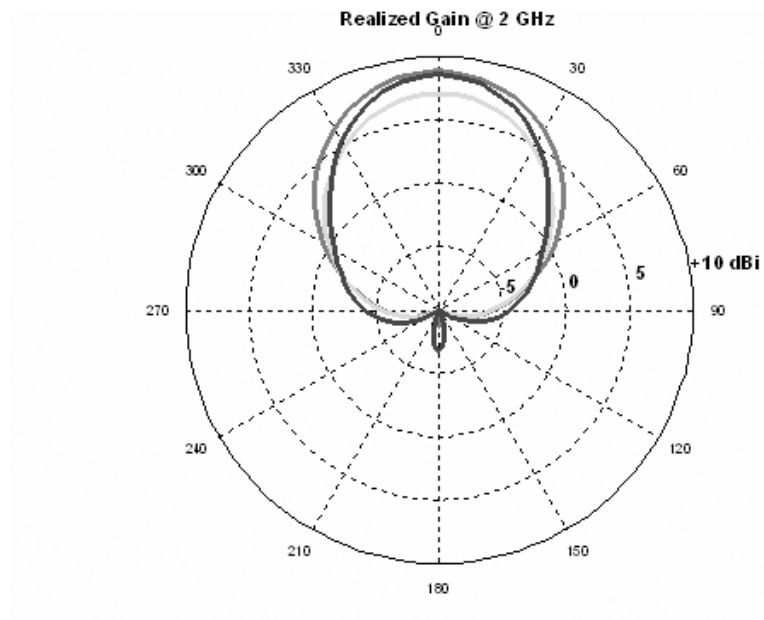


Figure 2.14: The radiation patterns of a four-point antenna embedded in impedance matched materials.

Table 2.5: Impedance Matched Material Embedded Four-Point Antenna

Magneto-Dielectric	Gain (dBi)	Bandwidth %	Scaling (λ_{L0}/λ_L)
$\mu_r=\epsilon_r=1.0$ (Air)	8.8	101%	1.00%
$\mu_r=\epsilon_r=2.0$	8.2	108%	2.46%
$\mu_r=\epsilon_r=4.0$	8.5	85%	3.65%

2.3.2 Z-Phase Hexaferrite

The Z-Phase Hexaferrite developed in conjunction with the Trans-Tech corporation ($3\text{BaO}\cdot 2\text{CoO}\cdot 12\text{Fe}_2\text{O}_3$) has been permeability enhanced to $\mu_r = 16$ by exposure to a high power magnetic field during processing (Figure 2.15). The relative permittivity, $\epsilon_r=16$ and was found to be non-dispersive up to at least 1.5 GHz. The Electric Loss Tangent was less than 5×10^{-3} across this range and was . The resulting ceramic is impedance matched along two axis (XY).

Up to 400 Mhz the Z-phase Hexaferrite is impedance balanced ($\epsilon_r = \mu_r = 16$) and the magnetic loss tangent is approximately 2×10^{-2} at 400 MHz.

2.4 Chapter Conclusions

The limitations of modern magnetic materials to meet the needs of microwave engineers have been presented. Chief among these is that magnetic materials exhibit either too high a loss tangent, or no magnetism at all ($\mu_r = 1$) in the microwave region. This condition is due to the gyromagnetic resonances in these materials occurring at frequencies which are not far enough above the desired operating frequency.

A newly developed Z-phase hexaferrite which represents the upper limits of modern materials technology is presented. This material achieves moderately acceptable loss factors and an impedance matching condition up to approximately 400 MHz.

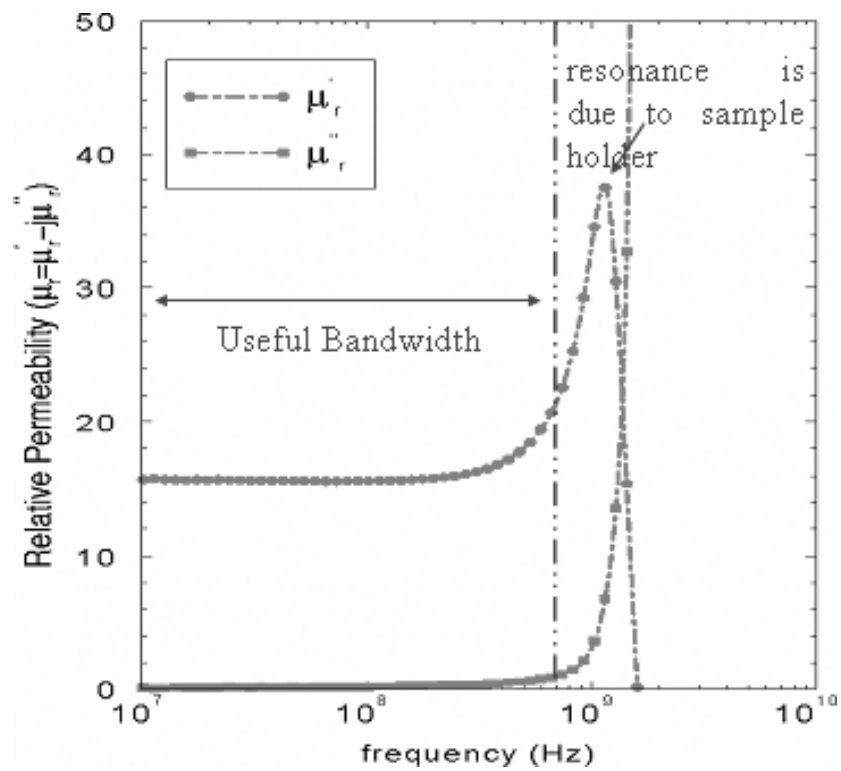


Figure 2.15: The permeability of the Z-phase hexaferrite was measured and found to be non-dispersive below approx 500 Mhz. The measurement also showed that it is low-loss.

CHAPTER 3

Metamaterials

MetaMaterials are a new class of ordered nanocomposites that exhibit exceptional properties not readily observed in nature. These properties arise from qualitatively new response functions that are: (1) not observed in the constituent materials and (2) result from the inclusion of artificially fabricated, extrinsic, low dimensional inhomogeneities.

Dr. Valerie Browning

3.1 Chapter Introduction

Metamaterials is a modern term used to describe engineered materials composed of electrically small elements that exhibit properties not observed in the materials the elements are made of themselves.

In this chapter I will be introducing the most popular modern metamaterials, the split-ring resonator and the metallic wire medium. I will also introduce a metamaterial of my own design, the embedded circuit spiral resonator. The properties of this material will be described, and a design procedure will be outlined.

3.2 Meta-Materials Background

Although engineered materials which seem to fit the modern definition of Meta-material have existed for since at least the 1950's ([8],[9],[10],[11],[12], and [13]) under various names such as metamaterials, artificial materials, and photonic crystals [14], the current popular research interest in this field is a result of recent advances in engineered magnetics [1].

3.2.1 The split ring resonator for permeability (μ_r)

When an magnetic field is incident normal to the ring-plane of a split ring resonator metamaterial, a current is induced in the ring elements (Figure 3.1). This circulating current generates a magnetic moment normal to the ring plane and this magnetic moment is the metamaterial equivalent to the atomic magnetic dipole moment of naturally permeable materials.

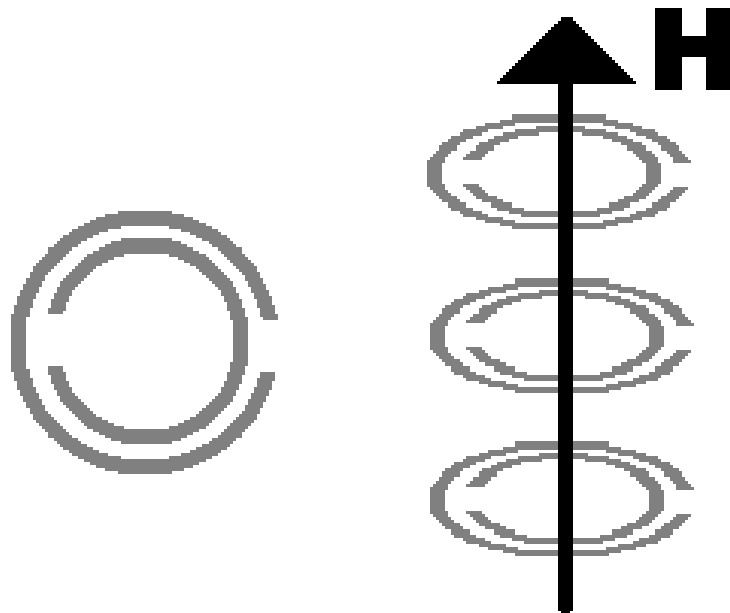


Figure 3.1: The split-ring resonator proposed by Pendry et. al. ([1]).

Due to the geometric requirement that the magnetic moment be normal to the ring plane, a geometry such as figure 3.2 is necessary to achieve isotropic performance.

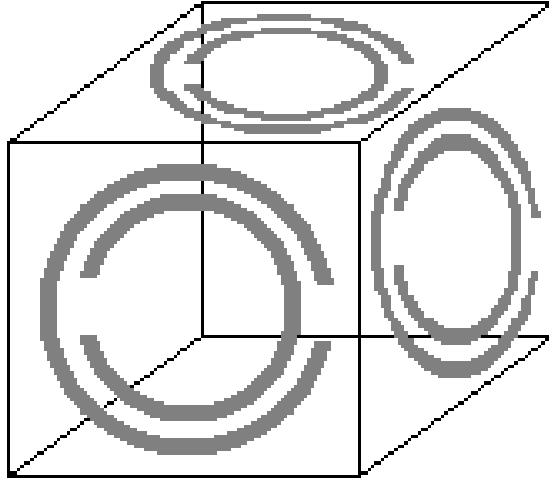


Figure 3.2: The unit-cell geometry for an isotropic split-ring resonator metamaterial.

Figure (3.3) shows the bulk permeability for an isotropic split-ring resonator as designed by Pendry [1] in which the permeability is described by (3.1).

$$\mu_r = 1 - \frac{F\omega}{\omega^2 - \omega_0^2 + i\omega\Gamma} \quad (3.1)$$

The salient phenomena of interest are as follows, in the spectral region below resonance the metamaterial exhibits an enhanced permeability ($\mu_r > 1$), as resonance is approached both the magnetic permeability and the magnetic loss mechanism (μ_{imag}) increases significantly, and in the region immediate above resonance the magnetic permeability is negative (Figure ??).

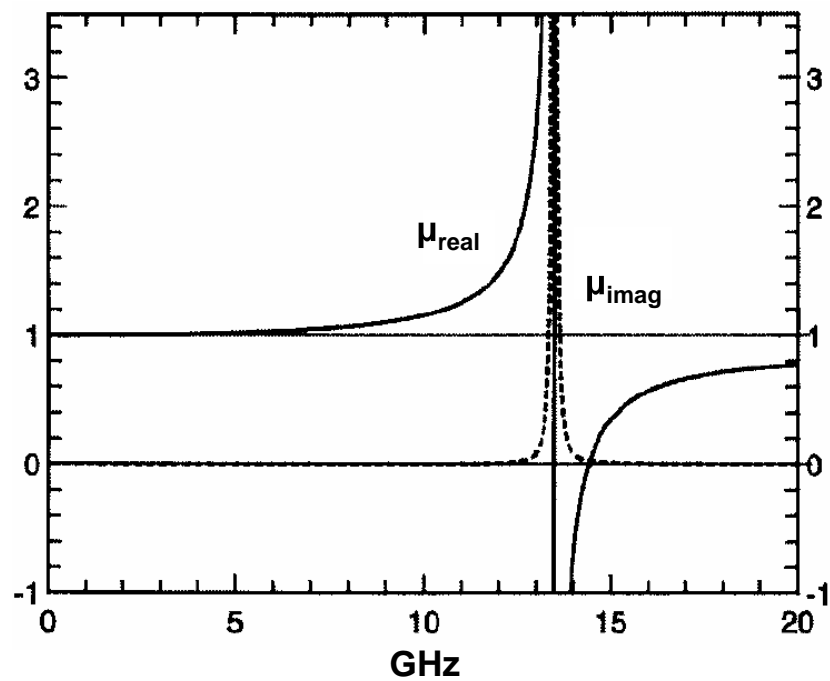


Figure 3.3: Complex Permeability of a bulk medium composed of split-ring resonator metamaterials.

3.2.2 The metallic dipole for permittivity (ϵ_r)

It is possible to engineer the permittivity of a bulk medium by means of metallic inclusions [15]. An array of wire elements with periodic gaps exhibit permittivity according to the Drude-Lorentz model. Such wires appear as small dipoles, similar to the electric dipoles of atomic and molecular systems in natural materials. The effective permittivity for a periodic wire medium is

$$\epsilon_r = 1 - \frac{\omega_p^2 - \omega_0^2}{\omega^2 - \omega_0^2 + i\omega\Gamma} \quad (3.2)$$

where ω_p is the plasma frequency ω_0 is the resonance frequency. These parameters are a function of the wire lattice geometry so are tunable for any given application. When $\omega_0 < \omega < \omega_p$, the permittivity is negative and, because the resonant frequency is often set to $\omega_0=0$ by using continuous wires interesting phenomena, including negative ϵ which are only found in natural materials at optical frequencies can be reproduced at almost any desired frequencies, even as low as a few megahertz.

3.2.3 Left-Handed Medium and the Negative Index of Refraction

With mechanisms for producing both negative permittivity, and negative permeability available, the question of combining these phenomenon becomes relevant. In 1968 Veselago [16] mathematically investigated the phenomenon involved of negative permittivity and/or permeability long before such materials were developed.

Veselago determined that if either ϵ_r or μ_r were negative, the material would not support the propagation of electromagnetic waves. This phenomenon came to be known as an 'electromagnetic band gap' phenomenon [17]. Of more interest to most modern researchers was that Veselago also determined that if both ϵ_r and μ_r were negative then the medium would support the propagation of waves but that the wave-

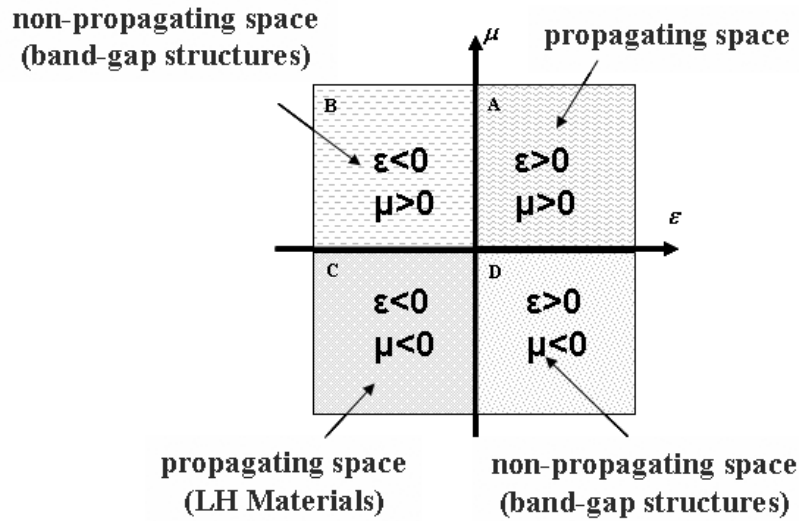


Figure 3.4: In most natural materials at microwave frequencies both ϵ_r and μ_r are positive.

equations in such a medium would follow a curious set of dual properties to normal materials where both ϵ_r and μ_r are positive [18].

Such a 'Double-Negative' material came to be called a 'Left-Handed' material in recognition of the left-handed triplet which the propagation vector forms with the electric and magnetic fields [[5], [19]]. When the the dielectric constant (ϵ_r) and the magnetic permeability (μ_r) are both negative then waves can still propagate, since the product ($\epsilon\mu$) is positive and causes a backward wave for which the phase of the waves moves in the direction opposite to the direction of the energy flow. In such a case the refractive index for Snell's law is negative and a wave exiting such a medium experiences a negative refraction angle at an interface with a natural material where ϵ and μ are both positive.

The most popular application of modern research for such a double-negative, or left-handed, material is in the development of electromagnetic lenses ([20], [21], [22], and [23]), but other creative applications are also being investigated [24].

For our purposes though, the interesting applications of metamaterials will be for

their positive enhancement of permeability, and the use of a negative permeability, positive permittivity material as an EBG insulator.

3.3 Embedded Circuit Spiral Resonator Metamaterial

In this project we developed and experimentally validated engineered magnetic materials with properties that do not exist in natural materials. We experimentally demonstrate a technique of producing magnetic properties in an engineered material using only non-magnetic component elements [[25],[3]]. The application chosen to demonstrate the magnetic permeability of this engineered material, which will be referred to as a *metamaterial*, is that of a miniaturized patch antenna above a ground plane and is presented in a later chapter. The patch antenna application calls for low-loss operation with a specifiable relative magnetic permeability at frequencies where low-loss magnetically permeable materials do not already exist.

For low-loss applications in the microwave region natural material choices are effectively limited to non-magnetic dielectrics. Unfortunately, for natural magnetic materials the upper frequency end of the magnetic region for high quality ferrites is limited by the gyromagnetic resonances and occurs in the VHF-UHF range, too low a frequency for microwave applications.

In the last chapter we introduced Z-phase Cobalt HexaFerrite which was created in joint development with the TransTech corporation. This Z-phase Cobalt HexaFerrite is representative of the current upper-frequency limit for low-loss magnetic permeability from natural materials. The admittedly subjective maximum 'useful' frequency for this material is approximately 500 MHz. To our knowledge there is no material currently available with moderately low loss ($\tan\delta_m = \frac{\mu''}{\mu'}$ < 0.02) and moderately enhanced permeability ($\mu'_r > 2$) for operation in the microwave region.

An engineered material such as our metamaterial which can fit this need would be quite useful.

3.3.1 Benefits of Magnetic Materials

The permittivity of a composite dielectric can be selectively engineered by the mixing of low and high dielectric materials to provide low-loss and high performance throughout the microwave operating region for practically any desirable permittivity. For example, Alumina (Al_2O_3) has a dielectric constant of approximately $\epsilon_r=10$ ($\tan\delta_e \leq 3 \times 10^{-4}$ at 10 GHz) and can be mixed in controlled ratios with lower dielectric filler materials to achieve any desirable dielectric constant from $\epsilon_r=2-10$ while maintaining an acceptably low loss factor. Similar, but more challenging to process is Titania (TiO_2) which has a very low dielectric loss tangent ($\tan\delta_e \leq 1 \times 10^{-3}$ at 10 GHz) and a dielectric constant of close to $\epsilon_r=100$, which opens up the entire possible range of dielectric values [26]. In contrast to the wide variety of low-loss dielectrics available covering a wide range of permittivities, the permeability of low-loss natural materials and their various composites are effectively limited to that of free space (μ_r) in the microwave region.

For current microwave applications, dielectric materials must be selected to achieve the desired electromagnetic phenomenon of the application goals. High dielectric constant materials are used to achieve electromagnetic scaling, field confinement, and other useful benefits. Restricting extremely high dielectrics from many desirable applications is the dramatic mismatch in wave impedance for the material relative to the system feed network and free space.

If the relative permeability can be increased from that of free-space ($\mu_r > 1$), the product of μ and ϵ increases quickly, providing miniaturization and electromagnetic scaling ($\lambda_{medium} = \frac{\lambda_0}{\sqrt{\mu_r \epsilon_r}}$). In a patch antenna the majority energy storage is capacitive energy in the electric field between the patch and underlying ground plane. By

increasing the amount of magnetic energy storage, the magnetic-electric imbalance is reduced and the system bandwidth automatically improves [27]. Since the patch antenna geometry is so strongly capacitive, a $\mu_r > \epsilon_r$ condition would be preferable in terms of balancing energy storage mechanisms. In terms of minimizing the free energy trapped within the substrate, a $\mu_r = \epsilon_r$ condition would be preferred. As relative permeability increases to match relative permittivity, the intrinsic impedance of the medium ($\eta_{medium} = \sqrt{\frac{\mu_r \mu_0}{\epsilon_r \epsilon_0}}$) approaches that of free-space ($\eta_0 = \sqrt{\frac{\mu_0}{\epsilon_0}}$). It is the difference in intrinsic impedances η_0 and η_{medium} which determines the impedance mismatch reflection coefficients at the interface. Obviously we can benefit from being able to control this factor independently of λ_{medium} .

The benefit to minimizing the energy loss due to the reflection at this interface is obvious and further anticipated benefits are improvements in matching and bandwidth as a result of increasing the proportion of magnetic energy storage. Benefits in improved input matching for miniaturized devices and elimination of trapped surface waves can offer significant potential benefits for microstrip antennas if losses due to the metamaterial are minimal.

As we will show, the embedded circuit spiral resonator metamaterial provides a permeability which varies from $\mu_r=1-5$ over a reasonable operating band. This property allows the designer to make an efficiency/miniaturization tradeoff with a single substrate material. For a specified efficiency level the maximum miniaturization factor may be selected, thereby enabling various antennas to operate on the same physical metamaterial substrate while each exhibits a different miniaturization factor and efficiency.

Natural Magnetic Materials

The bulk permeability of a material is a quantitative description of its magnetic susceptibility, or how readily the material experiences magnetization wherein the

materials charges align their motion in response to an externally applied magnetic field.

A circulating charge produces a magnetic moment, and the magnetic moments of atoms are the building blocks of natural magnets. The macroscopic magnetic properties of materials are the consequence of the magnetic moments of individual electrons. In the presence of a magnetic field, the magnetic moments of a material with $\mu_r > 1$ tend to become aligned with the applied field and to reinforce it by virtue of their own magnetic fields.

The challenge to microwave applications arises from the inertia of atomic systems. Although the mass of an electron is small, it is not zero and the attempts of the electrons magnetic dipole moments to track an externally applied magnetic field deteriorate and eventually fail altogether for inertial reasons as the excitation field approaches and passes the materials gyromagnetic resonance frequency. As gyromagnetic resonance is approached, the materials loss-factor increases dramatically and above resonance the material becomes essentially non-magnetic. Unfortunately for microwave engineers, magneto-dielectrics produced from natural materials exhibit gyromagnetic resonance in the VHF-UHF region and are unusable for low-loss microwave applications.

If a mechanism similar to the operating of natural magnetics can be developed for microwave operation by synthetic means, then low-loss operation may be pushed into the microwave region and low-loss microwave magneto-dielectrics may become a reality. Already, various researchers have proven that it is possible to replicate magnetic behavior by inserting electromagnetically small metallic inclusions into a natural dielectric. [[25],[3],[1]].

3.3.2 Embedded Circuit Meta-Materials

In 1968 Veselago [16] theoretically investigated the physics of materials with negative permeabilities and permittivities. Veselago determined that 'band-gap' and 'Left-Handed' behaviors occur when either permeability, permittivity or both are negative.

Recent experimental work builds upon the theoretical development for left handed materials provided by Veselago and is perhaps the most popular area of research for embedded circuit metamaterials [5]-[28].

We will show that the embedded circuit spiral resonator achieves enhanced positive magnetic permeability and electric permittivity for low loss microwave applications.

The concepts of using embedded circuits to enhance dielectric properties or achieve magnetic properties in an otherwise non-magnetic medium are not new, but we believe have not received adequate attention when the significance of the potential benefits are considered. In one relevant example, Saadoun and Engheta investigated a theoretical material they called the "omega" medium in the mid 1990's [4]. Their "omega" medium is composed of a host material with small inclusions shaped like the Greek letter "omega" (see Fig. 3.5). Their theoretical analysis of electromagnetic wave interaction with the circuit model for such a medium showed both an effective permittivity and an effective permeability thus establishing both dielectric and magnetic enhancement.

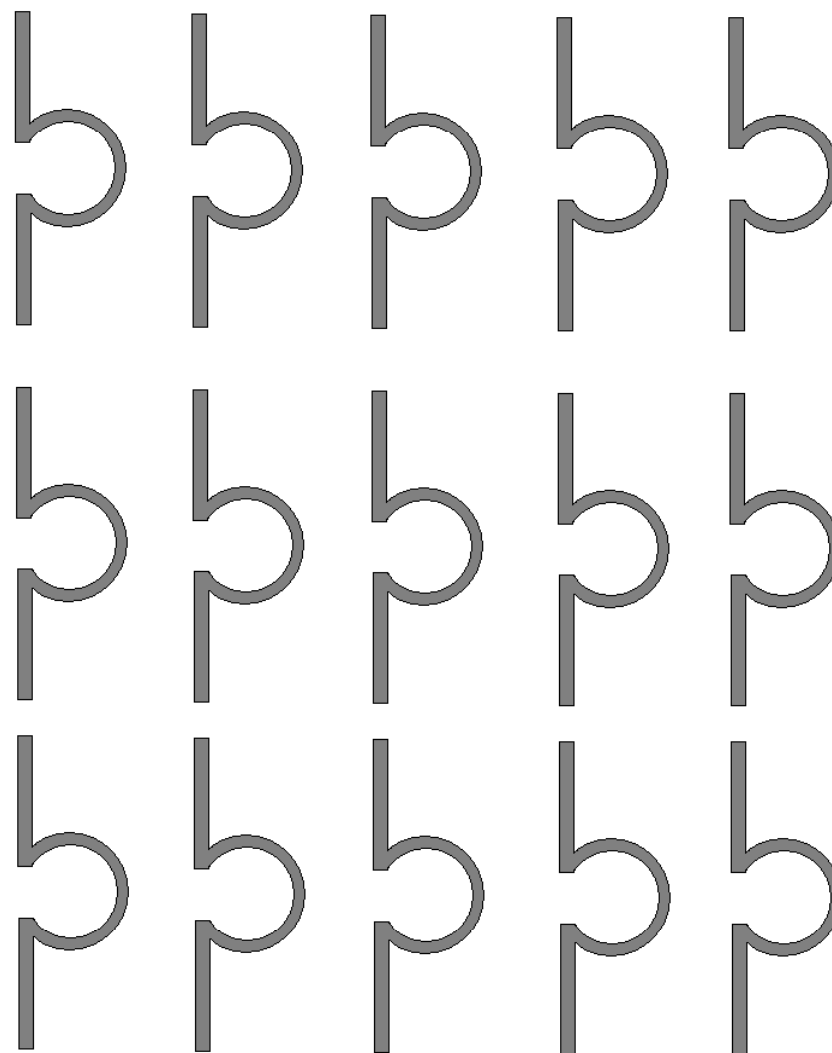


Figure 3.5: A medium with metallic inclusions in the shape of the greek letter "omega". The "omega" medium exhibits enhancement of both the magnetic and dielectric properties over the host material in certain frequency regions, determined by the circuit resonances.

Recently, geometries optimized to provide superior magnetic properties have been considered theoretically [25], [1] but to our knowledge none have been proven useful in practical experimental application.

Our circuit geometry is engineered to control energy coupling and storage. The benefit of this control is that within the limits of the processing technology the effective permittivity and most importantly the effective permeability of the medium can be tailored to the demands of the application.

3.3.3 Effective Medium Operation

The storage of energy in magnetic fields is the definitive characteristic of a magnetically permeable material. When magnetic energy storage is achieved by means other than atomic electron orbital or spin phenomenon an engineered effective bulk permeability is observed. The basic circuit unit for magnetic energy storage is the inductor and an electromagnetically small inductor embedded into a dielectric material will store coupled magnetic energy in a manner similar to the means by which magnetic energy is stored in the electron orbital or spin motion of materials exhibiting natural magnetic permeability. This embedded circuit magnetic energy storage imparts an effective bulk permeability to the material.

Figure 5.2 shows a single element of an embedded circuit capable of producing magnetic properties in a natural dielectric. The spiral loop acts as an inductor, coupling energy from an incident magnetic field to produce a current loop in the spiral. There is a distributed capacitance between the loops of the spiral, and the interaction between the spiral inductance and spiral capacitance causes the resonant behavior. Near resonance the current magnitude in the spiral loop increases and the magnetic permeability is enhanced.

To achieve an effective medium behavior the embedded circuits must be distributed uniformly through the host dielectric. Planar microstrip processing is em-

ployed to form a two-dimensional array of the resonant spirals (see Fig. 3.7) and the resulting substrate-metallization layers are stacked to form a three dimensional effective medium. This method of assembly allows for the critical control of geometrically determined circuit parameters and thereby selection of resonant frequency and coupling factors.

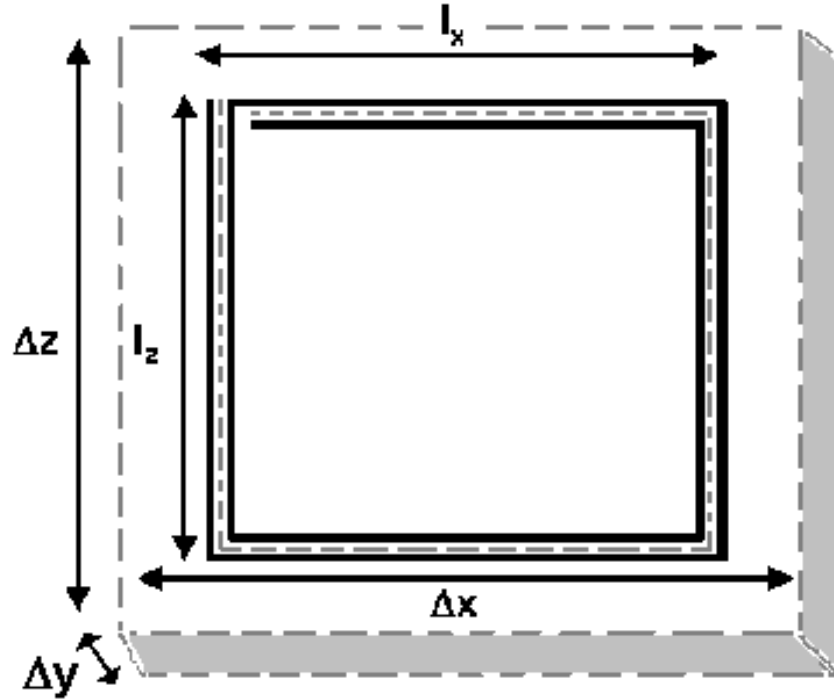


Figure 3.6: The metamaterial unit cell. Δ_x , Δ_y , and Δ_z is the unit cell size. In this diagram $N = 2$ is the number of wraps of the spiral. To achieve permeability enhancement, the magnetic field shall be aligned along the Y axis (normal to the page) and the electric field shall align along either the X or Z axis.

3.3.4 Equivalent Circuit Model

Our effective medium employs passive embedded circuits embedded in a dielectric medium for which we have developed the theoretical analytical models predicting material performance [[25],[29]]. Previous researchers have developed means of achieving magnetism from passive embedded circuits conductors [4],[1] and this work builds

upon the existing state of the art. One of our previous designs consisted of a single square spiral with an interdigitated capacitor providing lumped element capacitance-like performance and is shown in figure 3.8 beside other magnetic embedded circuit resonators [3].

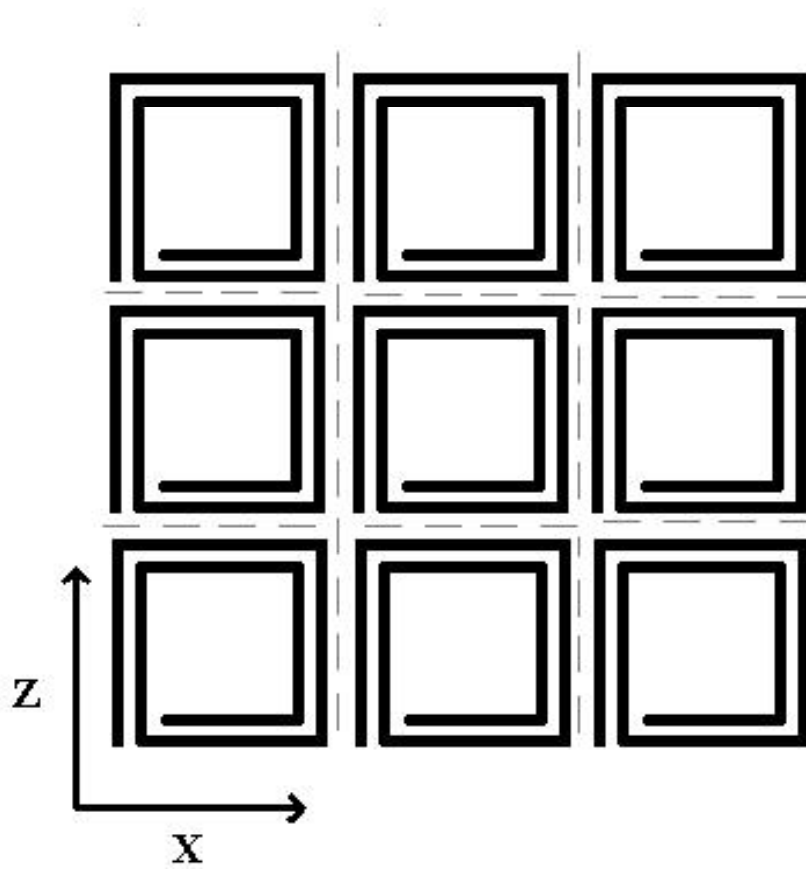


Figure 3.7: Infinite Metamaterial Medium. A passive 2D XZ array of elements shown in Fig. 5.2. These circuit boards can be stacked in the Y dimension to approximate an infinite magnetic medium.

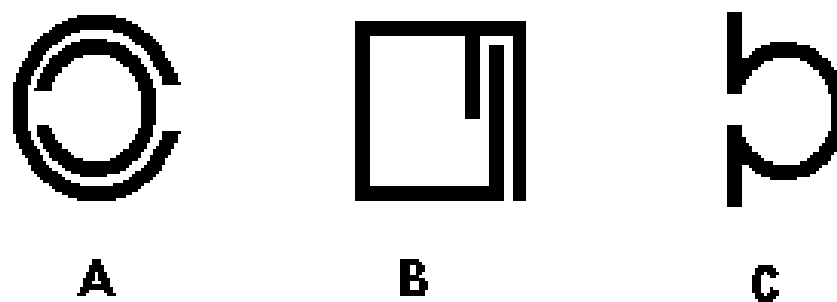


Figure 3.8: Previous Magnetic embedded circuits A) Split-Ring Resonator B) Square LC Resonator C) 'Omega' Medium Resonator.

One draw-back of this square LC resonator is its non-optimal use of unit cell area. A good design for optimal magnetic permeability would 'enclose' as much of the unit-cell area as possible to achieve the highest coupling of incident magnetic energy while maximizing packing density. A square inductive loop seems to be a reasonable candidate and was the choice of our previous design. An interdigitated capacitor seemed like a reasonable choice to provide the capacitance with which the inductive loop would resonate but we have since concluded that this is a non-optimal use of the unit-cell area inasmuch as that the interdigitation consumes too much valuable space inside the inductive loop and thereby inhibits optimal coupling to the incident magnetic field. We have since concluded that a spiral loop is preferable inasmuch as it uses less area to provide equivalent capacitance while simultaneously providing additional inductance, and hence additional permeability.

These embedded circuits (Fig. 5.2) couple incident magnetic energy to their inductive elements and store the energy in an LC resonator.

The basic design equations for the spiral loop circuit would be helpful in understanding the operation of the metamaterial. Useful design equations would need to provide approximate lumped element values for the distributed capacitance and inductance of a flat spiral inductor.

Although a theoretically rigorous analysis of the embedded circuit metamaterial is not available, a simple preliminary model is available which provides an intuitive understanding of the EC metamaterial behavior. For quantitative precision, numerical simulation is best employed as the second step in metamaterial design.

Towards the end of maximum physical understanding with only moderate analytic complexity the spiral loop of Figure 5.2 may be most simply modeled as an LC resonator as shown in Figure 3.9. This simple resonator interacts with its host medium in a manner similar to the well studied behavior of a plasma near its resonance, and hence the composite transmission-line equivalent model for the resonator is very

similar to that for a plasma. Incorporating the spiral loop loss mechanisms (R_{spiral}), the equivalent circuit model for the composite medium is given in Figure 3.10. Figure 3.10 can best be interpreted as a classic RLGC transmission-line model for a medium, with an embedded LC resonator inductively and capacitively coupled to it.

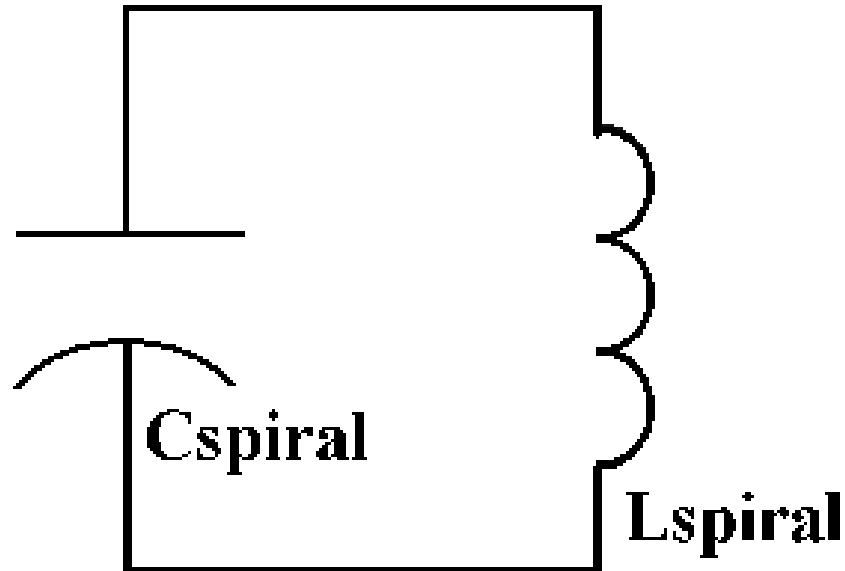


Figure 3.9: The spiral loop equivalent lumped-element circuit model.

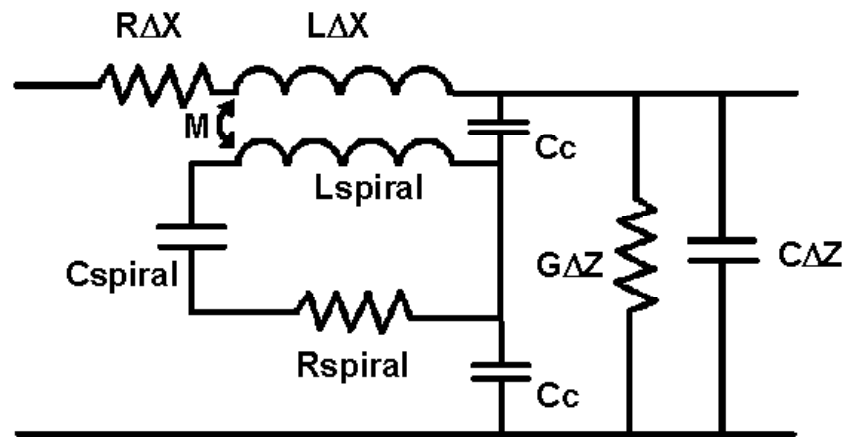


Figure 3.10: Transmission-line equivalent model for magnetic metamaterial.

For the derivation of the circuit models and equations (3.3)-(3.14) of this section the interested reader is directed to the reference [30]. What follows here is a sig-

nificantly expanded explanation and discussion of the design and validation process employing these methods for a more practical planar embedded circuit geometry.

Capacitance

To model the equivalent lumped-element capacitance (C_{spiral} in Figure 3.9) of the spiral loop (Fig. 5.2), the primary capacitive effect to be considered is the capacitance between adjacent wraps of the spiral inductor.

Additional smaller capacitances will result from the interaction between non-adjacent wraps, but only considering the adjacent wraps should give a preliminary understanding of the physics involved. These additional capacitances will be especially significant in cases where loops have greater than 2 wraps of the spiral arm. In this case the nearest capacitive effect not included in the model is only twice the distance of the included elements.

The distributed capacitance of the spiral inductor embedded in the host dielectric can be determined by considering the geometry of the "capacitive spiral" indicated in Figure 5.2 by a dotted line which traces the path between the metallic spiral arms. The value of capacitance can be computed from (3.3) where L_{SG} is the length of the spiral gap given by (3.4) and the gap fraction g is given by (3.5).

$$C_{spiral} = \epsilon_{diel} \frac{K(\sqrt{1-g^2})}{K(g)} L_{SG} \quad (3.3)$$

$$\begin{aligned} L_{SG} = & 2n(lz + lx) \\ & - w[(2n+2)\frac{2n+1}{2} - 1 + (2n+1)n] \\ & - s[(2n+1)n + (2n)(\frac{2n-1}{2} + \frac{1}{2})] \end{aligned} \quad (3.4)$$

$$g = \frac{\frac{s}{2}}{\frac{s}{2} + w} \quad (3.5)$$

$$K(g) = \int_0^{\frac{\pi}{2}} \frac{d\phi}{\sqrt{1 - g^2 \sin^2 \phi}} \quad (3.6)$$

The basic form of the capacitive equation (3.3) is the capacitance per unit length of co-planar thin metallic strips multiplied by the length of the strips and the dielectric constant of the host medium. An elliptical integral (3.6) exists for determining the capacitance per unit length. In equations (3.3) - (3.5) the metallization thickness is assumed to be zero, $\epsilon_{diel} = \epsilon_{rdiel}\epsilon_0$ where ϵ_0 is the permittivity of free-space, the width of the trace metallization is indicated by 'w' and the inter-trace gap spacing is 's' (see Fig. 3.11).

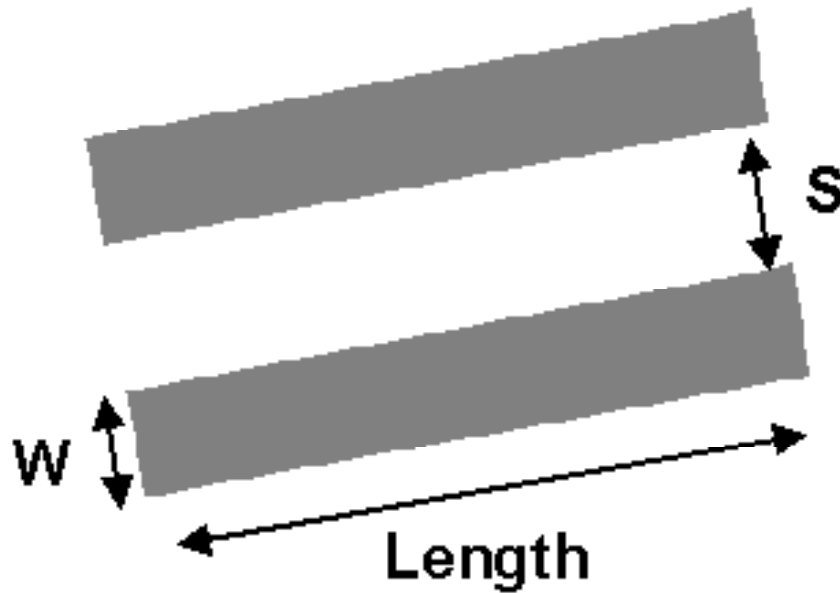


Figure 3.11: Geometry for (3.5) to calculate capacitance of two flat coplanar metallic strips.

Equation (3.4) is an analytic formula for the length of the spiral gap. If N is the number of turns of the metallic spiral arm, then $n=N-1$ is the number of turns of the capacitive spiral gap. This formula is correct for integer or half-integer values of N , and integer/4 values if $lx = lz$. For other values of N , the analytic formula provides a reasonable estimate to first order.

For our 250 MHz design $lx = lz = 16mm$, $w = s = 0.127mm$ and $L_{SG} = 6.24mm$. Then for a Rogers RO-4003 dielectric host medium $\epsilon_{rdiel} = 3.38$ and $C_{spiral} = 5.3pF$.

Although this estimate of capacitance is acceptable, it does neglect additional capacitances between spiral elements in adjacent different metamaterial unit cells, corner and gap-end effects, as well as capacitance between non-adjacent wraps, nor does it account for the air-gap between stacked layers (see Fig. 3.12). For these reasons the capacitance predicted by equation (3.3) will be at best a rough approximation of the actual capacitance. Nevertheless (3.3) provides useful insights into the behavior of the embedded circuit and is a useful starting point for design so is worthy of consideration.

Inductance

The planar elements in Figure 3.7 are stacked along the Y-dimension with a spacing of Δy . This geometry effectively forms a solenoid along the Y-axis of spiral loop elements and due to the long-solenoid structure, a uniform field distribution can be assumed. This observation provides the starting-point for modeling the spiral inductance. With this estimate in mind, for low values of spiral turns N , the inductance of a single spiral loop can be derived from (3.7) where 'S' is the cross-sectional area of the spiral.

$$L_{spiral} = \mu_0 \frac{N^2}{\Delta y} S \quad (3.7)$$

For our geometry, $\Delta y = 3.028mm$, $N = 2$, and $S \approx 2.56 \times 10^{-4}m^2$. The induc-

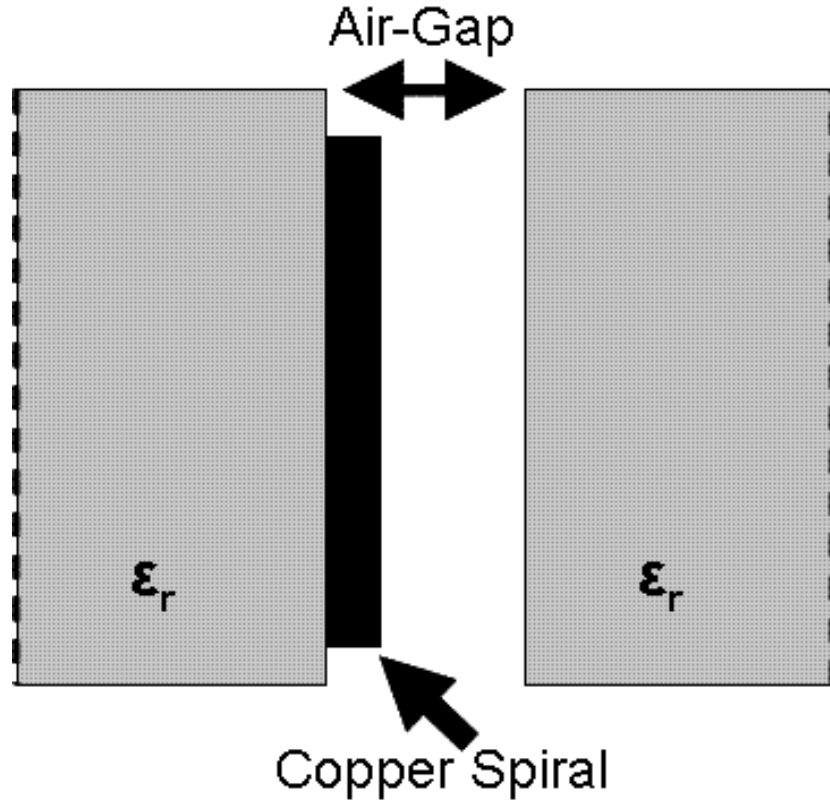


Figure 3.12: The air gap caused by substrate warpage decreases the effective capacitance of the spiral resonator, increasing the metamaterial resonance frequency.

tance of a single spiral loop element provided by (3.7) is just slightly higher than the real value due to imperfect 'fill-ratio'. Basically (3.7) assumes perfect magnetic linkage between all concentric loops of the spiral. Choosing an average area for the spiral (such as the area enclosed by the dashed line in figure 5.2) should account for the discrepancy. As in the capacitive calculation the simplifying approximations of this calculation limits its accuracy. In addition to the imperfect magnetic linkage mentioned, a significant deviation from ideality occurs in that the current on each spiral element is forced to go to zero at its ends, a condition which does not exist in ideal solenoidal wrapped wires which (3.7) represents. Nevertheless it is illustrative to consider the inductance for our geometry, which is $L_{spiral} = .425\mu H$.

Resonance

Once the distributed capacitance and inductance of the spiral loop are known from the methods above, the resonance frequency of the embedded circuit can be estimated from

$$F_{res} = \frac{1}{2\pi \times \sqrt{L_{spiral}C_{Spiral}}} \quad (3.8)$$

The estimate of resonance frequency from (3.8) is generally low. This estimation is partially due to estimation error of capacitance and inductance, but is also caused by the distributed nature of capacitance and inductance being poorly modeled by lumped elements. Equation (3.8) treats the capacitance and inductance as lumped values (as in Fig. 3.9) whereas they are actually distributed. For our substrate design (3.8) predicts a resonance frequency of 106 MHz, a dramatic underestimate of the realized values. At significantly increased complexity the lumped values C_{spiral} , and L_{spiral} may be distributed in a geometry more closely representing the actual spiral geometry (Fig. 3.13). This more accurately represents the interaction between the distributed capacitance and inductance, predicting a much higher resonance frequency of 183 MHz, but it is still too low relative to the actual spiral resonance and is not satisfactory for design purposes.

To more accurately model the medium, a finite element solver such as the commercially available HFSS is helpful. Perfect Electrically Conducting (PEC) walls and Perfectly Magnetically Conducting (PMC) boundary conditions around a single element unit can be employed to enforce symmetry conditions which would exist in an infinite YZ plane of embedded circuits under plane wave illumination at normal incidence as shown in Figure 3.14.

The resonant frequency derived by this numerical simulation method will be quite accurate, although experimental errors will remain. For example, small air-gaps be-

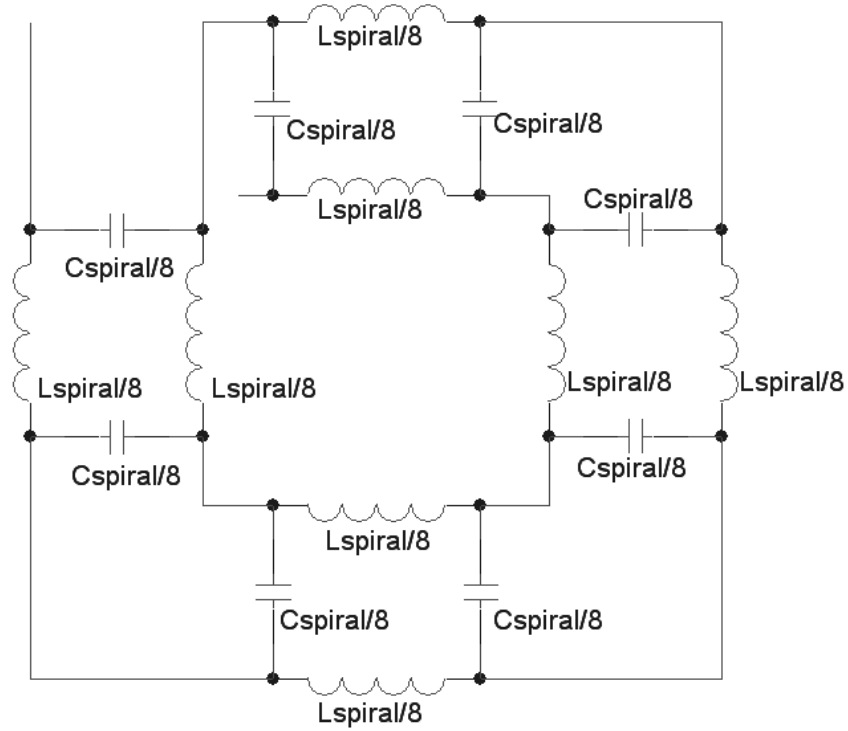


Figure 3.13: A higher order spiral loop equivalent circuit model.

tween layers stacked in the Y-dimension may slightly decrease capacitance for physically realized materials and increase resonance frequency by ten or twenty percent if not accounted for in the numerical simulations.

Effective Medium

In order to form an effective medium as represented by this model, a planar array of the unit-cell of Figure 5.2 is printed onto an XZ planar surface. These infinite XZ grid planes may be stacked infinitely in the Y dimension to form a 3D infinite medium.

Analytic formulations for the effective bulk permittivity and permeability of such embedded circuit meta-materials exist which correlate to the geometry of Fig. 3.10 [25]. The permeability and permittivity of such a medium are given in Figure 5.4.

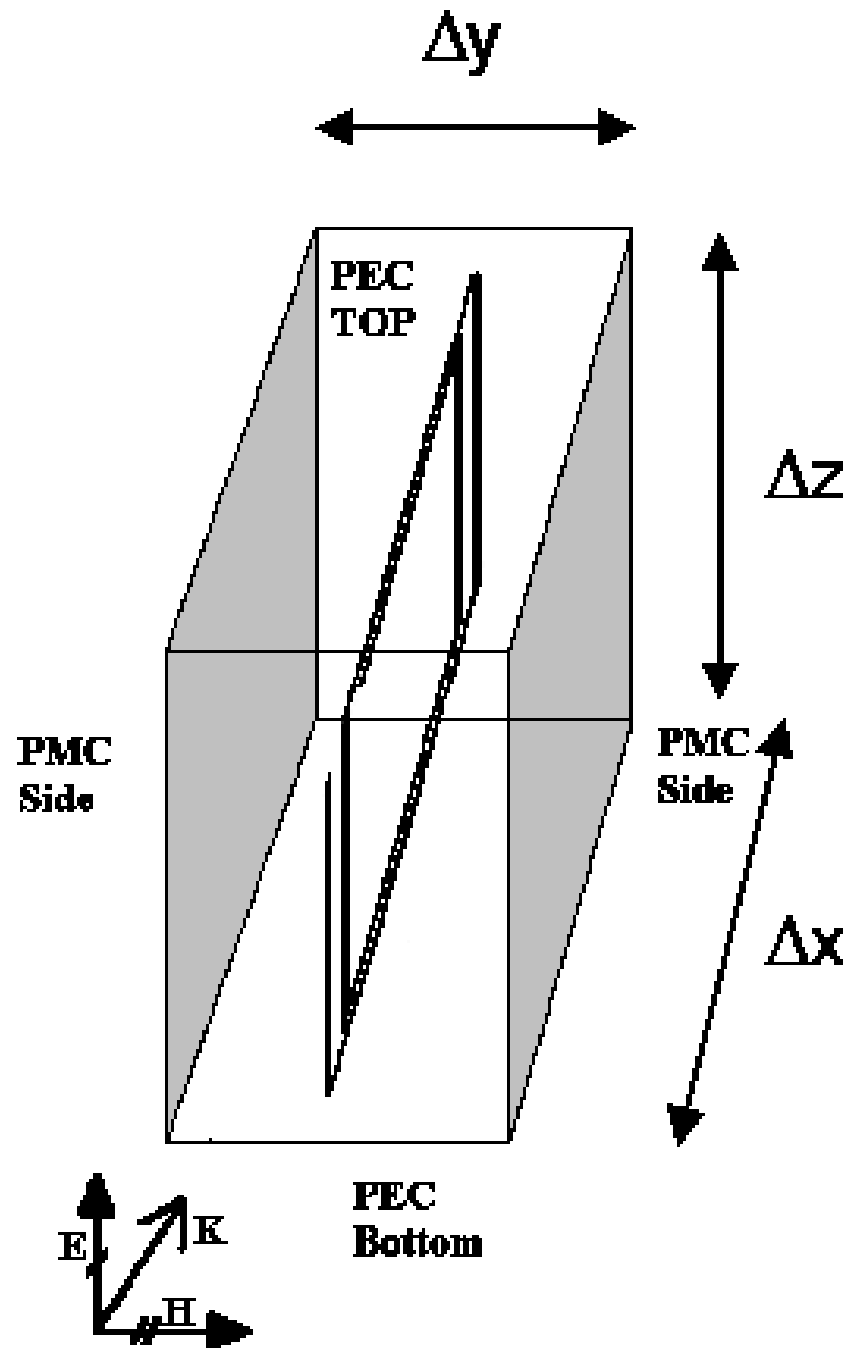


Figure 3.14: FEM boundary conditions to test resonance frequency.

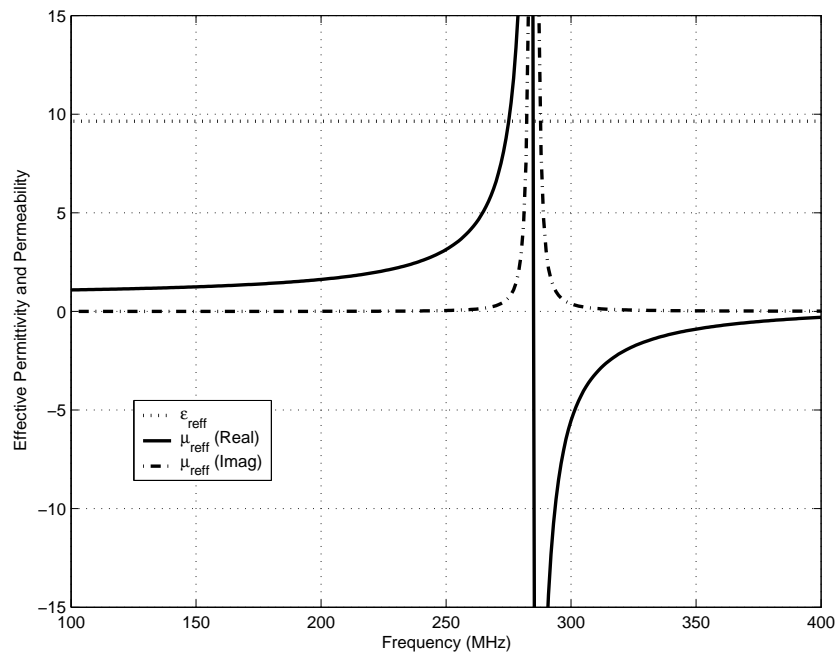


Figure 3.15: Relative Permittivity, and Permeability of metamaterial. At 250 MHz $\epsilon_{r(\text{meta})} = 9.8$, $\mu_{r(\text{meta})} = 3.1$, and $Tan\delta_m$ 0.014.

Permeability

Equation (3.9) gives the form of the anisotropic magnetic permeability. The effective-medium design provides permeability enhancement only along the solenoidal axis which is parallel the Y axis. Any incident magnetic field of X or Z orientation will not couple to the inductive loops of Figure 3.7 and the permeability μ_r experienced by these components will be that of free-space.

For a Y oriented time-harmonic magnetic field, incident magnetic energy induces currents in the circuit loop coupling energy into the resonators and changing the relative permeability of the medium. The current loop induced generates its own magnetic field, storing magnetic energy and thereby changing the magnetic susceptibility.

$$\bar{\mu} = \begin{bmatrix} \mu_0 & 0 & 0 \\ 0 & \mu_{eff} & 0 \\ 0 & 0 & \mu_0 \end{bmatrix} \quad (3.9)$$

$$\mu_{eff} = \mu_0 \left(1 - \kappa^2 \frac{1}{1 - \frac{\omega_p^2}{\omega^2} - j/Q} \right) \quad (3.10)$$

Effective permeability (μ_{eff}) given by (3.10) and is a function of the resonant frequency of the spiral inductors ($\omega_p = 2\pi \times F_{res}$), the frequency of the incident field ($\omega = 2\pi \times F$), the resonator quality factor 'Q' and the coupling coefficient of Y-directed magnetic energy κ . Figure 5.4 shows a typical response of μ_{eff} to frequency variation. Operating values of $\mu_r = 1 - 5$ can be achieved with moderately low-loss performance.

The coupling coefficient κ and most other metamaterial properties are a function of the circuit geometry shown in Figure 5.2.

$$\kappa^2 = \frac{l_x l_z}{\Delta x \Delta z} < 1 \quad (3.11)$$

$$Q = \frac{2l_x l_z w}{\Delta y (l_x + l_z) \delta} \quad (3.12)$$

The resonator 'Q' in (3.12) is a function of the conductor conductivity σ . Care should be taken to observe the condition that conductor thickness $\tau > 2\delta$, where $\delta = \sqrt{\frac{2}{\omega \mu_0 \sigma}}$ is the metallization skin depth at the frequency of operation.

Permittivity

Consider an X-directed electric field. Along the majority of the X-dimension, the electric field is shorted by the metallization of embedded circuit loop parallel to the incident E-field. In the gap-region between the unit-cells, the Z-directed metallizations form inter-cell capacitors for the incident X-directed Electric field. This capacitance is what stores electrical energy and provides for the X-directed permittivity of (3.13). The same phenomenon is observed in the Z-Dimension, but electric field components oriented along the Y-dimension will experience the permittivity of the host dielectric only and $\epsilon_r = \epsilon_{r\,diel}$. The corresponding permittivity tensor is given by (3.14).

$$\epsilon_{eff} = \epsilon_{diel} \left[1 + \frac{\Delta z l_x}{\Delta x \Delta y} \frac{K(\sqrt{1-g^2})}{K(g)} \right] \quad (3.13)$$

$$\bar{\bar{\epsilon}} = \begin{bmatrix} \epsilon_{eff} & 0 & 0 \\ 0 & \epsilon_{diel} & 0 \\ 0 & 0 & \epsilon_{eff} \end{bmatrix} \quad (3.14)$$

Unlike the permeability, the effective permittivity of the medium is not frequency dependent in the microwave region. The permittivity in (3.13) is a function of the inter-cell capacitance which is calculated by means of the same elliptical integral that was used to find the spiral capacitance (Equation 3.6). It should be noted that this simplification ignores the effects of metallization thickness and inter-cell capacitance

due to the inner loops of the spirals. As such will underestimate the true capacitance, and hence underestimate ϵ_{eff} . Here again we seek physical intuition rather than computational precision.

This analysis assumes a medium where the circuits are embedded in a 'simple' dielectric with $\mu_r = 1$.

As this analysis has indicated, the metamaterial substrate will exhibit a highly anisotropic behavior. Permeability enhancement will be achieved for Y-directed magnetic fields only. Permittivity enhancement will occur only for X or Z directed electric fields. This combination of orientation dependent permeability and permittivity is exactly the orientations needed to support the modes of a microstrip patch antenna.

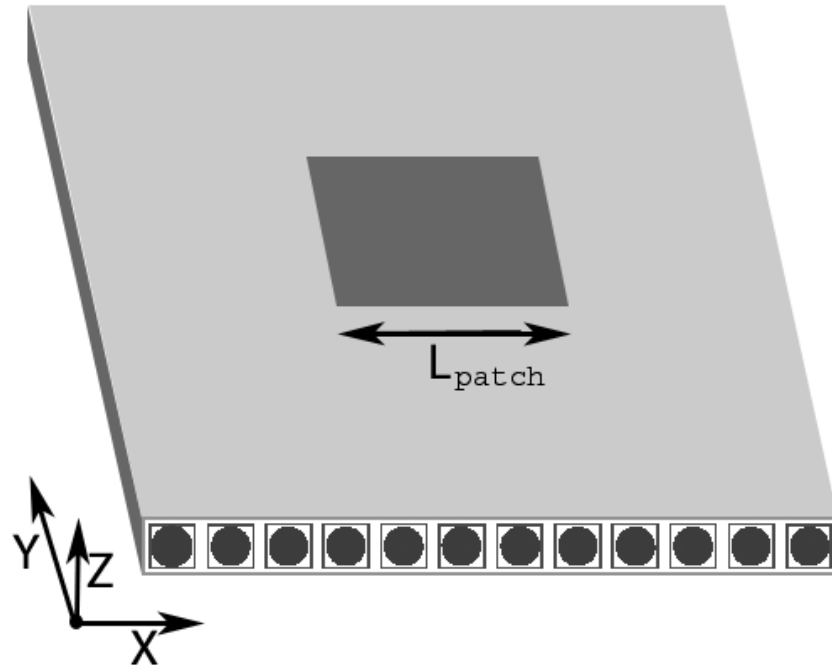


Figure 3.16: Patch antenna over Magnetic Metamaterial Substrate. Length ' L_{patch} ' is the resonant length and indicates orientation of radiating current.

Figure 3.16 demonstrates the proper orientation for a patch antenna operating in the regular mode to experience both μ_{eff} and ϵ_{eff} . In the area under the patch, the image reflections from the metallic antenna and ground plane appear to form an infinite medium in the Z-dimension, allowing the effective medium analysis above to

approximately apply despite the finite geometries.

3.4 Chapter Conclusions

The embedded circuit spiral resonator metamaterial was introduced in this chapter. This new metamaterial will be applied to various uses in the following chapters, both for its positive enhanced permeability below its self resonant frequency and for its negative permeability band-gap region above its self resonant frequency. The embedded circuit spiral resonator provides superior performance to the split ring resonator due to its superior use of the unit cell cross-sectional area.

CHAPTER 4

Material Characterization

"When you can measure what you are speaking about, and express it in numbers, you know something about it; but when you cannot measure it, when you cannot express it in numbers, your knowledge is of a meager and unsatisfactory kind: it may be the beginning of knowledge, but you have scarcely, in your thoughts, advanced to the state of science."

Lord Kelvin

4.1 Chapter Introduction

An inspection of Maxwells equations and the associated constitutive relations reveals that full electromagnetic characterization of simple materials entails identifying five material parameters of electromagnetic significance, ϵ' and ϵ'' which together constitute the complex permittivity of the material, μ' and μ'' which constitute the complex permeability of the material, and σ which is the electrical conductivity of the material. For relatively low conductivity materials at high frequencies σ , which manifests itself as a loss due to electric field, is usually treated to be zero and any electric field induced losses are attributed to ϵ'' .

Therefore the electromagnetic characterization of a relatively non-conductive material requires the determination of four parameters, ϵ' , ϵ'' , μ' and μ'' .

4.2 Waveguide Characterization Toolkit

Both ϵ' and μ' can be determined with acceptable accuracy by the transmission line method, also called the transmission/reflection technique. This technique is based upon transmission line theory and for microwave frequencies, waveguides are usually used to perform measurements.

For the advancement of this research project, an automated material characterization computer toolkit was developed which implements the waveguide transmission line material characterization technique.

To implement the Transmission/Reflection technique a sample block of material with cross-sectional dimensions equal to those of the waveguide interior dimensions is located as shown in figure 4.1. The complex reflection (Γ) and transmission (τ) coefficients will be measured at the frequencies of interest using a vector network analyzer.

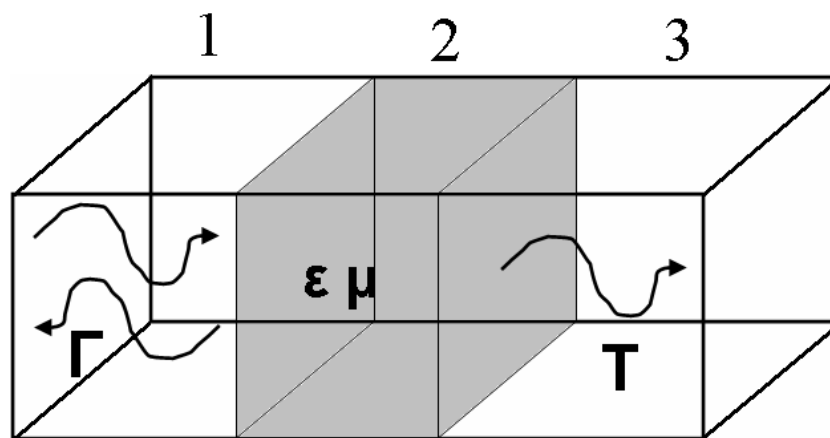


Figure 4.1: Sample under test in waveguide.

While the cross-sectional dimensions of the material should match the internal dimensions of the waveguide, there is freedom in the choice of sample thickness (t). Several factors influence the optimal choice of sample thickness. To avoid phase ambiguity, the sample block should be relatively thin (less than one wavelength in

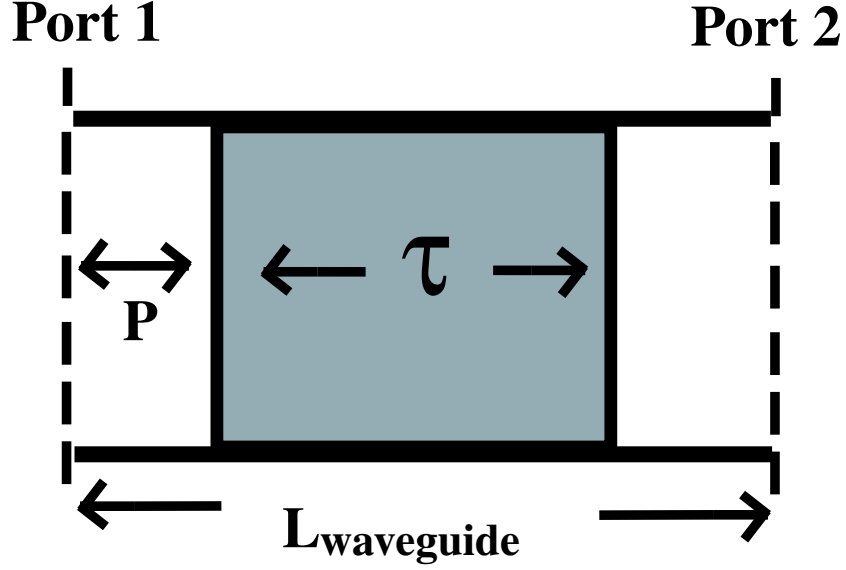


Figure 4.2: Sample position and thickness are variables in the material characterization equations.

material). For higher accuracy in measuring electric and magnetic loss-tangents a long sample would be preferred as this would maximize the physical loss realized, making it easier to measure. If the Nicholson-Ross technique [31] is employed unmodified, integer multiples of $1/2$ wavelength thickness must be avoided [32]. At the cost of increased complexity this limitation can be alleviated by methods such as the iterative Baker-Jarvis method [32] or the other non-iterative methods [[33], [34]].

Analytical Method

When a normalized wave is incident at the region 1:2 boundary in Figure 4.1, the electrical scalar potential F_z may be assigned in all three waveguide regions as

$$F_{z1} = \cos\left(\frac{\pi x}{a}\right) [e^{-jK_z z} + C_1 e^{jK_z z}] \quad (4.1)$$

$$F_{z2} = \cos\left(\frac{\pi x}{a}\right) [C_2 e^{-jK_{z2} z} + C_3 e^{jK_{z2} z}] \quad (4.2)$$

$$F_{z3} = \cos\left(\frac{\pi x}{a}\right) [C_4 e^{-jK_z z}] \quad (4.3)$$

Where the propagation constants are given by

$$K_{z1,3} = \frac{\pi}{\lambda_0 a} \sqrt{4a^2 - \lambda_0^2}, \text{ and}$$

$$K_{z2} = \frac{\pi}{\lambda_0 a} \sqrt{4\epsilon_{r2}\mu_{r2}a^2 - \lambda_0^2}.$$

The transmission coefficient T is equivalent to the S_{21} scattering parameter measured by the vector network analyzer and is equal to coefficient C_4 in (4.3). Similarly the reflection coefficient Γ corresponds to the measured S_{11} and is C_1 in (4.1).

By applying the tangential boundary conditions for the electric and magnetic fields at the region 1:2 and 2:3 boundaries, mode-matching may be used to determine coefficients C_1 - C_4 and ultimately the scattering parameters predicted through a waveguide with a material of the given properties.

The electric field boundary conditions are

$$Ey_1 = Ey_2 \text{ At material medium 1:2 interface,}$$

$$Ey_2 = Ey_3 \text{ At material medium 2:3 interface.}$$

The magnetic field boundary conditions are

$$Hx_1 = Hx_2 \text{ At material medium 1:2 interface,}$$

$$Hx_2 = Hx_3 \text{ At material medium 2:3 interface}$$

The electric field may then be solved from the electric scalar potential (F_z) as,

$$Ex = -\frac{1}{\epsilon} \frac{dF_z}{dy}, \quad Ey = \frac{1}{\epsilon} \frac{dF_z}{dy}, \quad Ez = 0$$

The magnetic field may then be solved from the electric scalar potential (Fz) as,

$$H_x = -j \frac{1}{\omega \mu \epsilon} \frac{d^2 F_z}{dx dz}$$

$$H_y = -j \frac{1}{\omega \mu \epsilon} \frac{d^2 F_z}{dy dz}$$

$$H_z = -j \frac{1}{\omega \mu \epsilon} \left\{ \frac{d^2}{dz^2} + \beta^2 \right\}$$

By applying these boundary conditions to the electric and magnetic fields we obtain the 1:2 interface (at z=0)

$$-\frac{1}{\epsilon_0} \frac{\pi}{a} \sin\left(\frac{\pi x}{a}\right) [e^{-jk_z z} + C_1 e^{jK_z z}] = -\frac{1}{\epsilon_0 \epsilon_r} \frac{\pi}{a} \sin\left(\frac{\pi x}{a}\right) [C_2 e^{-jk_z z} + C_3 e^{jK_z z}] \quad (4.4)$$

and at the 2:3 interface (z=-τ)

$$-\frac{1}{\epsilon_0 \epsilon_r} \frac{\pi}{a} \sin\left(\frac{\pi x}{a}\right) [C_2 e^{-jk_z z} + C_3 e^{jK_z z}] = -\frac{1}{\epsilon_0} \frac{\pi}{a} \sin\left(\frac{\pi x}{a}\right) [C_4 e^{-jk_z z}] \quad (4.5)$$

And similarly for the magnetic fields at the front and back material boundaries. Solving these equations yields four linear equations relating coefficients C1-C4.

$$[1 + C_1] = \frac{1}{\epsilon_r} [C_2 + C_3] \quad (4.6)$$

$$\frac{1}{\epsilon_r} [C_2 e^{-jK_z(-\tau)} + C_3 e^{jK_z(-\tau)}] = [C_4 e^{-jK_z(-\tau)}] \quad (4.7)$$

$$\frac{K_z}{K_z^2} [1 - C_1] = \frac{1}{\mu_r \epsilon_r} [C_2 - C_3] \quad (4.8)$$

$$\frac{K_{z2}}{K_z} \frac{1}{\mu_r \epsilon_r} [C_2 e^{jK_z \tau} - C_3 e^{-jK_z \tau}] = C_4 e^{jK_z \tau} \quad (4.9)$$

These equations are solved for the coefficients, noting that $C_1=S_{11}$ and $C_4=S_{21}$, then the resulting 'scattering parameters' are

$$S_{11} = \frac{-j[(\frac{K_{z2}}{K_z})^2 - \mu_{r2}^2] \sin(K_{z2}\tau)}{2\mu_{r2}^2 \cos(K_{z2}\tau) + j[(\frac{K_{z2}}{K_z})^2 + \mu_{r2}^2] \sin(K_{z2}\tau)} \quad (4.10)$$

$$S_{21} = \frac{2}{j[\frac{K_{z2}}{K_z} + \frac{K_z \mu_{r2}}{K_{z2}}] e^{jK_z \tau} \sin(K_{z2}\tau) - 2e^{jK_z \tau} \cos(K_{z2}\tau)} \quad (4.11)$$

These scattering parameters will only correspond to measured scattering parameters if the vector network analyzer calibration is performed up to the exact front and back of the sample ($P = 0, L_{waveguide} = t$ in Figure 4.2). Since this is often not physically realizable, methods have been developed to correct for an unknown sample position in a waveguide, again at the cost of increased complexity ([32]). It is possible to measure the length of your waveguide and the length of your sample, then to control the position of the sample with reasonable precision by placing the sample flush with the front end of the waveguide ($P=0$). In this case, a phase-shift $e^{-jK_z(L_{waveguide}-\tau)}$ applied to S_{21} (Eq 5) may be used to account for the excess waveguide length.

In order to determine the complex permittivity $\dot{\epsilon} = \epsilon' + j\epsilon''$ and complex permeability $\dot{\mu} = \mu' + j\mu''$ at a specific frequency by our iterative solver implementation, an initial guess of material parameters is used and the scattering parameters from (4.10) and (4.11) are calculated analytically. The solution is compared with the measured values of S_{21} and S_{11} and the difference between the scattering parameters predicted by the guessed material properties and the measured scattering parameters represents the error function for numerical solution. Numerical methods are employed to vary the initial guess of material parameters in order to minimize the error function and find the permittivity and permeability which lead to the the measured transmission

and reflection coefficients.

Generally, when this measurement technique is employed for a large number of single frequency measurements which are taken across a frequency bandwidth. In this case the solution determined from a specific frequency serves as an excellent 'initial guess' of the value at an adjacent frequency.

4.2.1 Effectiveness of the waveguide characterization toolkit

In order to validate the effectiveness of the waveguide characterization toolkit, a series of material measurements were made and compared to measurements taken by the commercially available coaxial probe method [35].

It is known a priori that for Teflon $2.0 \leq \epsilon'_r \leq 2.5$ and $\mu'_r = 1.0$. The material loss factors are also known, where $\epsilon''_r \leq 1 \times 10^{-3}$ and $\mu''_r = 0.0$. The teflon sample was measured by a commercially available dielectric probe technique as reference, then measured with the waveguide characterization toolkit. The results are given in table 4.1, where the magnetic properties are not measured by the coaxial probe method but instead the material is assumed to be non-magnetic.

Table 4.1: Teflon Measurement

Teflon Sample	Coaxial Probe method	Waveguide Toolkit
ϵ'	2.31	2.2549
ϵ''	0.15	0.006
μ'	1.0*	0.9894
μ''	0.0*	0.006

The measurement sensitivity for a non-magnetic ($\mu_r = 1 + j0$) low-loss dielectric similar to teflon ($\epsilon_r = 2.25 - j5 \times 10^{-4}$) was tested by causing a 0.05% perturbation in the measured S11 and S21. The result was a 0.07% error induced in the measurement of ϵ'_r and μ'_r but an error of almost 5000% in ϵ''_r and μ''_r .

As Table 4.1 and Figure 4.3 indicate, the waveguide toolkit provides excellent

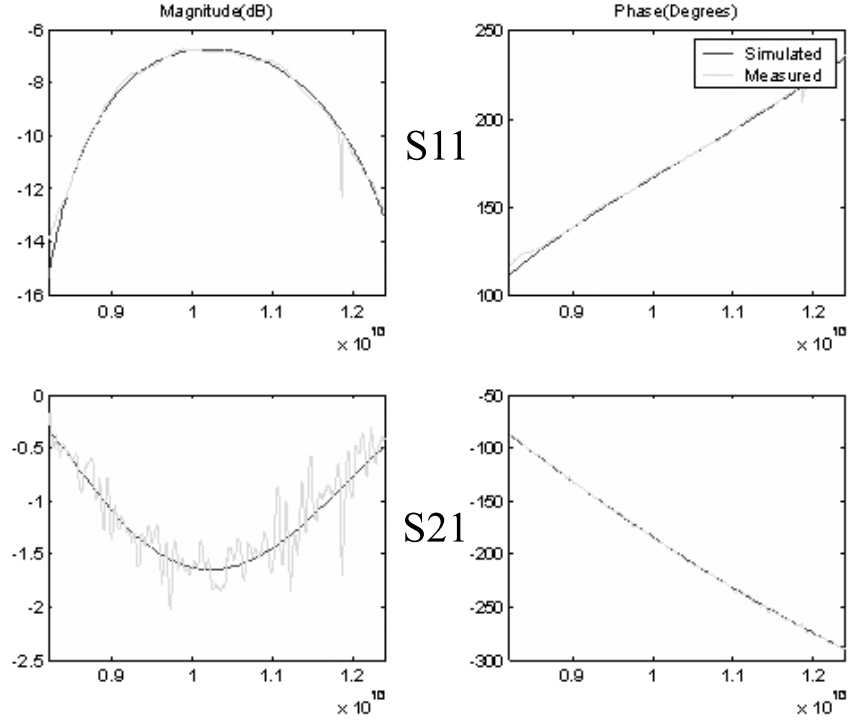


Figure 4.3: Comparison of predicted and measured scattering parameters for sample material (Teflon). The good match indicates that the material characterization properties determined by the waveguide toolkit are accurate.

accuracy in characterizing ϵ' and μ' (1% error), but is not very good at characterizing the loss factors ϵ'' and μ'' of a low loss material (error $\geq 1000\%$).

4.3 Resonant Cavity Method

The traditional resonant cavity method may be employed to fully characterize a dielectric or a magnetic sample, but not a material exhibiting both properties. Analytic techniques exist for determining either $\epsilon_r = \epsilon'_r + j\mu''_r$ or $\mu_r = \mu'_r + j\mu''_r$ if the other is $1+j0$. In the discussion that follows a short cylindrical metallic cavity will be assumed, although many differing geometries are possible.

The analytic method employs a perturbation theory for determining the complex permittivity of a non-magnetic material. In this method a sample is placed at the center of a cavity where the electric field is at a maximum. By observing the shift in

resonant frequency when the sample is present, the real permittivity ϵ' of the sample may be determined. Once the real portion of the permittivity is determined, the shift in cavity Q-factor is used to determine the samples imaginary permittivity ϵ'' and electric loss tangent ($\tan \delta_e \approx \frac{\epsilon''}{\epsilon'}$).

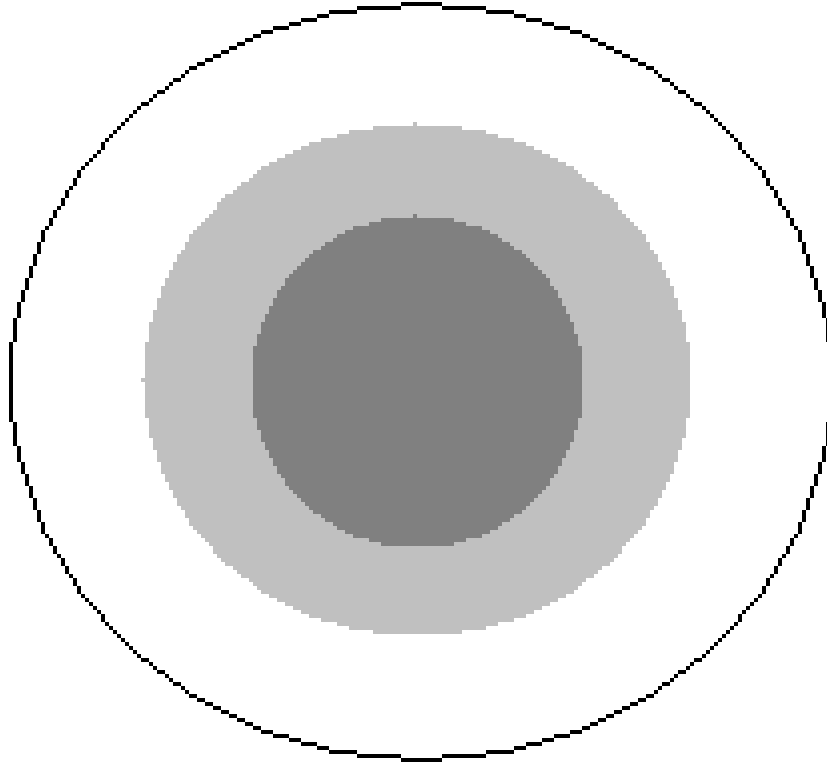


Figure 4.4: The electric field distribution in a short cavity (TM010 Dominant mode). The maximum electric field magnitude is at the cavity center.

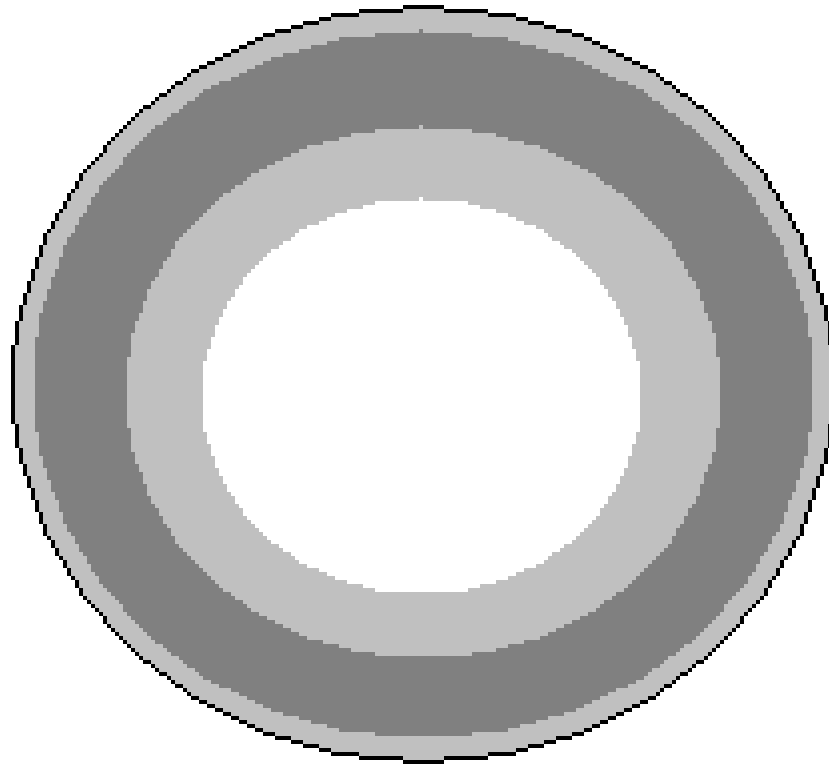


Figure 4.5: The magnetic field distribution in a short cavity (TM010 Dominant mode). The maximum magnetic field magnitude is near the cavity edge.

The advantage of using the cavity method to characterize low-loss materials is that the strong electric and magnetic fields contained in the cavity result in measurable phenomenon (resonant frequency shift and Q-factor shift) which are very strongly influenced by small differences in the complex permittivity of the sample.

For a small vertically oriented dielectric cylindrical ($\mu_r=1$) at the cavity center, equation (4.12) is the classic perturbation method equation used to determine the dielectric constant of the non-magnetic sample [36].

$$\epsilon_r - 1 = \frac{1}{PC} \frac{V_{Cavity}}{V_{pert}} \frac{Fr_{pert} - Fr_{empty}}{Fr_{empty}} \quad (4.12)$$

For a small non-dielectric ($\epsilon_r=1$) sample at the cavity edge, equation 4.13 is the classic perturbation method equation used to determine the relative permeability of the magnetic sample [36].

$$\mu_r - 1 = \frac{1}{PC} \frac{V_{Cavity}}{V_{pert}} \frac{Fr_{pert} - Fr_{empty}}{Fr_{empty}} \quad (4.13)$$

To determine the material loss factor ($Q_{material} = \frac{\epsilon'_r}{\epsilon''_r}$ or $\frac{\mu'_r}{\mu''_r}$), one uses equation (4.14).

$$Q_{pert} = \frac{\epsilon_r \text{ OR } \mu_r}{-\frac{1}{PC} \frac{V_{cavity}}{2V_{pert}} \left(\frac{1}{Q_{Perturbed\ Cavity}} - \frac{1}{Q_{Empty\ Cavity}} \right)} \quad (4.14)$$

Unfortunately, several shortcomings of this analytical method prevent it from being adequate for our purposes. The analytical method limits the material under test to causing a mere perturbation of the cavity fields, and this limits the sample to a small size with low dielectric constant and loss. More importantly this method only measures 2 values, resonant frequency shift and Q-factor and can not be used to solve for the 4 unknowns ϵ' , ϵ'' , μ' , and μ'' in practical magnetic materials.

4.3.1 Frequency Extended Perturbation Technique

The traditional resonant cavity perturbation technique is extremely popular for the highly precise and accurate measurement of complex permittivity or permeability of small samples. Although this technique is primarily used for the characterization of non-magnetic materials, analytical solutions do exist for using this technique on theoretical non-dielectric magnetic materials ($\epsilon_r = 1, \mu_r \neq 1$)[36].

The great merit of the classic material perturbation technique is the extremely high precision with which material characterization measurements are possible. The great shortcoming of this technique is that by its nature, this resonant technique only measures the properties of the sample under test at a single frequency.

The Frequency Extended Perturbation Technique is a procedure for performing resonant cavity based material characterization measurements over a bandwidth, rather than at only a single frequency. The merit of this technique is that when performing high precision measurements at a single frequency, all the data necessary to characterize over a wider bandwidth is already collected, with negligible additional computational effort required. Therefore, once implemented the Frequency Extended Perturbation Technique may be considered a 'freebie' when the expensive perturbation technique is employed.

Since a highly precise measurement has been obtained at a single frequency by the classical perturbation technique, the benefit of using the Frequency Extended Perturbation Technique lies in observing the trend of the material properties at frequencies diverging from that single frequency. Therefore, one useful application of this of the frequency extended perturbation method is in the measurement of dispersive materials.

Equation (4.15) is a frequency transformation which is employable to predict the full spectral response of a dielectric (or magnetic) perturbed cavity. The inversion of this predictive technique may be used to determine the permittivity (4.16) or

permeability (4.17) across the whole frequency spectrum around resonance, and not only at the resonant frequency of interest.

$$S_{21}(f) = -\frac{2\sqrt{\kappa_1\kappa_2}}{1 + \kappa_1 + \kappa_2} \frac{1}{1 + 2jQ_L \frac{f-f_0}{f_0}} \quad (4.15)$$

By solving for the material properties of perturbed cavity, the material permittivity and permeability may be calculated.

$$\epsilon_r - 1 = \frac{1}{PC} \frac{V_{Cavity}}{V_{pert}} \frac{F_{pert} - F_{empty}}{F_{empty}} \quad (4.16)$$

$$\mu_r - 1 = \frac{1}{PC} \frac{V_{Cavity}}{V_{pert}} \frac{F_{pert} - F_{empty}}{F_{empty}} \quad (4.17)$$

Several equations may be employed to increase the accuracy of this technique. Equation 4.18 and 4.19 account for the loading effect due to the cavity ports. In cavities where the loading is strong ($S_{21} \geq -10\text{dB}$), this loading must be accounted for.

$$2\kappa = \frac{|S_{21_{empty}}|}{1 - |S_{21_{empty}}|} \quad (4.18)$$

$$Q_L = \frac{Q_0}{1 + \kappa_1 + \kappa_2} \quad (4.19)$$

Validation of the Frequency Extended Perturbation Method

In figure 4.6, the system response of an empty cavity is compared to the response when the cavity is loaded by a small Teflon dielectric sample.

When equation 4.16 of the frequency extended perturbation method is employed to determine the Teflon permittivity, the results are shown in figure 4.7. There is good agreement with what would be predicted for a non-dispersive material such as

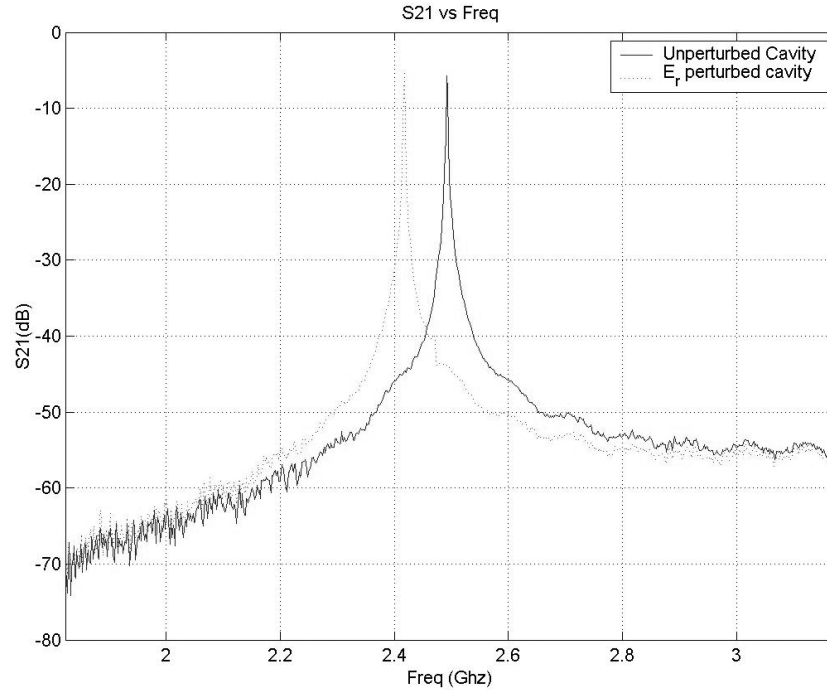


Figure 4.6: Cavity response (S_{21}) of a resonant cavity when empty and when perturbed by a dielectric (teflon) sample.

Teflon, exhibiting $\pm 10\%$ accuracy over a 15% bandwidth.

To further test the abilities of the frequency extended perturbation method, a dispersive metamaterial was measured. The Embedded Circuit Resonator Metamaterial is described in detail in chapter 3, and for our purposes here all that matters is the theoretical dispersive permeability predicted for such a material, which is shown in figure 4.8.

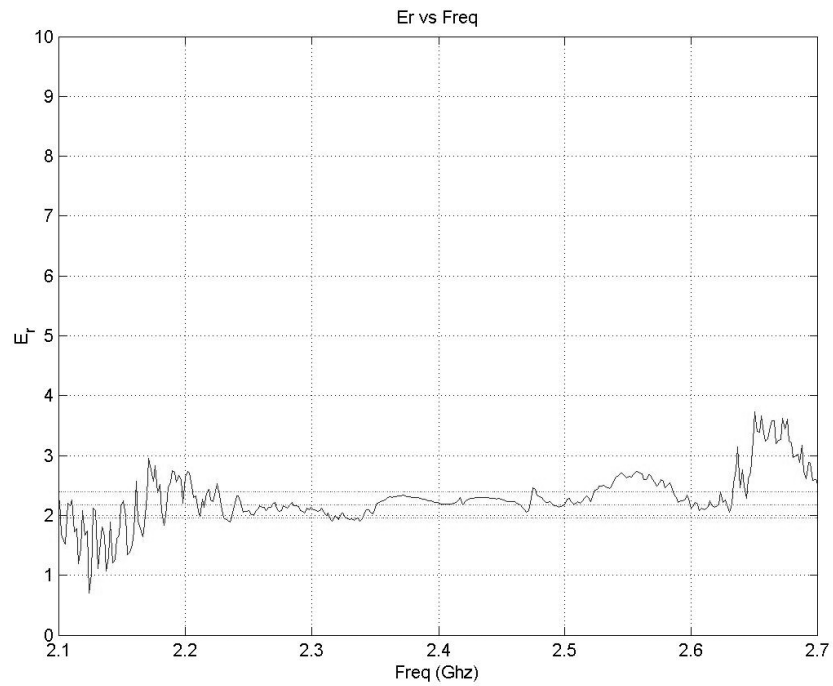


Figure 4.7: Dielectric constant of Teflon, measured by the frequency extended perturbation method.

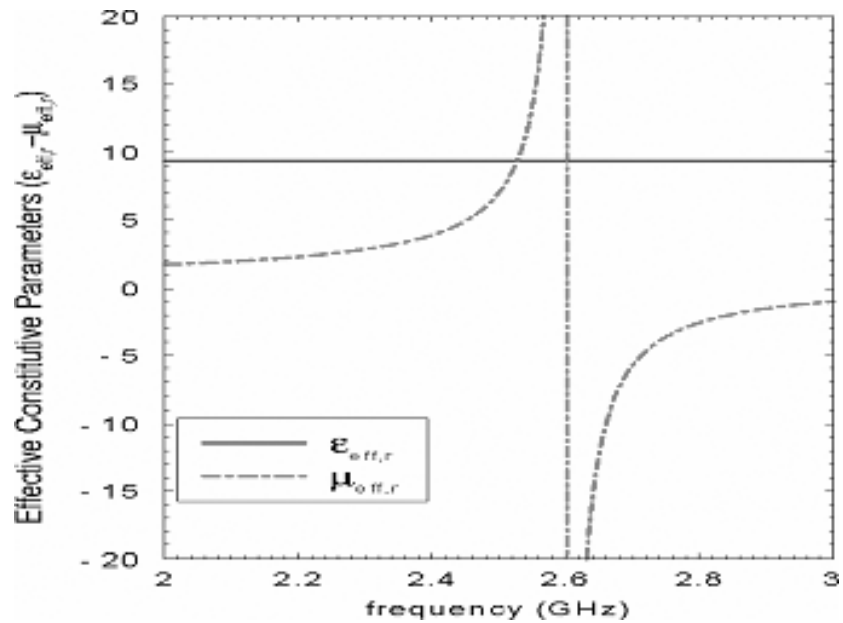


Figure 4.8: The permittivity and permeability of an embedded circuit resonator predicted by the models developed in this thesis.

Figure 4.9 validates that the FEPM properly predicts the spectral response due to a dispersive medium. The HFSS simulations performed here to produce the validation points in figure 4.9 were also used to validate (4.17).

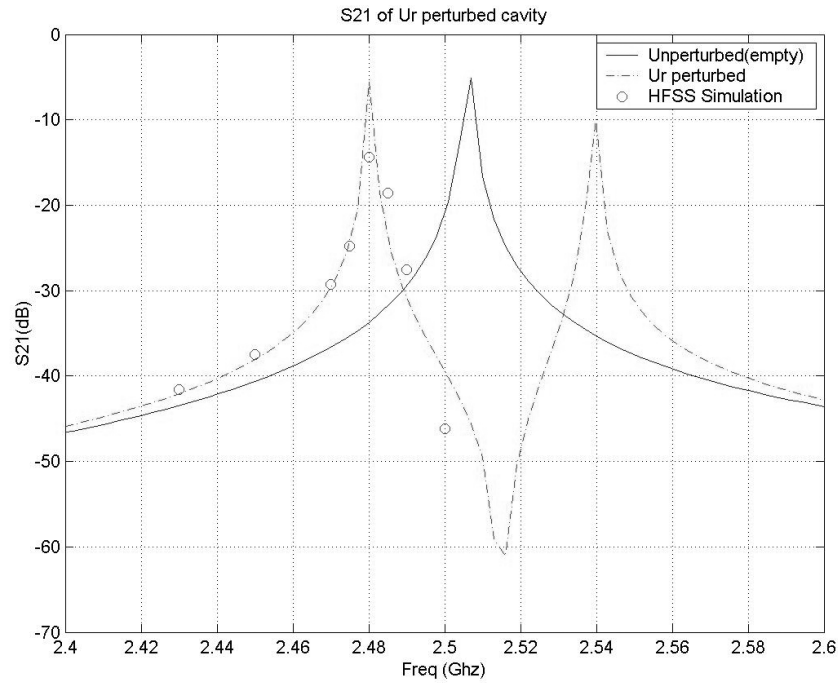


Figure 4.9: The system response of an empty cavity is compared to the perturbed response due to an embedded-circuit metamaterial resonator sample predicted by 4.15. The prediction is validated by HFSS simulations.

As a final validation test of the the FEPM technique, an embedded circuit resonator metamaterial was physically fabricated and measured. Figure 4.11 shows a picture of the material, and Figure 4.12 shows that the frequency extended perturbation method does an excellent job of measuring the spectral trend of this permeability dispersive material.

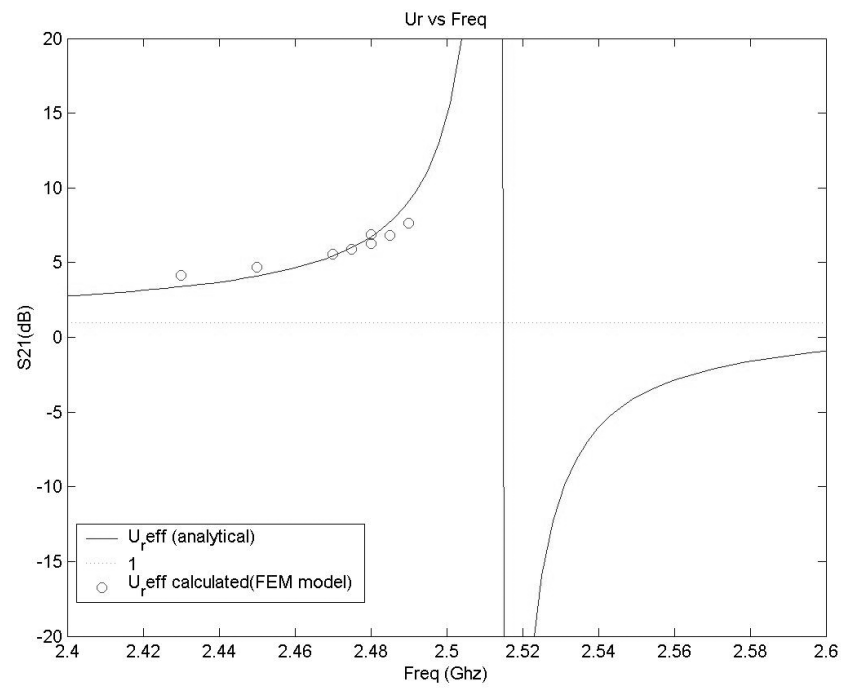


Figure 4.10: The permeability determined by 4.17 from the HFSS simulations is compared to the permeabilities used for those simulations.

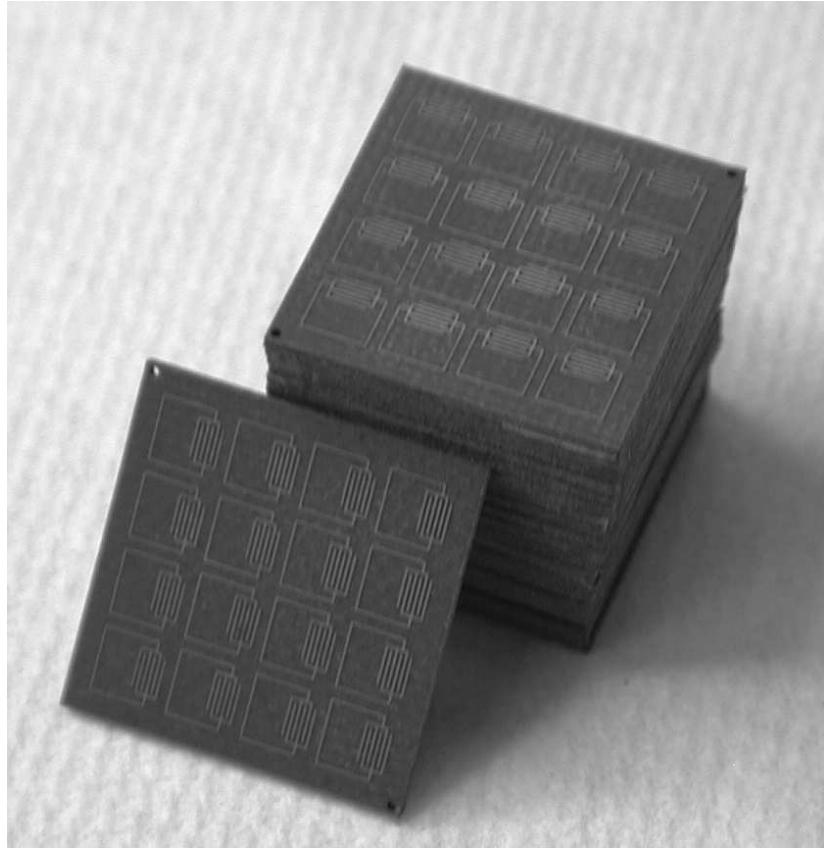


Figure 4.11: Embedded Circuit Resonator Metamaterial.

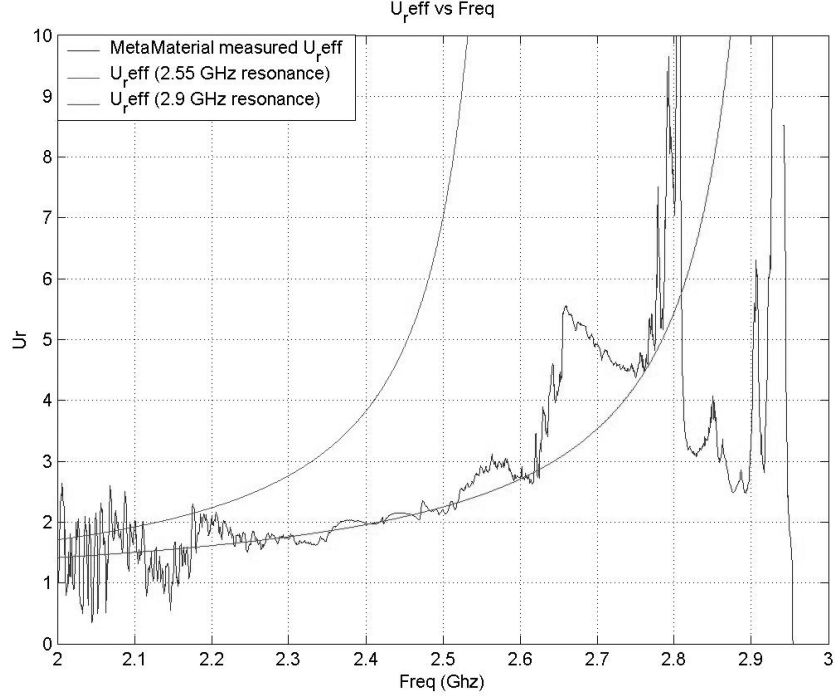


Figure 4.12: The dispersive metamaterial permeability measured by the FEPM is compared to that predicted by the metamaterial model.

4.3.2 Hybrid Perturbation Technique

Measurement of a materials electric and magnetic properties is the critical step between predicted theory and validated reality of engineered electromagnetic materials. To fully characterize a materials electromagnetic properties both its complex permittivity ($\hat{\epsilon} = \epsilon' - j\epsilon''$) and complex permeability ($\hat{\mu} = \mu' - j\mu''$) must be determined. Characterization of a non-magnetic material requires identifying both its dielectric constant (ϵ') and electric loss tangent ($\tan \delta_e \approx \frac{\epsilon'}{\epsilon''}$). This is a well researched area and excellent methods exist to characterize non-magnetic materials [[37],[38]]. For magnetic materials methods have been developed to accurately measure both the real electric permittivity ϵ' and real magnetic permeability μ' [[39],[40]]. Unfortunately these methods do not characterize the imaginary permittivity ϵ'' or magnetic permeability μ'' with high accuracy. Consequently the electric loss tangent ($\tan \delta_e \approx \frac{\epsilon'}{\epsilon''}$)

and magnetic loss tangent ($\tan \delta_m \approx \frac{\mu'}{\mu''}$) of low-loss materials can not be reliably determined. The hybrid method proposed here accurately measures all portions of complex permittivity and permeability of low-loss materials, including their electric and magnetic loss tangents.

This hybrid method was developed for the measurement of low-loss materials exhibiting isotropic permittivity and permeable properties as are present in low loss uniform composites or some Meta-Materials but this technique may be extended for more general anisotropic application. In the general linear case, anisotropies may exist in both ϵ and μ . When this is the case, complex permittivity and permeability tensors $[\hat{\epsilon}]$ and $[\hat{\mu}]$ fully characterize these materials and a variation of the hybrid measurement method given here may be employed. Permittivity and permeability tensors may occur in engineered materials due to either structural factors such as periodicity or as a result of an external field such as the effect of magnetic biasing on permeability for many magnetic materials.

The Hybrid Method

In linear isotropic materials with both complex permittivity $\hat{\epsilon}$ and permeability $\hat{\mu}$, four unknown factors need to be determined ($\epsilon', \epsilon'', \mu', \mu''$) to fully characterize the materials small-signal EM properties. To determine these four unknowns, four independent measurements are needed. In this hybrid method both computer simulations and experimental measurements are performed and the results are combined to provide a single complete and accurate characterization of the material under test (Fig. 4.13). Independently either of the two techniques employed here (the waveguide technique and the hybrid method) can provide all four measured values and fully characterize the measured material, but by combining these methods a single highly accurate characterization is achieved.

The hybrid method described here employs the transmission line technique as well

as a resonant cavity technique to exploit the relative merits of each in characterizing a low-loss material. The transmission line technique is recommended to determine the real permittivity ϵ' and real permeability μ' over a frequency band of interest. The resonant cavity technique is then used to accurately determine the electric loss tangent ($\tan \delta_e \approx \frac{\epsilon''}{\epsilon'}$) and magnetic loss tangent ($\tan \delta_m \approx \frac{\mu''}{\mu'}$) at a single frequency within this band.

In the transmission-line method, described earlier in the section 'Waveguide Toolkit', a modern vector network analyzer measures the complex reflection and transmission coefficients Γ and τ . The four measured values $|\Gamma|, \angle\Gamma, |T|$, and $\angle T$ are used to determine the four material properties $\epsilon', \epsilon'', \mu'$, and μ'' at each measured frequency. This transmission line method determines the real portions of permittivity ϵ' and permeability μ' accurately, but the loss factors ϵ'' and μ'' are not well characterized for low-loss materials. In the transmission/reflection method, field strengths are relatively low. In the absence of high field magnitudes the effect of loss mechanisms ϵ'' and μ'' are minor and the calculated values for these loss mechanisms are prone to measurement error.

In contrast with the high error sensitivity of the transmission-line method, the resonant-cavity based hybrid measurement technique measures loss tangents highly accurately. By confining strong electromagnetic fields within a resonant chamber, material losses are increased to levels where the electric and magnetic loss factors can be measured accurately. A major drawback of this method is that it characterizes the material at only a single frequency.

The second major drawback of the traditional cavity technique, is that it is unclear how to account for materials exhibiting both magnetic and electric properties. In order to characterize both the electric and magnetic loss tangents independently, a new method of taking independent measurements in resonant cavities was developed and is presented here, the hybrid method. The hybrid method can be used in

determining the real portions of permittivity ϵ' and permeability μ' , but unlike the transmission line method it measures at only a single frequency.

To realize the benefit of high accuracy in material characterization for our application the resonant cavity method must be able to make four independent measurements. This is achieved by subjecting the sample to two independent sets of electric-to-magnetic field ratios.

At the center of the cavity, the electric field is at a maximum, and the magnetic field is at a minimum (Figure 4.4). The resonant frequency shift with the sample at the cavity center is predominantly caused by the dielectric constant of the material, and the shift in Q-factor is predominantly caused by the materials electric loss tangent. In contrast, near the edge of the cavity the electric field is at a minimum and the magnetic field is at a maximum (Fig. 4.5). The resonant frequency shift with the sample near the edge will be much more strongly influenced by the real permeability of the material than at the center, and the shift in Q-factor will be more strongly influenced by the materials magnetic loss tangent. In this manner, by taking measurements of resonant frequency shift and Q-factor shift with the sample in two independent positions, four independent measurements will be obtained and all four material unknowns ϵ' , ϵ'' , μ' , and μ'' can be determined.

Numerical simulation is required for this stage of the hybrid method since no analytical method currently exists. One benefit of using simulation methods is that measurements can be made of materials of any geometry. That is, measurements are not limited to symmetric or predefined shapes as is required to determine the polarization factor (P) in the classic cavity perturbation method. In order to perform this measurement, the cavity and sample are modeled and then the system is simulated for various possible values of permittivity and permeability. By matching the simulation results to measured behavior which most nearly approximates it, the complex permittivity and permeability can be determined.

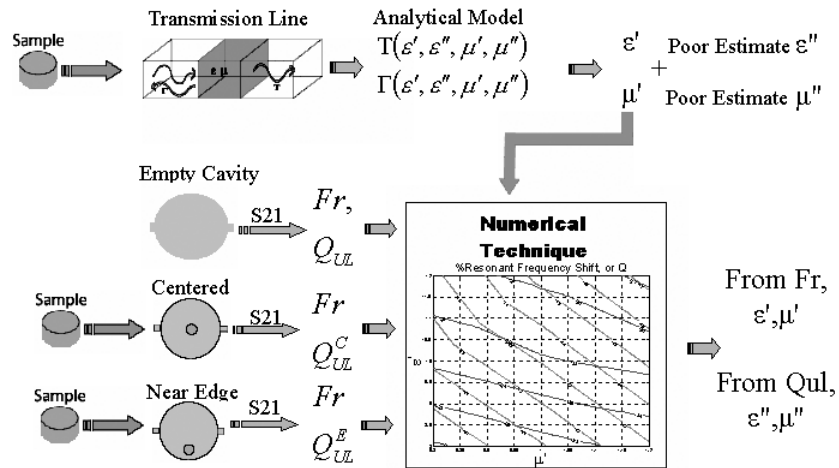


Figure 4.13: Flowchart showing the steps of the hybrid characterization method.

The Magnitude of Real Permittivity and Permeability

When attempting to determine the real permittivity and permeability, ϵ' and μ' respectively, of a sample the material is first simulated as lossless. This approximation is valid because the electric and magnetic loss tangents of a low-loss sample will not affect the samples resonant frequency significantly. With the loss tangents held constant, the simulation values of ϵ' and μ' are swept and the cavity resonant frequency shift is observed.

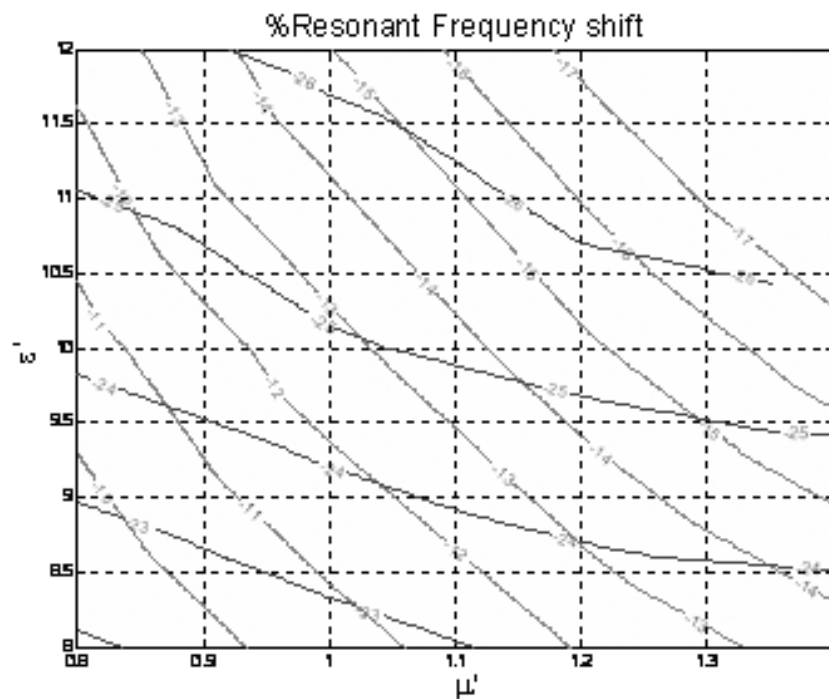


Figure 4.14: Percent shift shift in resonant frequency with sample in a cavity, for various possible material permittivities and permeabilities.

For each position of the sample, cavity center or cavity edge, a set of curves indicating ϵ' , μ' pairs which result in the same resonant frequency shift will be generated (Figure 4.14). For the center case, the sample permeability will have a relatively weak influence on the resonant frequency shift. This is due to the magnetic field at the cavity center being a minimum, whereas the electric field is a maximum, and consequently the electrical properties of the material will dominate. By identifying the resonant frequency shift which corresponds to the frequency shift which is physically measured when the sample is centered, a single curve of the possible ϵ' , μ' pairs is identified, but the specific value of ϵ' , μ' is not yet known.

Simulations with the sample at the edge are performed next. A second set of resonant frequency shift curves are generated and it is observed that the magnetic field exhibits a much stronger influence than in the sample centered case and the curves vary (slope) much more strongly with changing permeability.

By finding the intersection point of the two curves corresponding to the resonant frequency shifts measured in the center and edge conditions, the unique pair of ϵ' , μ' which could result in the two measured values is identified, and the materials real permittivity and real permeability are determined. (Figure 4.14)

The Magnitude of Imaginary Permittivity and Permeability

When ϵ' and μ' are known either from the waveguide method, or by the cavity method as described above, then the imaginary permittivity ϵ'' and imaginary permeability μ'' may be found. ϵ' and μ' are held constant while ϵ'' and μ'' (or the electric and magnetic loss tangents) are varied. Curve-sets similar to those generated to determine ϵ' and μ' are generated, but in this case the curves indicate shifts in Q-factor instead of resonant frequency (Figure ??). Similar observations regarding the effects of sample position on curve slope apply in the Q-factor plots.

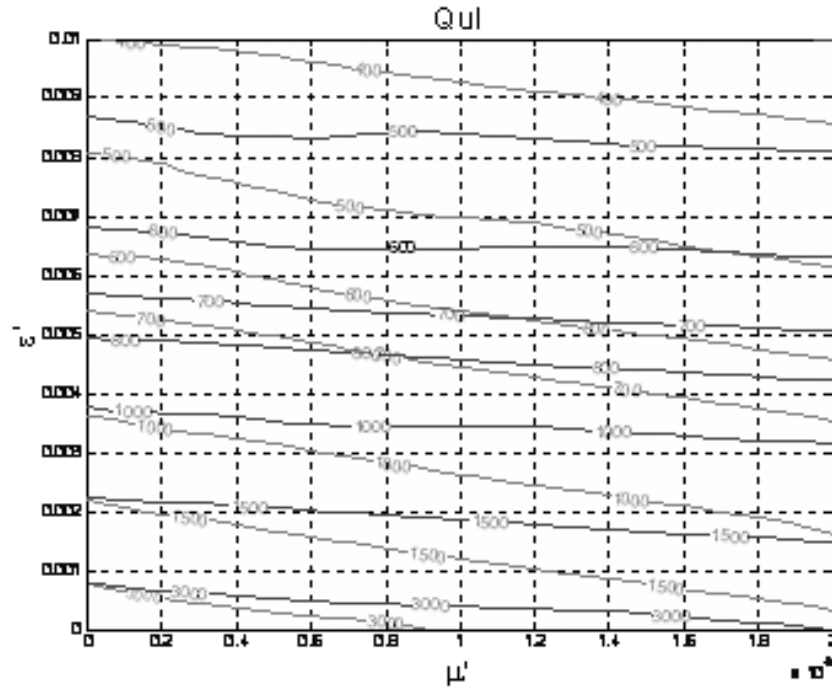


Figure 4.15: Shift shift in Q-factor with sample in a cavity, for various possible material electric and magnetic loss factors.

Improving Measurement Accuracy

The Q-factor of a cavity represents the ratio of energy stored in the cavity fields to the power lost per cycle. In order to measure the losses due to energy dissipated in the material accurately, the other sources for loss must be minimized and any remaining non-idealities accounted for. In an enclosed resonant cavity power may be lost through cavity wall currents, or out the cavity ports. In order to minimize the power dissipated by wall currents, smooth highly conductive cavity walls must be used. The dominant cavity mode for a 'short' cavity less than half as tall as it is wide is the the TM010 mode. In the TM010 mode the induced currents are radial on the cavity top and bottom and axial on the cavity walls (Figure 4.16).

For a cavity with a removable lid, this lid-gap seam causes a disruption in the conductor currents at the lid gap. To minimize the effects of this lid-gap, an RF-Choke flange may be employed, causing a virtual short at the lid/cavity interface

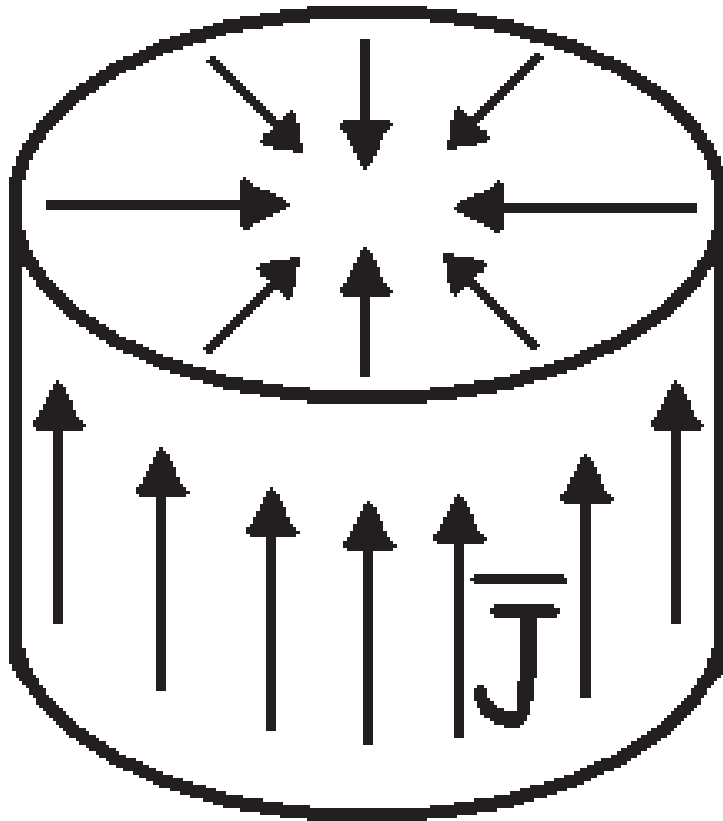


Figure 4.16: Electrical currents on the wall and lid of a cylindrical cavity in TM₀₁₀ mode.

(Fig. 4.17). The use of choke flanges dramatically improves the observed cavity Q , bringing it much closer to the theoretically ideal for a given cavity wall metal [26]. Since imperfections still exist in the modeling of the wall surfaces and lid-gap, the published bulk-conductivity of the wall metal can not be used. Instead an effective conductivity is chosen to match the simulated Q -factor of the measured cavity to the measured Q -factor.

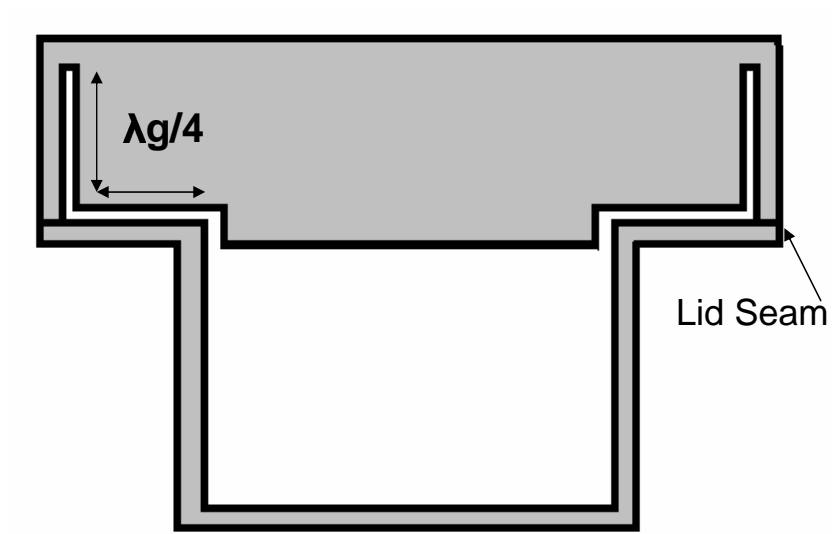


Figure 4.17: Employing a Choke-Flange significantly improves cavity Q-factor, and the accuracy of material loss factor measurement.

The second source for power loss in a resonant cavity is transmission out through the ports. In order to minimize this source of power loss, a cavity with low coupling (voltage coupling coefficient $k < 0.32$, or $S_{21} < -10db$) should be used. In these simulations, port coupling is probably the hardest thing to model accurately, and further elimination of the coupling effects is desirable. To facilitate modelling and analysis, ports should be symmetrical as well as low-coupling. The 'Unloaded' Q-factor may be employed to mathematically factor out the effects of power lost out the ports, providing the 'ideal' Q-factor of the cavity if no ports were present [41].

$$Q_{Unloaded} = \frac{Q_{loaded}}{1 - |S_{21}|} \quad (4.20)$$

With most of the the error sources suppressed but not eliminated it is preferable to compare simulation and measurement by the percentage shift in resonant frequency and unloaded Q-factor rather than absolute values when determining complex permittivity and permeability.

Validation of Hybrid Measurement Method

To validate the Hybrid Measurement Method, a series of measurements were performed. First, the technique was performed on magnetic ($MgFe_2O_4$) and non-magnetic materials (Aluminum-Oxide and ULF) to determine how accurately the real components of permittivity and permeability can be measured (Table 4.2). This series of experiments indicated that such measurements achieve accuracy within approximately 10-30%. Although comparable to the 10-20% achieved by commercially available non-resonant measurement methods, this is not of particularly high accuracy and is useful mostly as a validation of the technique.

To test the measurement accuracy of the Hybrid Measurement Method for measuring the loss-factor of low-loss materials, a low loss material of known loss factor needed to be measured and a low-loss non magnetic material such as Aluminum-

Table 4.2: Measured Permittivity and Permeability of Materials

Material	Relative Permittivity (ϵ_r)	Relative Permeability (μ_r)
Aluminum Oxide	9.997	1.32
ULF	7.42	1.01
$MgFe_2O_4$ +5% BST	7.55	0.372
$MgFe_2O_4$ +10% BST	11.35	0.40

Oxide is an ideal candidate. Since it is non-magnetic, it is known that the magnetic loss factor for such a material is zero. Therefore the value when measured of μ_r'' is itself the error level attributable to the measurement method. Table 4.3 shows that when such a measurement was performed, the error was on the order of 1×10^{-4}

Table 4.3: Measured Loss Factors of Aluminum-Oxide

Material	Electric Loss Factor (ϵ_r'')	Magnetic Loss Factor (μ_r'')
Aluminum Oxide	5×10^{-3}	1×10^{-4}

To determine the error sensitivity, simulations were performed for the measurement of aluminum oxide loss factor. For the purpose of determining the sensitivity the modeling is assumed to be perfect and a 1% error is induced in the measured Q-factor to be analyzed. This causes a 1.4% error in the predicted loss factor ϵ'' . Or considered differently, if the material measurement were performed perfectly and a 1% error existed in the system simulation predicted Q-factor, then a 1.4% error would be observed in the characterization accuracy.

4.4 A comment on Measuring Anisotropic materials

Anisotropies may be present in the material under test for many reasons, such as due to external fields or material structure. Anisotropies in a general 3-dimensional

form for permittivities take the form in Eq. 4.21

$$[\dot{\epsilon}] = \begin{pmatrix} \epsilon_{xx} & \epsilon_{xy} & \epsilon_{xz} \\ \epsilon_{yx} & \epsilon_{yy} & \epsilon_{yz} \\ \epsilon_{zx} & \epsilon_{zy} & \epsilon_{zz} \end{pmatrix} \quad (4.21)$$

or a simpler form such as the 1-dimensional (uniaxial) anisotropic permeability

$$[\dot{\mu}] = \begin{pmatrix} \mu_1 & j\mu_2 & 0 \\ -j\mu_2 & \mu_1 & 0 \\ 0 & 0 & \mu_3 \end{pmatrix} \quad (4.22)$$

Examples of uniaxial anisotropies are 1-D periodic meta-materials (Fig. 4.18) or the permeability under an externally applied static magnetic field (Eq. 4.22). A method of measuring the uniaxial anisotropy induced by an externally applied magnetic field which is somewhat similar to the cavity method portion of our hybrid method exists [40].

When it is desired to solve for both complex permittivity and permeability in a uniaxial case or the more general 3D case, the general form of the anisotropy which leaves the minimum number of unknowns should be chosen. For example, if the anisotropy is one dimensional as in the case shown in Fig. 4.18 the axis normal to the plane is identified as the primary axis, and symmetry will exist in the remaining two axes. The resulting symmetry will simplify both $[\dot{\epsilon}]$ and $[\dot{\mu}]$ from the form of Eq. 4.21 to the simpler uniaxial form in Eq. 4.22. In order to measure the remaining unknowns multiple measurements under different sample orientations need to be made.

In an extremely time-intensive process, simulations could be performed for all measurement conditions and the complete tensors $[\dot{\epsilon}]$ and $[\dot{\mu}]$ could be characterized by the same general process as is used to determine $\epsilon', \epsilon'', \mu',$ and μ'' for isotropic materials.

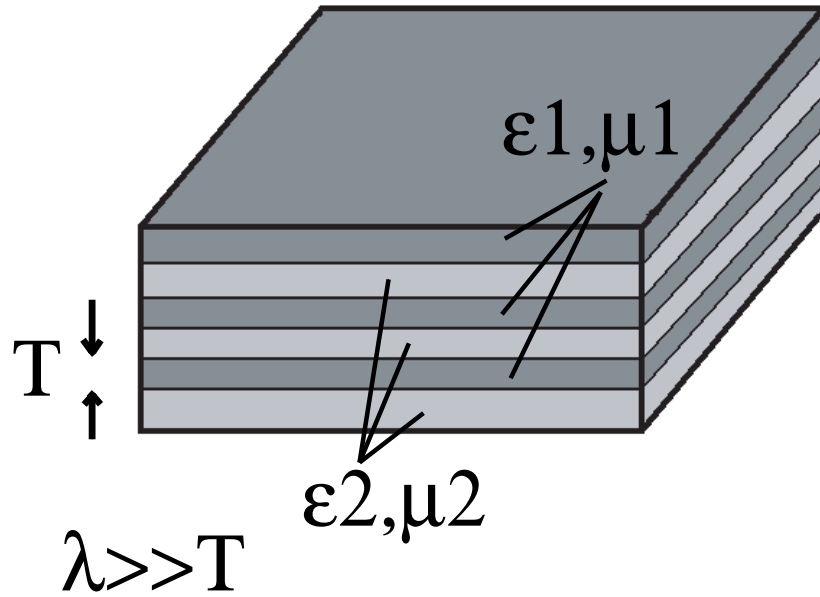


Figure 4.18: Stacked isotropic layers are examples of uniaxial anisotropies.

4.5 Chapter Conclusions

An overview of the basic concepts behind material characterization were presented. The waveguide toolkit is essentially an automated measurement software package implementing a customized version of the academically popular Nicolson-Ross-Weir [NRW] material characterization technique. This technique provides good (approx 10%) accuracy in measuring the real permittivity and permeability, but provides poor accuracy for loss factors of low loss materials.

The traditional resonant cavity method is significantly more accurate than the NRW characterization technique, but is only able to measure either dielectric materials which are non-magnetic- or magnetic materials which are non-dielectric. Furthermore, it can only characterize materials at a single frequency. The frequency extended perturbation technique enables the measurement of dielectric or magnetic properties across a bandwidth of approximately 15%, which is a dramatic improvement on the classical single-frequency cavity technique.

The hybrid characterization technique involves matching computer simulation to physical cavity measurements in order to identify the electromagnetic properties of the material under test in a resonant cavity. This technique is computationally more intensive than the other techniques, but it provides the ability to make highly accurate measurements of the material loss factors for materials exhibiting both permittivity and permeability simultaneously.

CHAPTER 5

A miniaturized Patch Antenna on Magnetic Metamaterial Substrate

In the space of one hundred and seventy six years the Lower Mississippi has shortened itself two hundred and forty-two miles. That is an average of a trifle over a mile and a third per year. Therefore, any calm person, who is not blind or idiotic, can see that in the Old Oligic Silurian Period, just a million years ago next November, the Lower Mississippi was upwards of one million three hundred thousand miles long, and stuck out over the Gulf of Mexico like a fishing-pole. And by the same token any person can see that seven hundred and forty-two years from now the Lower Mississippi will be only a mile and three-quarters long, and Cairo [Illinois] and New Orleans will have joined their streets together and be plodding comfortably along under a single mayor and a mutual board of aldermen. There is something fascinating about science. One gets such wholesale returns of conjecture out of such a trifling investment of fact.

Mark Twain

5.1 Chapter Introduction

In order to validate the embedded circuit spiral resonator, a patch antenna with a miniaturization factor that is tunable by resonant frequency was designed, fabricated, and measured. This series of experiments validates that the metamaterial performs as expected and that it is useful for practical applications.

5.2 Metamaterial Design and Fabrication

A metamaterial substrate based on the embedded circuit spiral resonator was designed with a cell-size of $\Delta x = \Delta z = 2\text{cm}$, $\Delta y = 3.028\text{mm}$ (120mils) (Fig. 5.2). The substrate was fabricated on 120 mil thick Rogers RO-4003 dielectric. The spiral resonators were etched from 1/2 oz thick copper (0.017mm) with a line-width (w) and spacing (s) of 0.127mm (5 mils). For our design $lx = lz = 16\text{mm}$, $w = s = 0.127\text{mm}$ and $L_{SG} = 6.24\text{mm}$. Then for a Rogers RO-4003 dielectric host medium $\Delta y = 3.028\text{mm}$ thick, $\epsilon_{r\text{diel}} = 3.38$ and according to (3.3) $C_{\text{spiral}} = 5.3\text{pF}$, $N = 2$, $S \approx 2.56 \times 10^{-4}\text{m}^2$ and according to 3.7 $L_{\text{spiral}} = .425\mu\text{H}$. The resonance frequency predicted by (3.8) is therefore 106 MHz, but for the reasons previously described this is an unreliable number and numerical simulation is used to identify the actual resonance frequency which is 250 MHz.

To reduce substrate mass, 33/64'th inch diameter air-holes were drilled along the y-axis into the center of each spiral resonator cell. The final substrate mass is reduced by a factor of approximately 1/3'rd which is significant for a 2cm thick substrate. Figure 5.1 shows a typical strip from which the final substrate was assembled. To determine the effects of these air-holes a numerical analysis of Figure 3.14 with and without air-holes was performed in HFSS. It was found that the inclusion of these air-holes reduced the effective permittivity of the medium along the X and Z axis by only 5%. These drill holes do not strongly influence the substrate EM properties because the majority of electric-field energy storage occurs in the 'gap' region between cells and the magnetic-field storage is unaffected by air gaps.

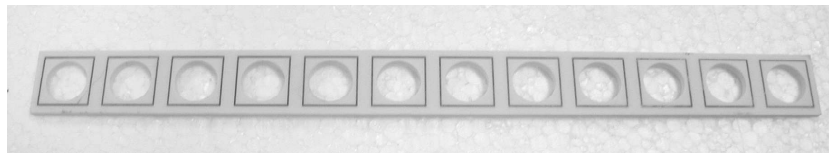


Figure 5.1: 2x24 cm strip of RO-4003 with 12 resonant loop unit cells

The final substrate was formed by stacking XZ-planar strips in the Y-dimension to form the final substrate in the geometry of Figure 3.16. The final substrate was 24 cells in the x-dimension by 75 cells in the y-dimension and one cell in the z-dimension. The resulting total substrate was 24cm x 24cm x 2 cm and had a weight of about 3.5 pounds.

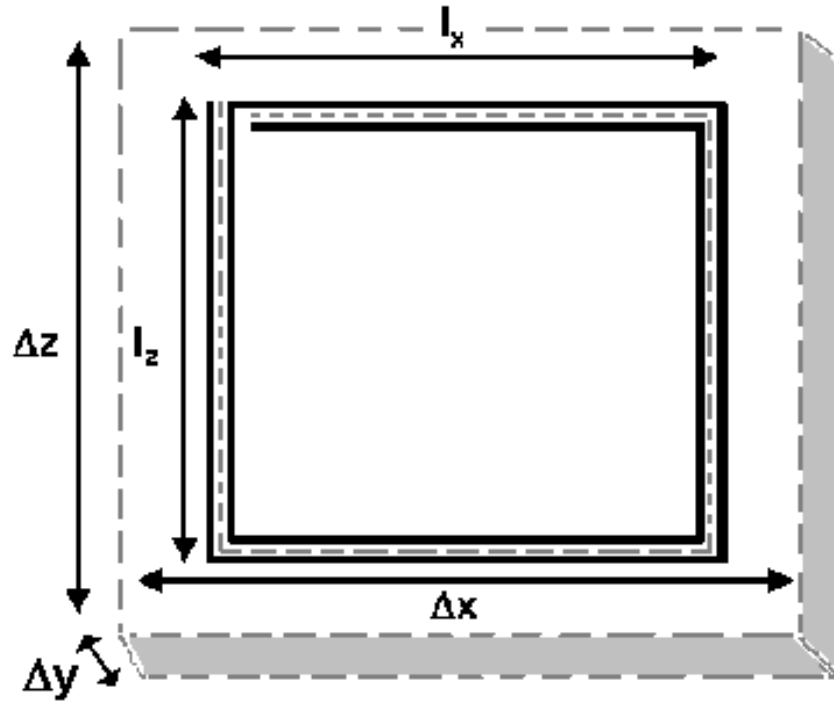


Figure 5.2: The metamaterial unit cell. Δ_x , Δ_y , and Δ_z is the unit cell size. In this diagram $N = 2$ is the number of wraps of the spiral. To achieve permeability enhancement, the magnetic field shall be aligned along the Y axis (normal to the page) and the electric field shall align along either the X or Z axis.

5.3 Metamaterial Performance

With an assembled substrate, the transmission through the medium was measured by electrically small linear probes and a network analyzer as shown in Figure 5.3. Theory predicts such a medium to exhibit a non-propagating condition at resonance. This was observed as a strong drop in measured transmission through the substrate medium at 285 MHz. By this means, the embedded circuit metamaterial resonance frequency (F_{res}) was identified to be 285 MHz. The substrate was originally designed by numerical simulation for a resonance frequency of 250 MHz, and this discrepancy (14%) can be explained by considering the effect of changes in spiral capacitance due to unmeasurable but unavoidable air-gaps caused by imperfect stacking of substrate layers (Fig. 3.12). To investigate the effects of such air-gaps, numerical simulation was performed to consider the effects of a 0.05mm air-gap on our design. Simulations indicate that such a condition would increase the metamaterial resonance frequency of our design by 15%, and this seems to validate the hypothesis that these airgaps are the majority cause of deviation in resonant frequency between measurement and the numerical simulation of the original design.

The ϵ_{reff} and μ_{reff} for a bulk ECSR metamaterial of this design are predicted in Figure 5.4. Equations (3.13) and (3.10) predict that at 250 MHz $\epsilon_{reff} = 9.8$, $\mu_{reff} = 3.1$, and $\tan\delta_m = 0.014$.

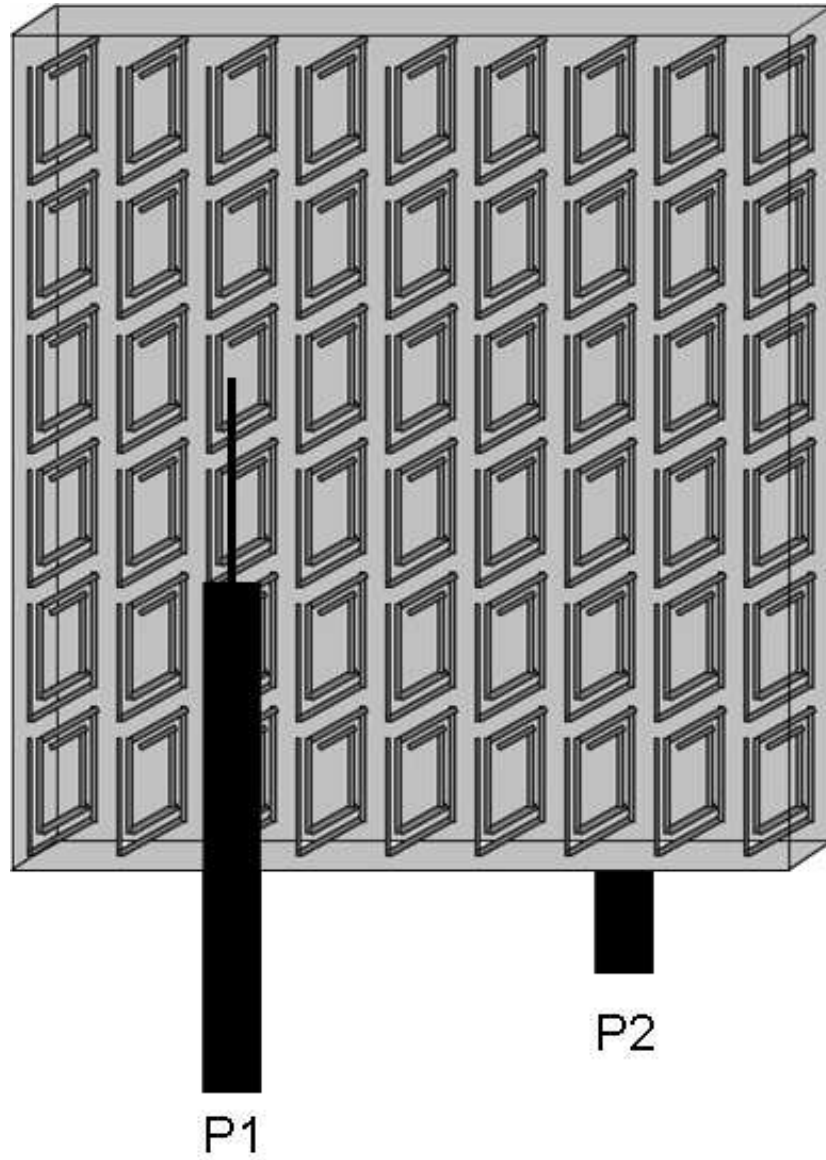


Figure 5.3: Free space Transmissivity/Reflectivity test of metamaterial substrate to identify resonance frequency.

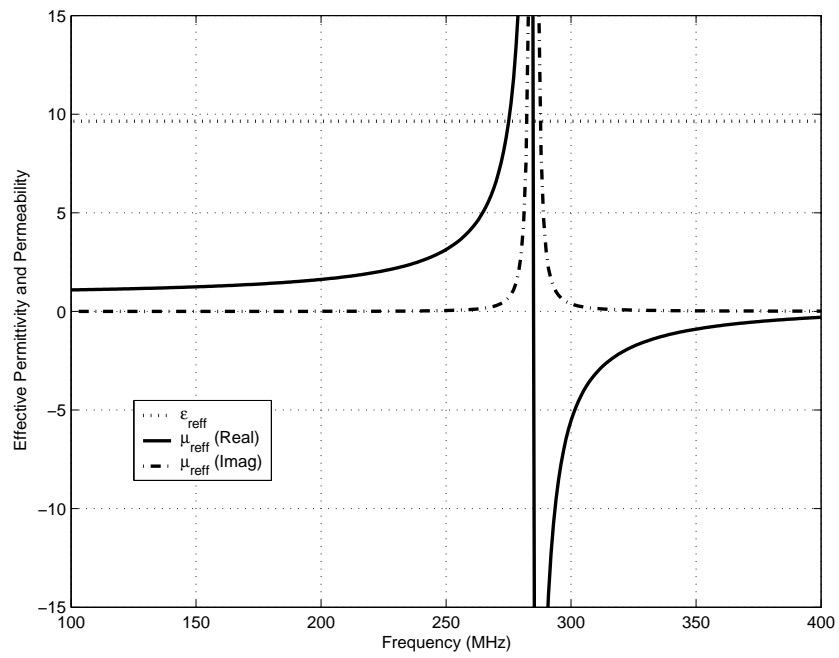


Figure 5.4: Relative Permittivity, and Permeability of metamaterial. At 250 MHz $\epsilon_{r(\text{meta})} = 9.8$, $\mu_{r(\text{meta})} = 3.1$, and $Tan\delta_m$ 0.014.

To better characterize the medium an independent measurement of ϵ_{ref} is also desirable. The analysis of the effective medium assumes an infinite periodic array of embedded circuit elements, but obviously this is not the actual case for a metamaterial substrate. However, this approximation is valid in the area under the antenna patch due to the reflective imaging between the patch and ground metallizations. In accordance with classical image theory, the region between two parallel metallic conductors such as the patch and its ground plane can be analyzed as equivalent to an infinite array whose period is the distance between the metallic plates. Therefore our infinite medium analysis developed in chapter 3 will approximately apply to our application case of a patch over a ground plane.

To measure the achieved permittivity, a test structure similar to the patch antenna geometry is required. The frequency independent form for permittivity given in (3.13) indicates that a low frequency measurement of a parallel-plate metamaterial capacitor would give a reasonable estimate of the high frequency permittivity in the patch-antenna design if the host dielectric itself is non-dispersive.

To perform this measurement a large parallel-plate capacitor was constructed on the meta-material substrate and measured at 2 megahertz with an Agilent E4991A impedance analyzer. The host dielectric itself (Rogers-RO4003) possesses a permittivity of only $\epsilon_{rdiel} = 3.38$ at 2.5 GHz whereas the parallel-plate capacitor fabricated from the embedded circuit metamaterial substrate exhibited an effective permittivity of $\epsilon_{ref} = 13.13$. This clearly shows permittivity enhancement at a level even slightly higher than was predicted. This deviation from theory (3.13) may be due to fringing fields coupling into the under hanging and adjacent loops, or variances in the distances between the spiral edge and the ground-plane or patch metallization. This distance, which is on the order of 2mm, may vary in experimentation by as much as 1mm.

5.3.1 Antenna Performance

Consideration of the field orientations of a patch antenna is beneficial at this time. Figure 5.5 shows the basic geometry of our patch antenna, where the resonant length is indicated by dimension 'L'. A cross-section taken along the XZ plane in the middle of the patch antenna shows the field orientations of the dominant TMZ_{010} in the substrate in Fig. 5.6. The electric fields are oriented along the vertical Z-axis and the magnetic fields are oriented along the Y-axis. These orientations correspond to the directions of electric permittivity and magnetic permeability enhancement in an ECSR metamaterial as established previously. If the patch is oriented as shown in figure 5.5 then the magnetic properties of this metamaterial will be observed, but a patch rotated ninety degrees about the Z-axis, with the resonant length L now along the Y-axis, will experience only dielectric enhancement.

A probe-fed microstrip patch antenna resonant at 250 MHz was built on the metamaterial substrate. To resonate at 250 MHz with a reasonable input match the patch dimensions were found to be 9.3x9.3cm. The final substrate plus patch antenna assembly is shown in Figure 5.5 while the measured antenna gain pattern is shown in Figure 5.7 and Figure 5.8 shows the antenna return loss.

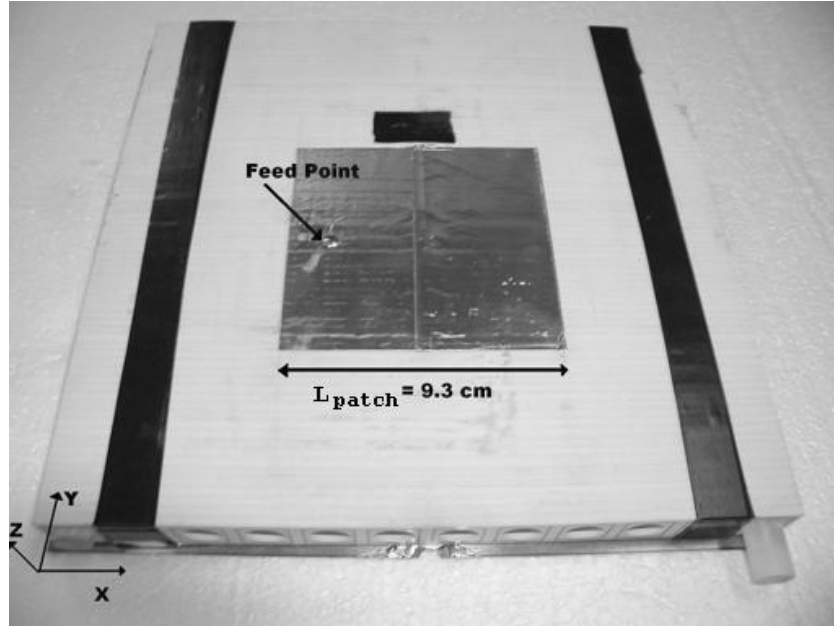


Figure 5.5: Miniaturized microstrip patch antenna on a magnetic metamaterial substrate operating at 250 MHz. The resonant length $L_{patch} = 0.077\lambda = 9.3\text{cm}$.

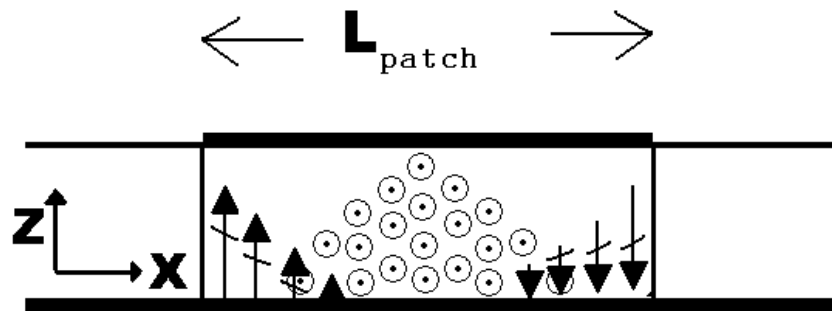


Figure 5.6: Electric and Magnetic field configurations in region beneath microstrip patch antenna. The electric field is aligned along the Z axis and the magnetic field is aligned along the Y axis normal to the page as shown.

As mentioned earlier, this metamaterial substrate can be used to design patch elements with different miniaturization factors since μ_{eff} is a function of frequency. For a material employing simple dielectrics the relationship between operating frequency and physical geometry is fixed to a single miniaturization factor. In a traditional dielectric substrate decreasing the physical dimensions by a factor of two increases the operating frequency by a factor of two and the miniaturization ratio would remain constant. In contrast, for this metamaterial it is possible for a 50% decrease in physical geometries to necessitate only a 20% increase in operating frequency. Therefore, with this metamaterial the miniaturization factor is a function of operating frequency.

The antenna performance parameters, such as the miniaturization and efficiency factors of several patch antenna over the metamaterial substrate operating at different frequencies are given in Table 5.1 and Table 5.2. A patch antenna in free-space will resonate with a length of approximately $\lambda_0/2$ and for our purposes the miniaturization factor is defined as the fraction of this size for which the patch resonates at the same frequency. For example, a miniaturization factor of 5 would indicate that the resonant length of the patch is $\lambda_0/10$.

Our procedure for measuring efficiency was by application of the relationship between gain and directivity. The maximum value of the gain is related to the maximum value of the directivity by [42]

$$G_0 = eD_0 \tag{5.1}$$

The maximum gain (G_0) of the antenna under test was measured experimentally by comparison to an antenna of known gain. To determine directivity, pattern measurements were taken along the primary E-plane and H-plane cuts. Since this is a low directivity antenna, these measurements were sufficient to approximate the total antenna pattern and directivity was calculated from the classic formula [42]

$$D_0 = 4\pi \frac{U_0}{\int_0^{2\pi} \int_0^\pi U(\theta, \phi) \sin(\theta) d\theta d\phi} \quad (5.2)$$

There $U(\theta, \phi)$ is the directional radiation intensity and U_0 is the radiation intensity in the direction of maximum radiation. Cross-polarization was also measured, but found to be low enough for these antennas that polarization efficiency was negligible to within the accuracy of the other estimates in this calculation.

To provide comparison, the antenna probe feed position and geometry were also adjusted to provide a resonant dimension along the Y-axis rather than the X-axis used previously (See Figure 3.16). In this orientation there should be no effective permeability experienced by the antenna, but permittivity should remain enhanced. That is $\mu_r = 1$ but ϵ_{reff} is given by (3.13).

Table 5.1: Antenna Parameters

0.077 λ Patch Antenna at 250 MHz over Magnetic Metamaterial Substrate	
Return Loss	-11.9 dB
-10dB RL BW	0.83%
Gain	-3.9 dBi
Directivity	3.4 dBi
Cross-Pol Ratio	-12 dB
Efficiency	19.8%
Miniaturization Factor	6.45

Table 5.2: Miniaturization and Efficiency

Description	Frequency	Resonant Length	Miniaturization Factor	Efficiency
Aligned	215 MHZ	150mm	4.65	31.92%
Aligned	240 MHZ	125mm	5.00	27.35%
Aligned	250 MHZ	93mm	6.45	19.80%
Anti-Aligned	250 MHZ	195mm	3.08	10.84%

As shown in Table 5.2 the Anti-aligned 250 MHz case exhibits a miniaturization of just greater than three which is predicted by the theoretical and measured

permittivity enhancement alone, indicating no permeability enhancement. In this patch orientation the magnetic enhancement of the material does not provide for miniaturization and as a result the patch is comparable to the size of the ground-plane. This nearly parallel plate capacitor structure suffers from somewhat stronger edge-effects and therefore should exhibit lower efficiency. That the non-magnetic orientation of operation yields significant losses indicates that the losses observed in the permeability-enhanced orientation are not entirely caused by the magnetic loss-tangent itself. The ohmic losses of the patch, ground plane, and dielectric loss tangent of the substrate are also contributing to the high losses.

The orientation, frequency dependence, and observed miniaturization factor values reinforces validation of our embedded circuit spiral loop resonator model.

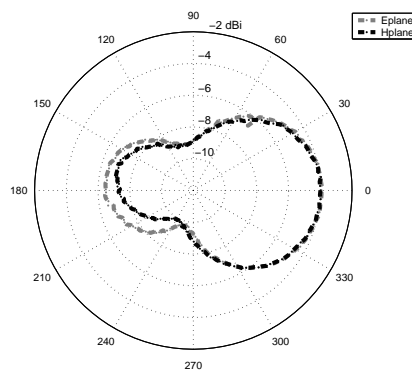


Figure 5.7: Measured antenna gain pattern for patch antenna over magnetic meta-material substrate at 250 MHz.

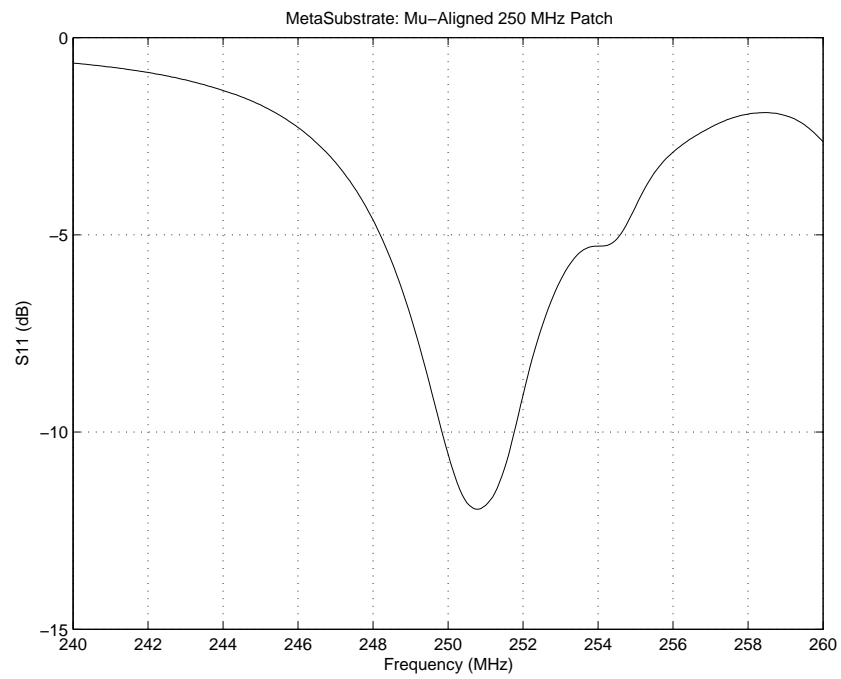


Figure 5.8: Return loss at 250 MHz for probe-fed patch antenna over magnetic meta-material substrate.

Figure 5.8 shows the insertion loss of the 9.3x9.3cm patch antenna to be around 250 MHz. This figure indicates a more difficult input matching condition than the bulk material properties $\epsilon_{eff}, \mu_{eff}$ would imply. This is due to the material bulk properties not being perfectly representative of the very near field properties in the region around the probe feed. The probe feed does not induce a simple field geometry to interact ideally with the metamaterial anisotropies, the way that the patch itself does. Even so, this is an acceptable feed condition to demonstrate the properties of metamaterial substrates.

The observed efficiencies in this experiment are lower than would be predicted by Eq. (3.10). This is at least partially due to the overly simplifying assumption of Eq. (3.12). The 1/2 Oz copper ($\sigma = 5.8 \times 10^7$ S/m) used as our metallization has a skin-depth of $10.5 \mu m$ at 250 MHz. Since 1/2 Oz copper is only $17 \mu m$ in thickness, (3.12) predicts a higher performance than is realizable with this metallization. Numerical simulation indicated that a thicker metallization $70 \mu m$ (2 Oz) will improve the magnetic loss tangent by a factor of almost 2, and this should improve antenna efficiency levels. An additional source of loss is the dielectric loss tangent of the host dielectric material. Numerical simulation indicates that decreasing the host material dielectric loss tangent will significantly improve the efficiency of the effective medium, but not as strongly as improvements to the metallization would.

To investigate the impact of changes in material loss tangent on antenna efficiency, a patch antenna on an anisotropic theoretical substrate whose properties are modeled according to (3.9) and (3.14) was simulated. With a copper patch and ground plane $35 \mu m$ thick, on a 2cm thick substrate ($\epsilon_{rdiel}=3.38$, $\epsilon_{reff}=9.8$, $\mu_{reff}=3.1$, and $Tan\delta=Tan\delta_e=Tan\delta_m$) numerical analysis of a 250 MHz patch was performed using HFSS software. (Fig. 5.9)

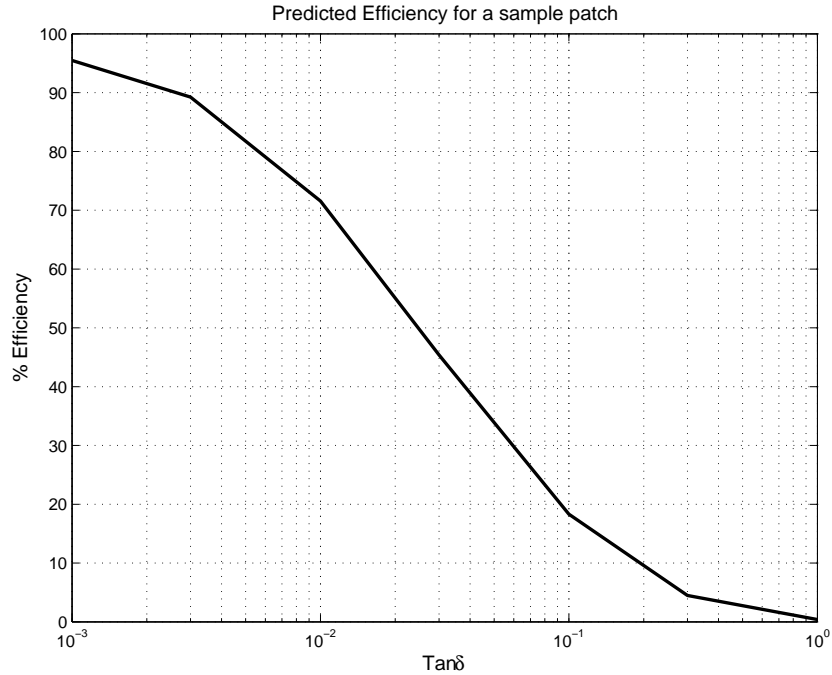


Figure 5.9: Radiation Efficiency of a patch at 250 MHz verses substrate material loss tangent on modeled metamaterial substrate.

5.4 Chapter Conclusions

A naturally non-magnetic dielectric was imbued with magnetic properties and permeability by means of embedded circuit spiral resonators. This metamaterial substrate possesses enhanced positive values of permeability with reasonable loss levels. A microstrip patch antenna was developed and tested to demonstrate the potential application of these embedded circuit magnetic metamaterial substrates. Miniaturization factors on the order of 4-7 and moderate efficiencies of 20-30% were observed, validating that various miniaturization factors may be selected in a miniaturization vs. efficiency optimization trade-off using a single material. Higher efficiencies should be achievable with judicious metallization choice. This experiment indicates the validity of the embedded circuit resonator metamaterial analytical model.

Embedded circuit MetaMaterials like those described here have been fabricated for applications of up to 2.5 GHz and simulations indicate that with commercially avail-

able materials and processing technology, magnetic metamaterials produced by this technique can operate in frequency ranges of up to about 10 GHz with permeability in the $\mu_r = 1 - 5$ range for moderately low-loss applications.

CHAPTER 6

Patch Antenna Over Reactive Impedance Surface

Theory is splendid but until put into practice, it is valueless.

James Cash Penney

6.1 Chapter Introduction

The perfect electric conductor (PEC) and perfect magnetic conductor (PMC) are two extremes on the spectrum of reactive impedance surfaces (RIS). Although PEC's have well known shortcomings, they are extremely simple to implement. In contrast, PMC's seem to offer superior properties, but they have proven exceedingly difficult to realize despite a great deal of recent research effort.

The generalized reactive impedance surface (RIS) is superior to either the PEC or PMC inasmuch as that it can be tuned specifically to provide the properties needed for a specific application. For our purposes, a RIS is tuned to minimize the interaction between a radiating source current and the 'image' current it produces due to the reflections on the RIS. Other researchers have pursued other RIS designs with other goals [43].

By minimizing the interaction between a source antenna and its image, the antenna system performance can be dramatically improved. Various RIS tuning tech-

niques are employed to improve bandwidth, provide miniaturization, and increase gain.

6.2 Motivation

Smaller physical size, wider bandwidth, and higher efficiency are three desired characteristics of antennas for mobile systems. Antenna miniaturization utilizing a patch antenna printed on a metal backed high dielectric substrate has been attempted previously [44]. The drawbacks of this approach are twofold 1) there is a strong electromagnetic coupling between the patch and the PEC surface backing the high permittivity substrate which traps a significant portion of EM energy in the nearfields resulting in a low antenna efficiency, narrowband characteristics, and in some cases a degraded radiation pattern due to surface waves and leaky waves, 2) the characteristic impedance in a high permittivity medium is rather low and that creates difficulty in impedance matching of the antenna. Such challenges can be successfully circumvented by the novel design of patch antenna over a Reactive Impedance Surface (RIS) [45]. The RIS has the minimum interaction with the patch and dramatically enhances antenna performance metrics, namely, size, bandwidth, and efficiency.

6.3 Patch Antenna over the RIS Substrate

It is demonstrated in [45] that a reactive impedance plane with $\eta = j\nu$ can be tuned to exhibit the minimum interaction with the antenna located above it by judicious selection of " ν ". To realize such a RIS backplane, a periodic surface of FSS (Frequency Selective Surface) patches printed on a metal-backed dielectric material as illustrated in figures 6.1 and 6.2 is employed. When a wave is incident on such a structure at normal incidence the the FSS patches store capacitive energy between adjacent unit cells (Figure 6.3) and a parallel inductive effect is contributed by the

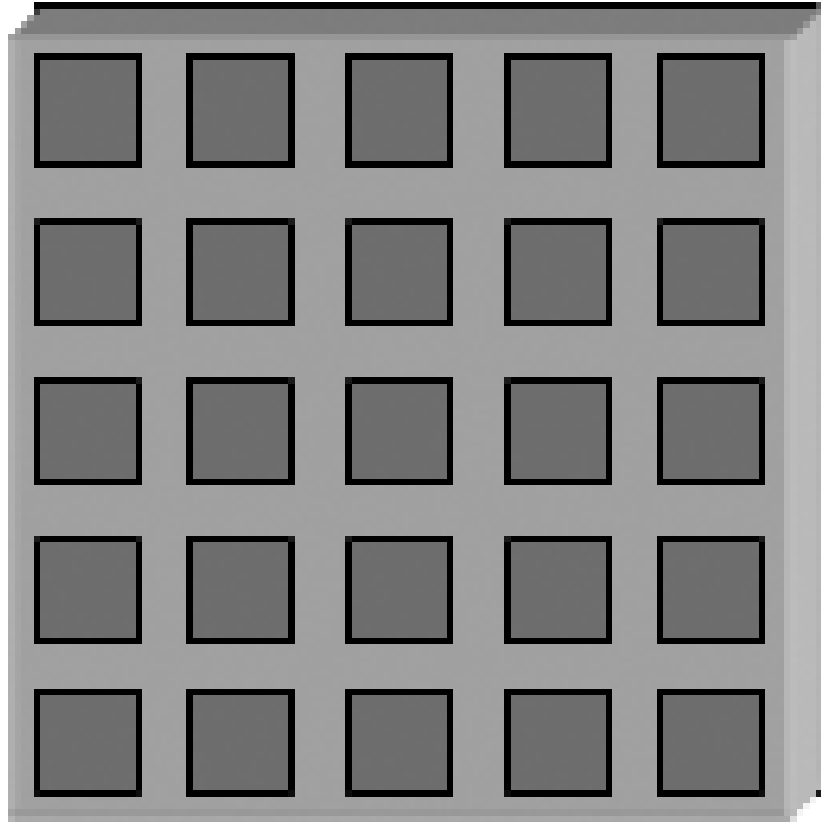
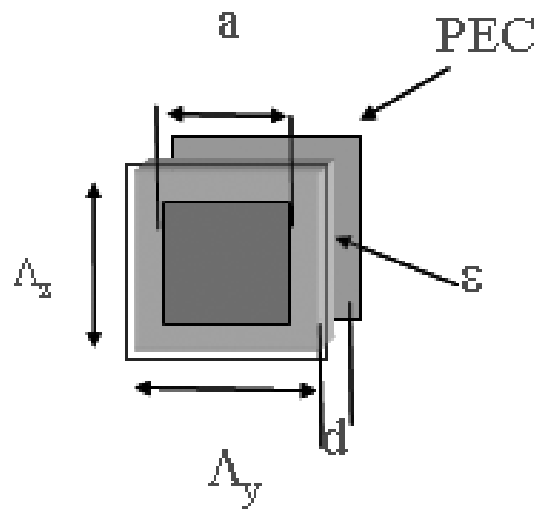


Figure 6.1: A Reactive Impedance Surface (RIS) composed of small metallic patches over a PEC backed dielectric substrate.

phase delay caused by the wave propagating to the PEC back-plane through the the substrate between FSS and PEC, then reflecting back (Figure 6.4). Thus, the composite periodic structure is equivalent to a parallel LC circuit which can be tuned by adjusting geometric parameters to provide the desired reactive impedance (Figure 6.5). The Finite Difference Time Domain (FDTD) technique with PBC/PML boundary conditions [46] may be applied to characterize the structure and the impedance behavior of the surface. The results of such a simulation are presented in figures 6.6 and 6.7. The results of figures 6.6 and 6.7 compare very well with the predictions of the circuit model which is presented next.



$$\begin{aligned} \epsilon_r &= 25.0, \mu_r = 1.0, \text{tg} \delta_1 = 0.001 \\ \Lambda_x &= \Lambda_y = 1.20 \text{ cm}, d = 0.40 \text{ cm} \\ a &= 0.80 \text{ cm} \end{aligned}$$

Figure 6.2: A Reactive Impedance Surface (RIS) Unit Cell.

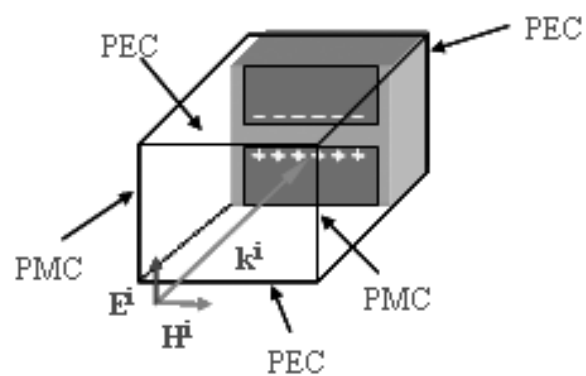


Figure 6.3: Capacitance between Reactive Impedance Surface (RIS) Unit Cells.

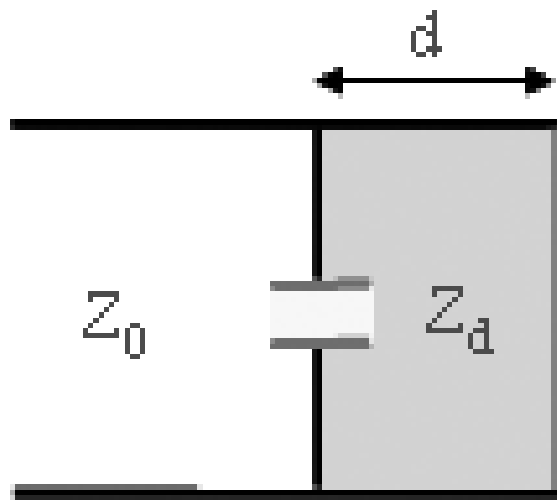


Figure 6.4: A Parallel Inductive effect from the phase delay of the traveling through the underlying substrate.

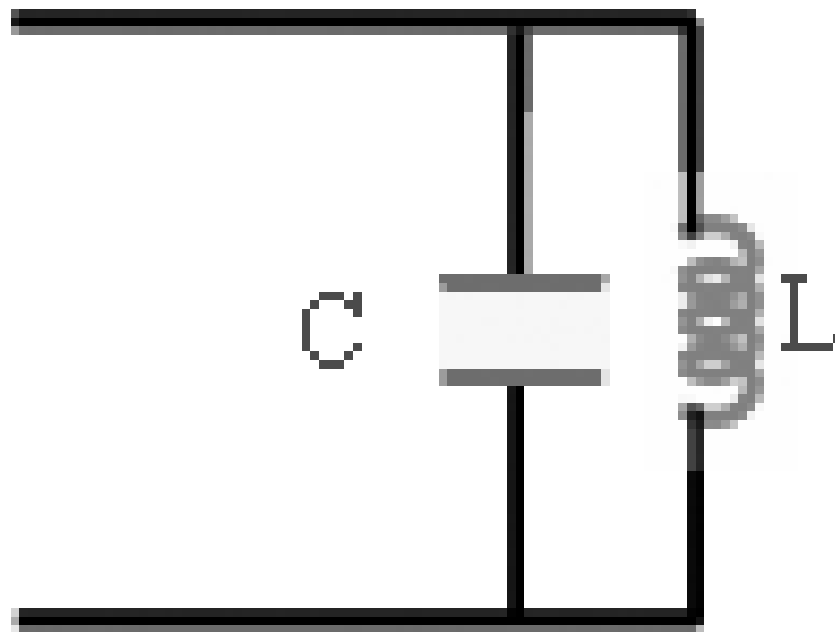


Figure 6.5: The equivalent circuit model for the parallel capacitance and inductance in a RIS.

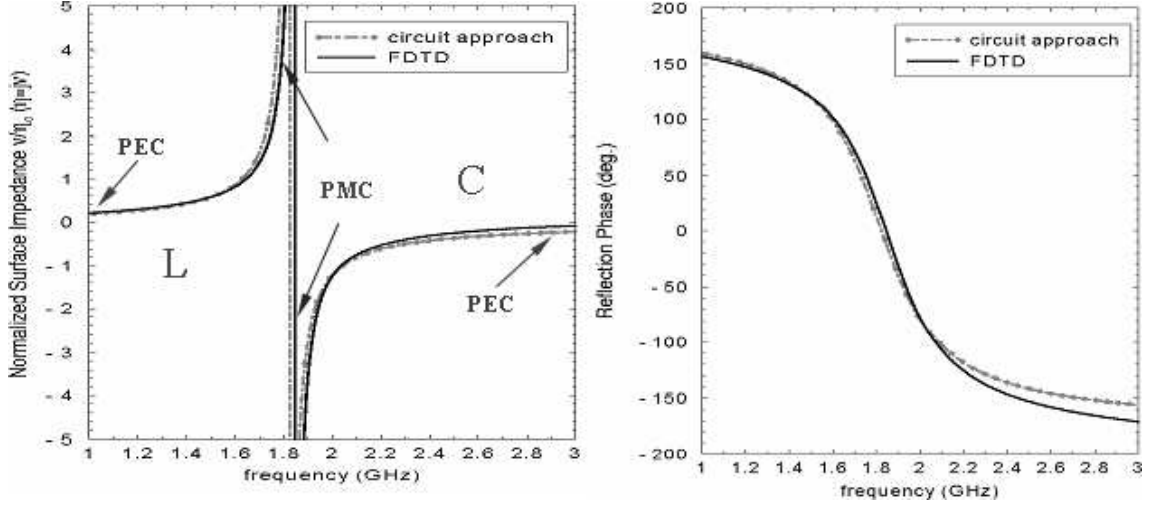


Figure 6.6: Normalized Surface Impedance at Normal Incidence

Equivalent Circuit Model

According to the circuit model of figure 6.5, the equivalent surface impedance of such an RIS is $\eta = j\nu = j X_{LC}$, where X_{LC} is the parallel combination of the capacitance X_c and inductance X_L .

$$\eta = j \frac{X_c X_L}{X_c - X_L} \quad (6.1)$$

At normal incidence, the inductance X_L is a function of the thickness (d) and dielectric constant (ϵ_r) of the substrate between the metallic patch grid and the PEC backplane.

$$X_L = Z_d \tan(kd) \quad (6.2)$$

$$k = k_0 \sqrt{\epsilon_r} \quad (6.3)$$

$$Z_d = \eta_0 / \sqrt{\epsilon_r} \quad (6.4)$$

At oblique incidence, X_L can be approximated.

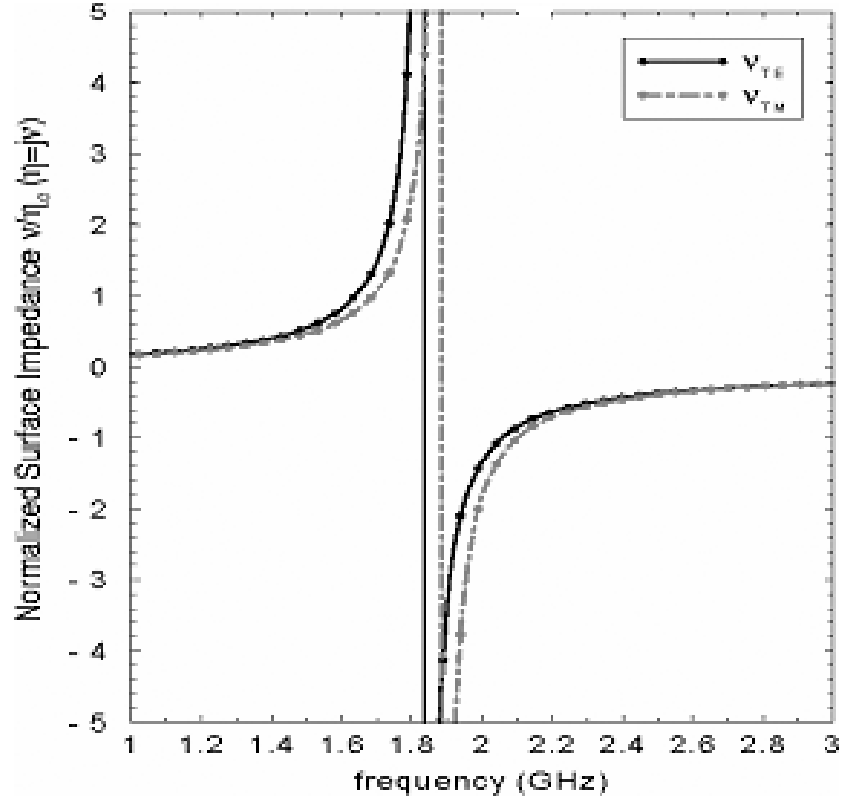


Figure 6.7: Normalized Surface Impedance at Oblique Incidence

$$X_{L,TE} = (Z_d / \cos\alpha) \tan(kd \cos\alpha) \quad (6.5)$$

$$X_{L,TM} = (Z_d \cos\alpha) \tan(kd \cos\alpha) \quad (6.6)$$

The circuit model for the capacitance (X_C) is a function of the geometries and the materials above and below it.

$$X_C = 1/\omega C \quad (6.7)$$

$$C = \frac{\epsilon K(\sqrt{1 - (z_1/z_2)^2})}{K(z_1/z_2)} \quad (6.8)$$

$$K(z) = \int_0^{z/2} \frac{d\phi}{\sqrt{1 - z^2 \sin^2\phi}} \quad (6.9)$$

Figures 6.6 and 6.7 validate that the equivalent circuit model provides a good approximation of the surface impedance experienced by a wave incident upon such a RIS.

Antenna Design

A miniaturized patch antenna over a dielectric substrate and RIS backplane was design. This patch antenna was tuned to operate at $f_r=1.86\text{GHz}$ and the longest patch dimension is about $\lambda_0/10$. The RIS geometry is shown in figure 6.2 and the reactive impedance expected from such a RIS is shown in figure 6.8. Simulations comparing the performance of such an antenna to an equivalently miniaturized patch over a PEC shows that the bandwidth is enhanced dramatically to $\text{BW} = 4.96\%$ 6.9. According to FDTD simulation the directivity of is antenna is $D = 4.8\text{d5}$ and a 5.6 d5 front-to-back ratio is achieved (Figure 6.10). Notice that, using the conventional high dielectric substrate the trapped EM waves inside in the high permittivity material prevents proper matching of the antenna as illustrated in figure 6.9. Therefore, the unique properties of reactive impedance surfaces presents a novel meta-backplane for miniaturized wideband planar antenna design with high efficiency performance.

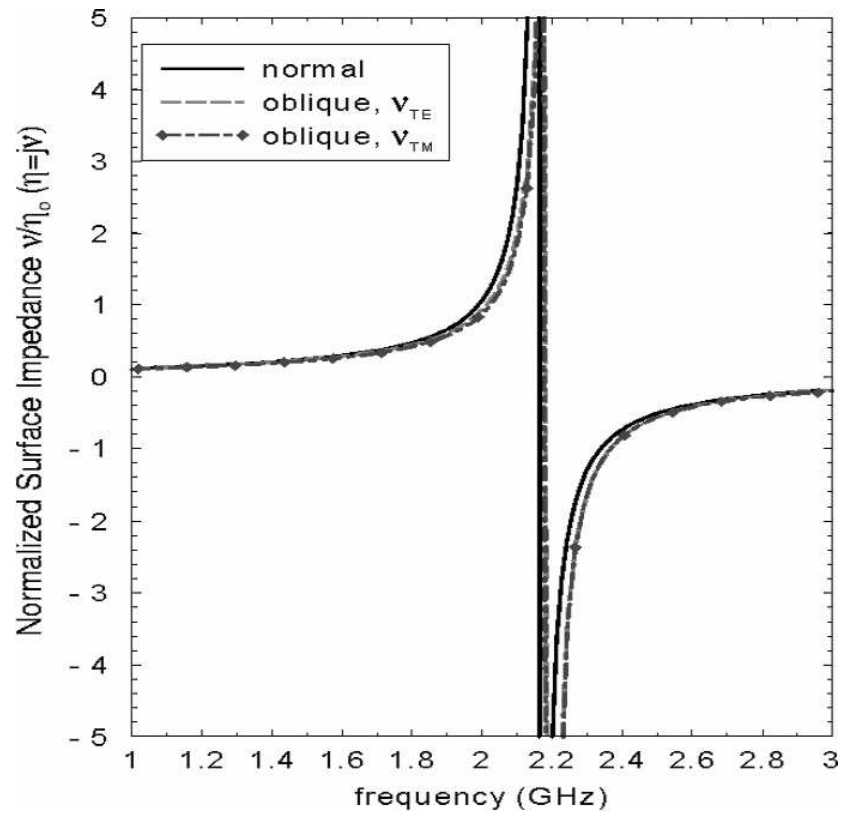


Figure 6.8: RIS Surface impedance for 1.86 GHz patch antenna.

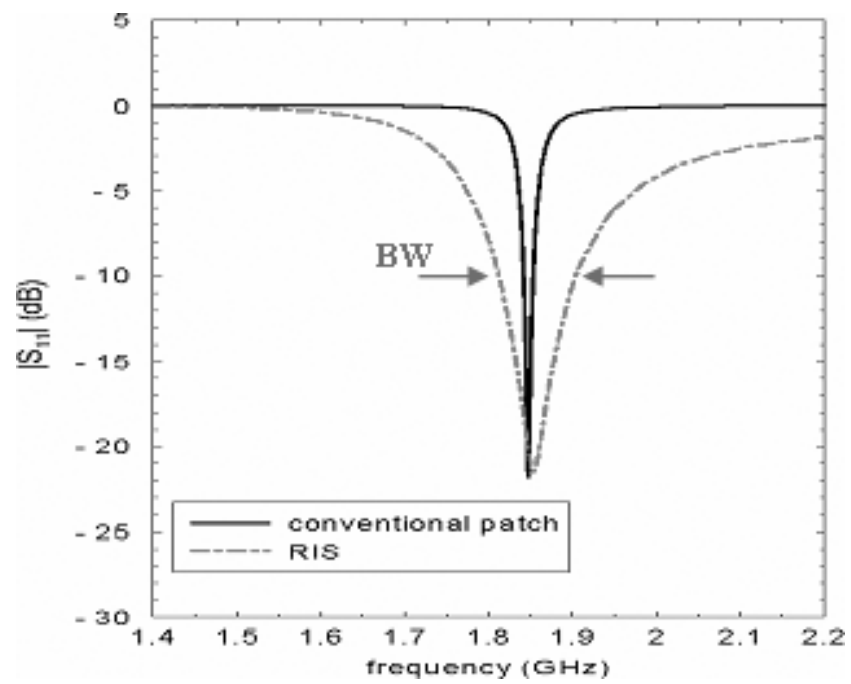


Figure 6.9: Impedance bandwidth of patch antenna over RIS and equivalent conventional substrate.

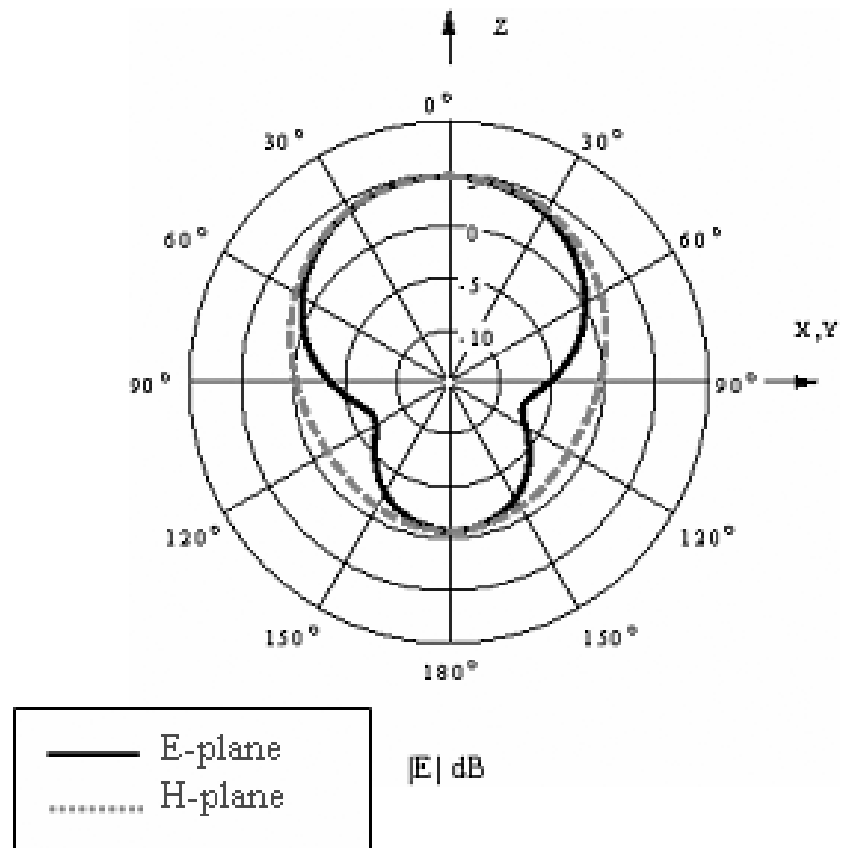


Figure 6.10: Radiation pattern for miniaturized patch over RIS.

6.4 Fabrication

The dielectric material used for the patch antenna was Trans-Techs D-6, a magnesium silicate ($\epsilon_r=6$) commonly known as forsterite. The RIS substrate was Trans-Techs MCT-25 between the PEC and grid of metallic squares. MCT-25 is a Magnesium calcium titanate composition ($\epsilon_r=25$). Both materials were fabricated by reacting the individual chemical constituents at high temperature to form a powder. Blocks were fired and subjected to another high temperature firing to achieve the desired dielectric properties. From these blocks, substrates were machined to the desired size using a thick film silver paste and Trans-Techs screen printing process. The array of FSS patches, corresponding metal backing, and patch were all generated by this process. Both substrates were heat treated to form an intimate bond of the silver to the dielectric material. This intermediary stage is diagrammed in figure 6.11. Using a two part, low loss dielectric adhesive, the substrates were assembled in a fixture to ensure alignment. The feed-hole was then drilled into the assembly. Finally, the feed-thru pin was machined from hardened brass and soldered to the silver patch. The completed antenna structure is shown in figure 6.12.

6.5 Measurement

The return loss of the patch antenna over RIS substrate was measured using a modern vector network analyzer and is shown in figure 6.13. The antenna resonance was found to be 1.92 GHz and it exhibited matching far superior to traditional patch antennas, with better than 25dB input matching at resonance and a -10dB impedance bandwidth of 6.71%. This validates the FDTD model based design which exhibited a resonant frequency of 1.86 GHz, 22dB peak matching and a -10dB impedance bandwidth of 6.99%. The radiation pattern was measured in an anechoic chamber at the University of Michigan Radiation Laboratory. Two calibrated standard gain

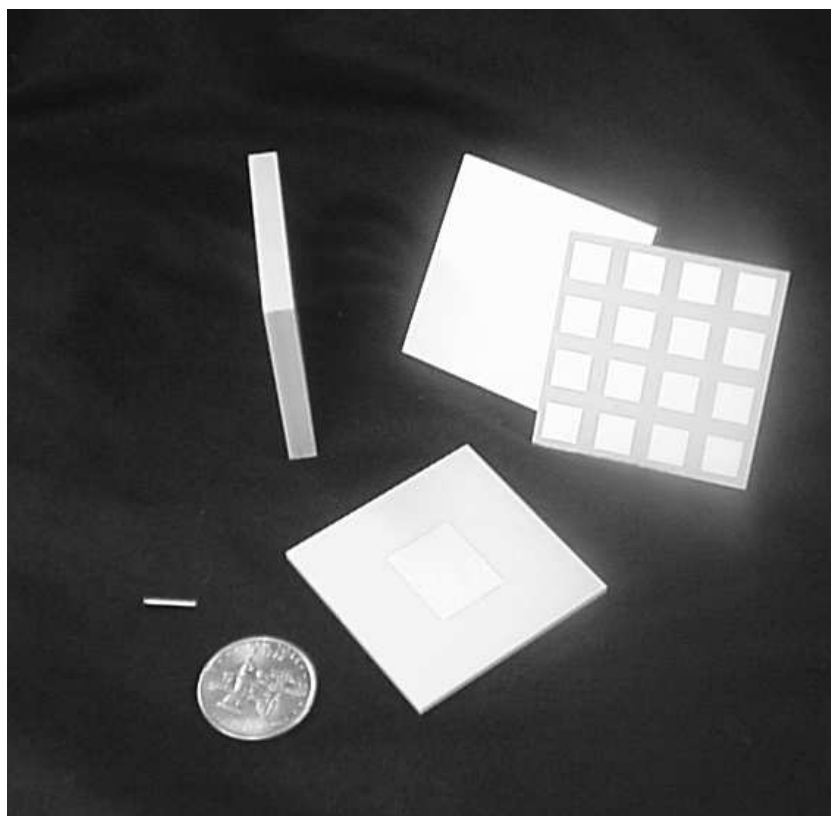


Figure 6.11: The elements of the RIS patch antenna.

antennas were employed to characterize the path loss and radiation environment of the chamber at the antenna operating frequency. The standard gain antenna in transmitting mode in the anechoic chamber quiet region was replaced with the patch antenna to be measured while the receiving antenna was kept fixed at the chamber far end. When the patch was oriented for optimal reception by the standard gain antenna, the signal level had dropped relative to the standard gain antenna configuration to a level indicating a patch antenna absolute gain of 4.5 dB. The patch antenna was rotated along its E and H planes and the received signal power was recorded as a function of patch orientation angle. Figure 6.14 indicates the radiation pattern observed. Radiation pattern measurement yielded 4.5dB gain, a 5.6dB front/back ratio, and an efficiency of 93%. This validates the model predicted performance parameters of 4.8dB gain and 5.6dB front to back ratio.

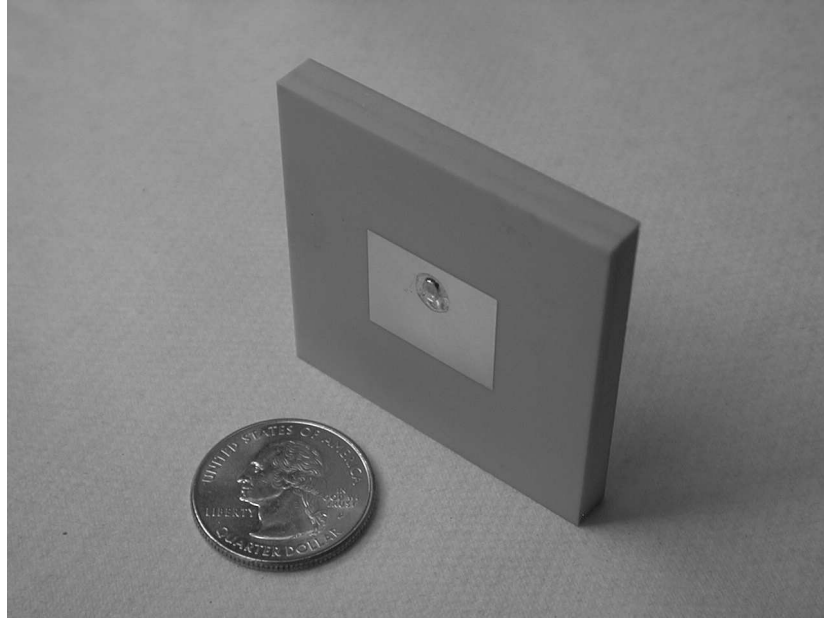


Figure 6.12: The final assembled Patch antenna on RIS.

6.6 Chapter Conclusions

By selectively tuning the RIS to provide an optimum interaction with a nearby radiating source element, miniaturized patch antenna performance is optimized. With 6.71% -10dB impedance bandwidth at 1.92 GHz, Gain of 4.5 dBi, and a front to back ratio of 5.6 dB, this $\lambda_0/10$ patch antenna on a $\lambda_0/3 \times \lambda_0/3$ substrate and ground plane exhibited 93% radiation efficiency. To our knowledge this is the highest reported gain and bandwidth for such a small planar antenna.

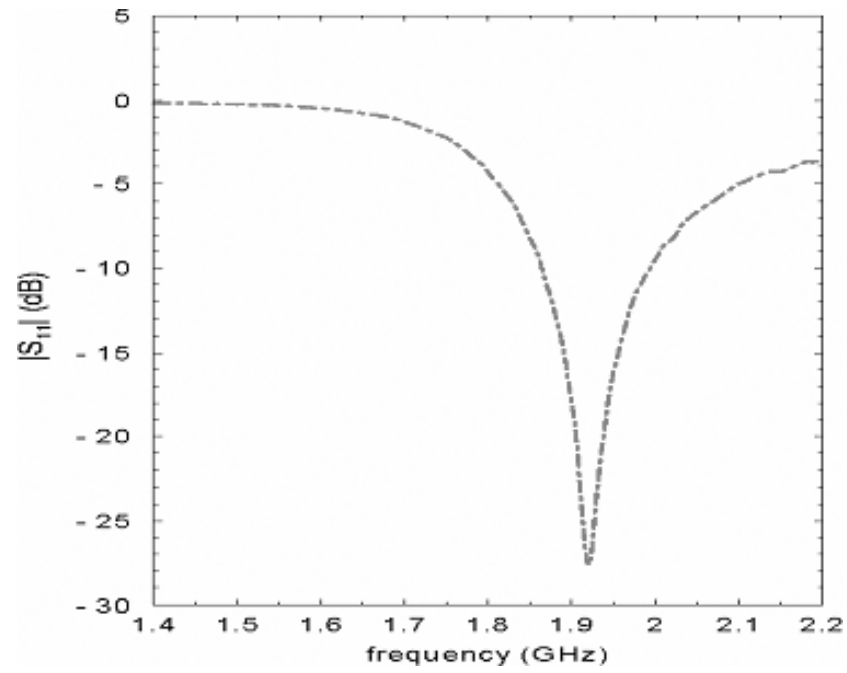


Figure 6.13: Experimentally measured impedance bandwidth

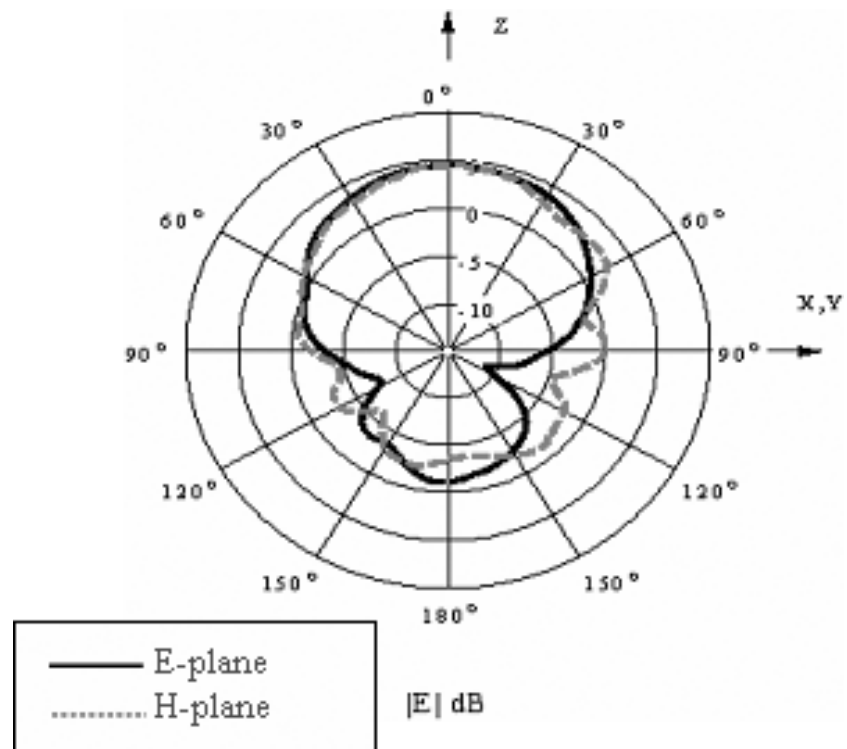


Figure 6.14: Experimentally measured radiation Pattern

CHAPTER 7

Electromagnetic MetaMaterial Insulator

I recognize that many physicists are smarter than I am—most of them theoretical physicists. A lot of smart people have gone into theoretical physics, therefore the field is extremely competitive. I console myself with the thought that although they may be smarter and may be deeper thinkers than I am, I have broader interests than they have.

Linus Pauling

7.1 Chapter Introduction

The basic function of metamaterial insulators is the blocking of EM energy from being transmitted across the insulation boundary. Such a component tool is useful in the toolbox of microwave designers for many applications such as isolating stacked RF circuit boards, providing isolation between the power amplifiers and LNA's in an RF front end, and improving the Front-to-Back ratio of antennas by blocking ground-plane currents from wrapping around to the backside of ground-planes.

7.1.1 Preview of Metamaterial Insulators

Metamaterial EM insulators are formed by embedded circuit metamaterials operating in a non-propagating spectral region such as is observed in the field of optics for EM Bandgap (EBG) materials. By this mechanism, metamaterial insulators can

dramatically reduce mutual coupling between densely packed circuit elements. A single $0.05\lambda_0$ thick layer of embedded circuit Metamaterial insulators placed between radiating antenna array elements achieves better than 20dB reduction in mutual coupling, effectively eliminating the mutual coupling in all but the most densely packed arrays [[47],[48]].

Embedded Circuit Metamaterials are a rapidly evolving topic currently, and a great deal of literature is being produced which explains the physics of EC metamaterial operation and the design procedures to fabricate for a specific resonant frequency. [49]

7.2 Theory of Metamaterial Insulators

A lengthy description of the design of metamaterial resonators and their properties is published in the literature [49]. For our purposes, a brief summary of embedded circuit metamaterials is sufficient.

Embedded circuit metamaterial resonators are small spiral metallic loops embedded in a host dielectric. The typical geometry for a single resonant element is shown in Fig. 7.1[29].

These single element resonators are stacked to form solenoidal structures, which couple any properly polarized incident magnetic energy. This coupled incident magnetic energy excites a current in the spiral loops, generating a magnetic field of its own. This magnetic field stores magnetic energy in the form of a magnetic dipole moment which was coupled by the incident wave and this magnetic energy storage is the definition of permeability and is the reason this otherwise non-magnetic structure exhibits an effective permeability.

The magnetic energy storage in EC metamaterial resonators is a bulk property (permeability) which is not present in either the copper or the host dielectric. Because

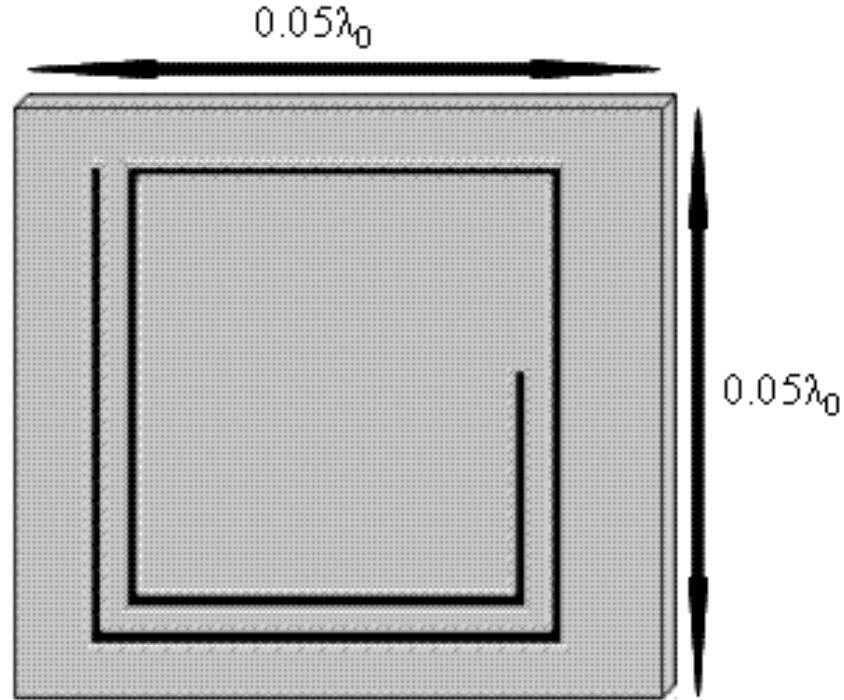


Figure 7.1: Embedded Circuit (EC) Metamaterial Resonators consist of a planar metalized spiral in a dielectric host medium. The insulator operating frequency is tuned by the spiral resonance and for our design the insulators are $0.05\lambda_0$

the permeability is a function of the induced current magnitude, in order to enhance the permeability of the metamaterial the spirals are operated near their resonance frequency when resonant current gain occurs. The spirals possess both inductance and a distributed capacitance. The resulting LC resonance is exploited for our purposes.

Analytic equations describing the behavior of a bulk-material made from such spirals are published, but more involved that is necessary for our purposes here [49]. The bulk properties of such a metamaterial medium is a function of the metal conductivity, spiral geometry, and the host dielectric.

For our purposes, since only a qualitative understanding is required here, a discussion of the basic trends of the metamaterial bulk permittivity and permeability as shown in Fig. 7.2 will suffice.

The permittivity of the host medium is enhanced anisotropically by the capaci-

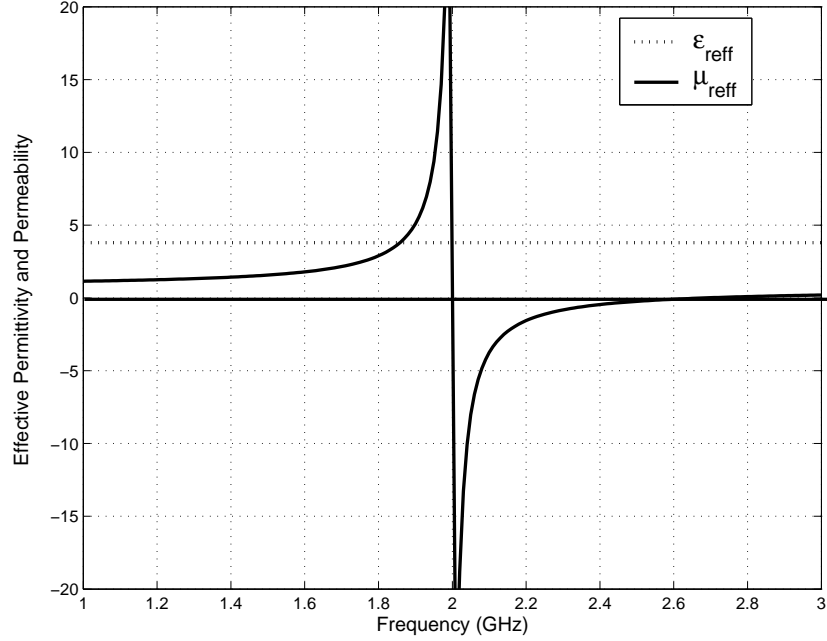


Figure 7.2: The anisotropic permittivity (ϵ_{reff}) and permeability (μ_{reff}) exhibit a band-stop region immediately above resonance when $\mu_{\text{reff}} < 0$ and $\epsilon_{\text{reff}} > 0$

tance between the metamaterial unit cells, and is non-dispersive in the region around the spiral resonant frequency. The permeability is also anisotropically enhanced, but is strongly a function of frequency in the region around the resonance. As resonance is approached from lower frequencies the resonant current gain increases the magnetic energy storage and the effective permeability increases rapidly with frequency. Immediately above resonance, the magnetic field energy storage experiences a phase reversal from lagging to leading the incident magnetic field and the permeability becomes negative. This region, where permittivity is positive and permeability is negative is the insulating region.

It is important to realize that although 3D isotropic operation can be readily achieved by more complex EC stacking geometries, the most straight-forward geometry, which is the one considered here, is anisotropic. For this reason, EC orientation must be selected for the magnetic field polarization to be blocked.

7.3 Theoretical Isolation Performance

The most basic geometry for measuring the effectiveness of metamaterial insulators is a wall of solenoid-like rows which are infinite in height and width and one layer thick. A plane wave at normal incidence to the metamaterial wall produces a reflected wave (reflection coefficient $\Gamma=S_{11}$) and a transmitted wave (transmission coefficient $\tau=S_{21}$) which can be simulated as a semi-infinite periodic medium in commercially available numerical electromagnetic solvers such as HFSS by employing the proper boundary conditions [49].

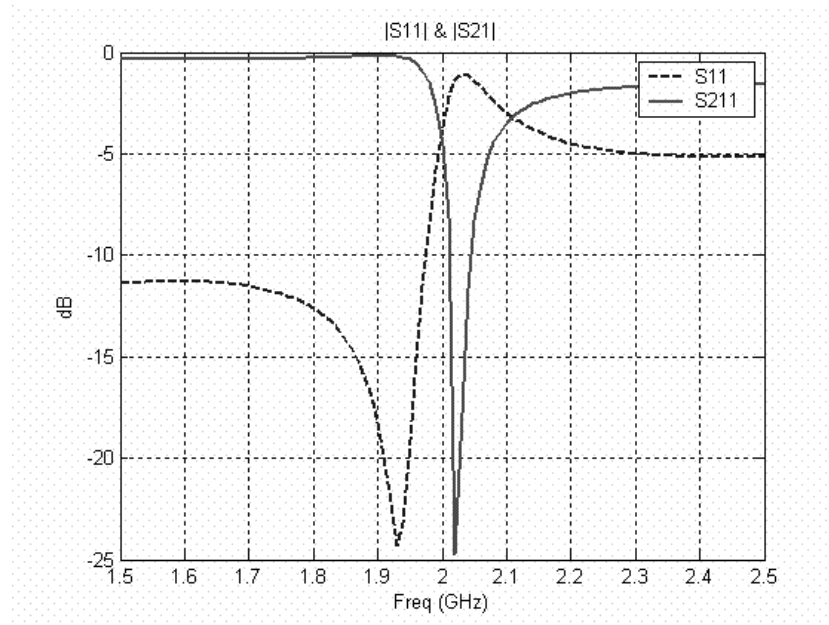


Figure 7.3: The transmission (S_{21}) and reflection (S_{11}) at an infinite wall clearly shows an insulating region where nearly all the energy is reflected. This occurs immediately above the 2.0 GHz spiral resonance

The transmission and reflection through this metamaterial slab is shown in figure 7.3. The region of interest for insulator applications is the strong stop-band region occurring just above 2GHz. For this realization, which was simulated in HFSS for copper spirals and a commercially available host dielectric, there is a -10dB stop-band of 2% bandwidth, and a peak isolation of -25 dB.

By the law of conservation of energy, for a perfectly lossless medium of this geometry $|S_{21}|^2 + |S_{11}|^2 = 1$. In this experiment it is noted that this is not the case, and the metamaterial insulator is introducing some loss. A first order approximation regarding the level of the loss is to observe that $|S_{11}|$ is down approximately 1dB at the insulation peak (where $|S_{21}|$ is a minimum). In other words, approximately 20% of the incident energy is being dissipated in the insulators or lost to depolarization scatter. This is an acceptably low level of loss for many applications, especially where the energy to be blocked is already considered 'wasted' energy and is only a very small fraction of the total system energy.

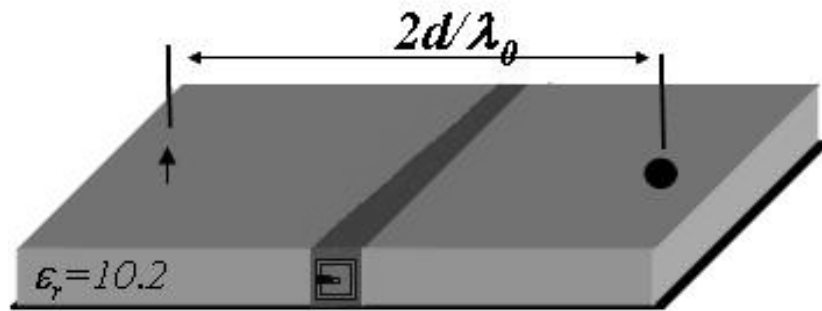


Figure 7.4: Source and observation points on a high dielectric substrate. Metamaterial insulator are shown half-way between the source and observation points, d/λ_0 from each.

In practical application, semi-infinite walls of metamaterial insulators will not often be employed. The more interesting test then, is to observe how a finite wall of insulators performs in a practical geometry. Consider the case shown in Figure 7.4. The electric field magnitude induced at some observation point in a high dielectric substrate due to a point source some distance $2d/\lambda_0$ away on the other side of the insulator wall is shown in Figure 7.5.

The observed field is strongest for observation points near the source on a conventional solid substrate (in the absence of insulator wall) and decreases (Fig. 7.5, 'Conventional') with increasing separation distance. By removing a portion of the substrate and creating an air-gap $0.03\lambda_0$ in width, the observed field is slightly at-

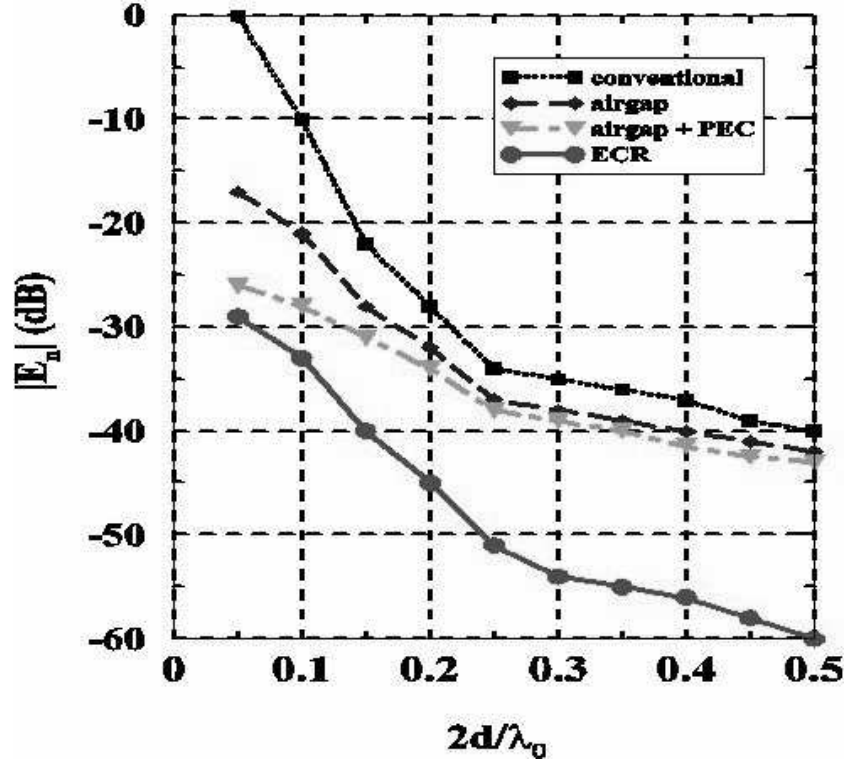


Figure 7.5: Magnitude of electric field induced at the observation point in Figure 7.4.

tenuated as shown ('Airgap'). If a thin PEC wall as tall as the substrate is placed in the center of this gap, coupling is further suppressed slightly ('Airgap+PEC').

When a single $0.03\lambda_0$ metamaterial insulator row is placed between the source and observation points (Figure 7.4), the field magnitude at the observation point is suppressed by 20-30dB (Figure 7.5) (ECR).

To test the isolation capabilities of the embedded circuit isolation wall when located between patch elements an in-house FDTD code was employed to model the two-patch geometry of Fig. 7.6. This geometry was selected to maximize the coupling between adjacent patch antennas and present a 'worst case' scenario. By using an extremely thick ($0.04\lambda_0$) high dielectric ($\epsilon_r = 25$) substrate to maximize trapped substrate waves, a probe-feed for patch excitation, and only $\lambda_0/10$ spacing between patch edges, the coupling between adjacent elements is extremely high. Without the

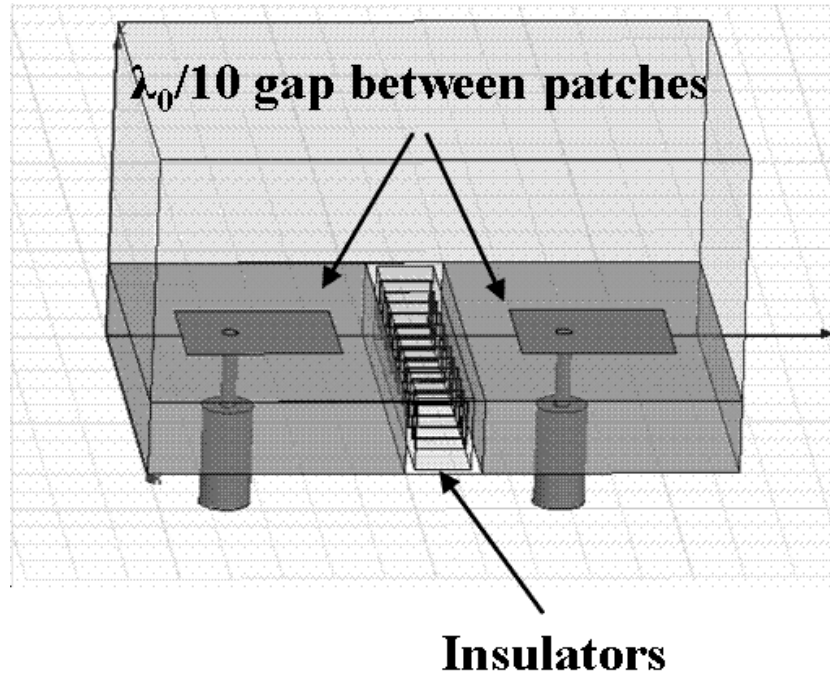


Figure 7.6: Two adjacent patches aligned to produce a strong trapped substrate wave and maximize mutual coupling. The insulator wall of spiral resonators suppresses this coupling

isolation wall present, the close-packing of array elements causes extremely strong mutual coupling, as high as -2dB (Fig. 7.7).

This in-house FDTD code approximates all conductors as PEC's, and all dielectrics were treated as lossless so this is not a suitable reference for efficiency calculations of highly resonant circuits, but when the insulation wall is inserted to this ideal simulation an astonishing 40 dB improvement in mutual coupling is observed with over 6% -10dB bandwidth due to a single insulation layer (Fig. 7.8).

These simulations, if experimentally validated, prove conclusively that metamaterial insulators provide effective isolation.

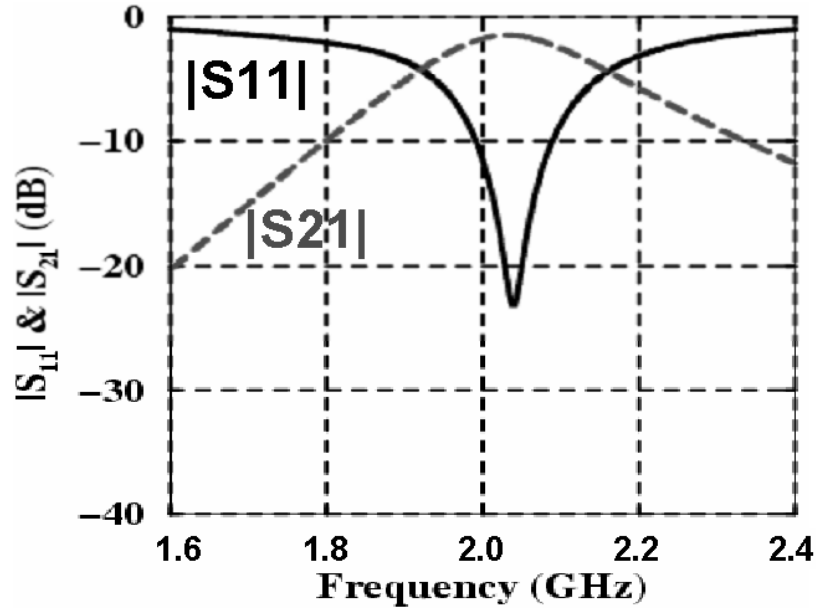


Figure 7.7: With the insulators removed, on a solid substrate the coupling (S21) between the two adjacent probe feeds is strong. The input matching (S11) indicates a well tuned patch.

7.4 Metamaterial Insulator Design, Fabrication, and Measurement

The resonant frequency for the embedded circuit metamaterial resonators is chosen so that their insulating region coincides with the operating frequency of a small patch array. In our case the EC resonance is tuned for 2.0 GHz, and the array operating frequency is intended for 2.02 GHz.

The first-order design of EC geometries proceeds according to the analytical methods [49], and final resonance is tuned in HFSS numerical simulation by adjusting the length of the innermost spiral arm. The desired resonant frequency is achieved (2.0 GHz) after only two design iterations, requiring about 12 hours on a typical desktop PC.

The EC spirals were fabricated by standard commercial etching of $\frac{1}{2}$ Oz copper on 0.125" thick Rogers RT/duroid 5880 ($\epsilon_r=2.2$, $Tan\delta_e = 9 \times 10^{-4}$). The resulting

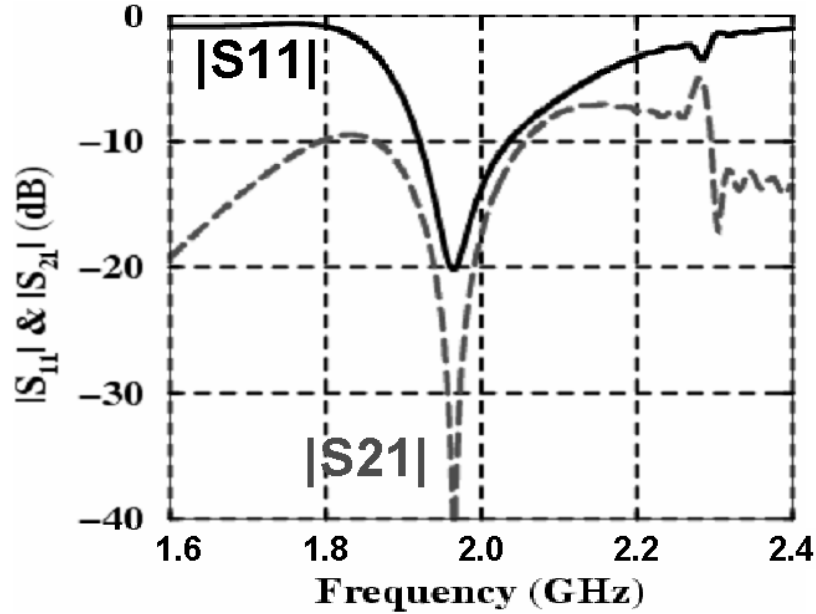


Figure 7.8: When the insulators are returned, a slight shift in resonant frequency occurs but the input matching (S_{11}) is still good. More importantly, the insulators provide excellent suppression of mutual coupling (S_{21}).

EC spirals are shown in Figure 7.9 and then stacked to form a solenoid-like structure which serves as an insulating 'wall' only $0.05\lambda_0$ thick.

For a physical validation of the simulations, geometry similar to that of the simulation geometry in Figure 7.6 was fabricated for measurement (Fig. 7.10). In this physical case the substrate was adjusted somewhat, here $\epsilon_r=15$ and the substrate thickness $T=0.05\lambda_0$.

The input impedance match and coupling were measured directly on a two-port vector network analyzer. First, the input matching and coupling with a $0.05\lambda_0$ airgap between the patches was measured (Figure 7.11) and then the measurement was repeated with the metamaterial insulators in place (Figure 7.12). This measured system performance readily validates the simulations, exhibiting real-world coupling suppression of 22 dB better than the same geometry without metamaterials. For a similar geometry, but with a solid substrate and no air-gap, the ideal simulation performance indicated 40 dB isolation improvement on the solid-substrate case.

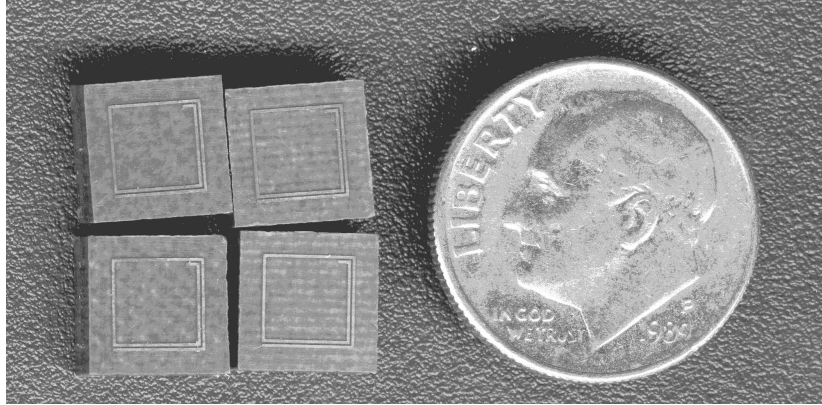


Figure 7.9: Embedded Circuit Metamaterial Resonators designed for a 2.0 GHz resonant frequency.

By these experimental results, the effectiveness of embedded-circuit metamaterial resonators predicted by theory and simulation is validated. In order to prove their usefulness to solving practical problems, an example application is considered in the next chapter.

7.5 Improving Isolation Bandwidth

Embedded circuit resonators are inherently narrow-band structures due to their resonant behavior. Two methods of increasing the isolation bandwidth are straightforward. In cases where the energy incident upon the insulators is already considered 'lost' energy, and absorber-like behavior is acceptable then the material Q-factor may be decreased by using a lossy host dielectric for the spiral or increasing the metal ohmic losses by using thinner or lower conductivity metals.

In the case that a low-Q insulator is not desirable, the spiral insulators can be stacked so that each isolation layer provides a slightly different isolation band. In a simulation experiment similar to that of Figure 7.3, the performance of insulator walls one and two layers thick are shown in Figure 7.13. For this experiment, the single spiral layer demonstrates a -10dB isolation bandwidth of 1.4%. By tuning



Figure 7.10: A physical experiment similar to the simulation of Fig. 7.6 for validating the effectiveness of metamaterial insulators.

the second spiral layer for a resonant frequency slightly higher than the first the two-layer insulator provides 4% -10dB isolation bandwidth. In this configuration the -5dB isolation bandwidths (2%) are added to achieve better than double the -10dB isolation bandwidth of a single layer.

7.6 Chapter Conclusions

The embedded-circuit metamaterial resonator has been shown to be an effective insulator. Despite its small size of only $0.03-0.05\lambda_0$, in the worst case it provided at least 20 dB of peak isolation and with a 10 dB isolation bandwidth of 1%. In the best case a single layer or metamaterial insulators provided as much as 40 dB isolation, with a 10 dB isolation over 6% bandwidth. Techniques were also presented for improving bandwidth to meet the specific bandwidth goals of a given application.

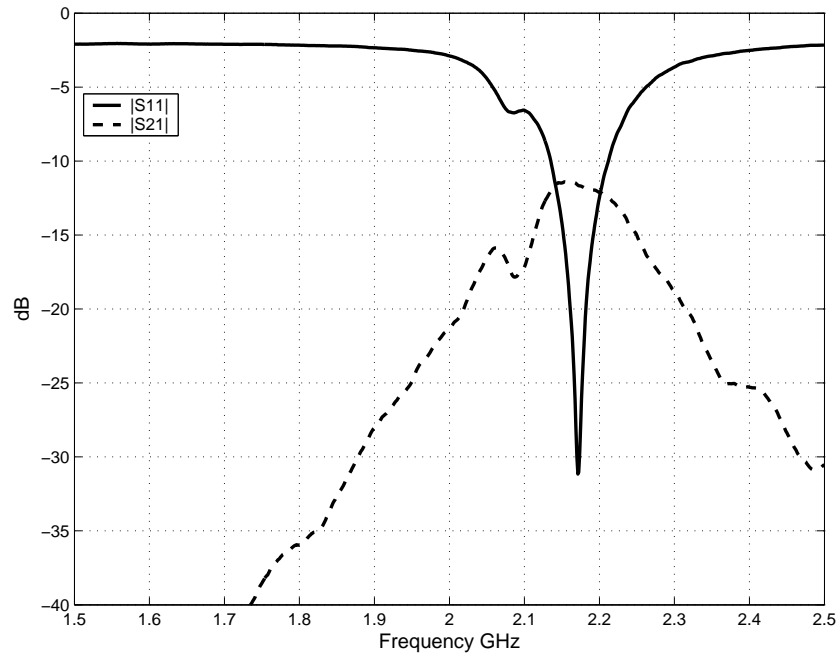


Figure 7.11: The input matching (S_{11}) and mutual coupling (S_{21}) of the two patches in Fig. 7.10 with metamaterial insulators removed, leaving an air-gap between substrates.

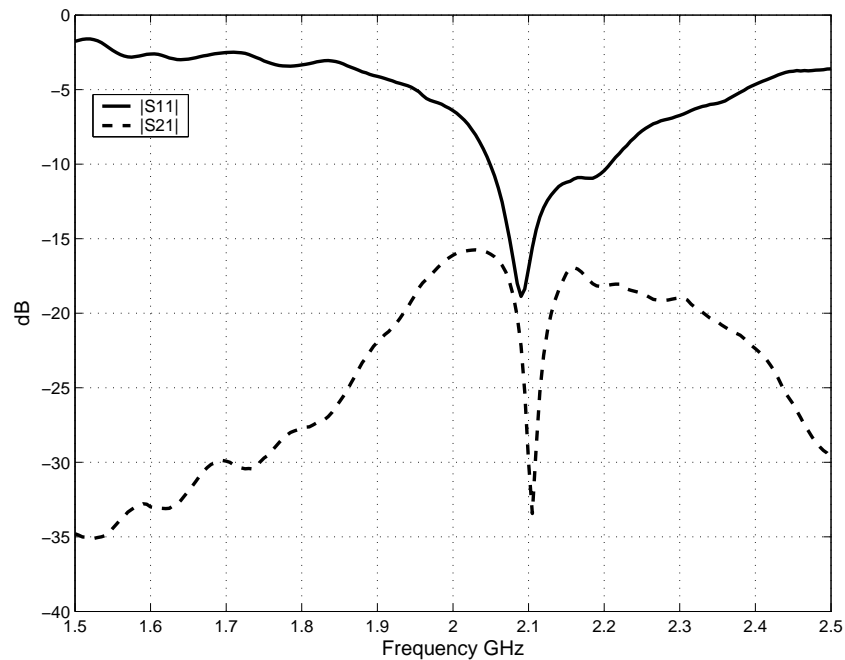


Figure 7.12: The input matching (S_{11}) and mutual coupling (S_{21}) of the two patches in Fig. 7.10 with metamaterial insulators. Even without tuning, the metamaterial insulators provide excellent suppression of mutual coupling.

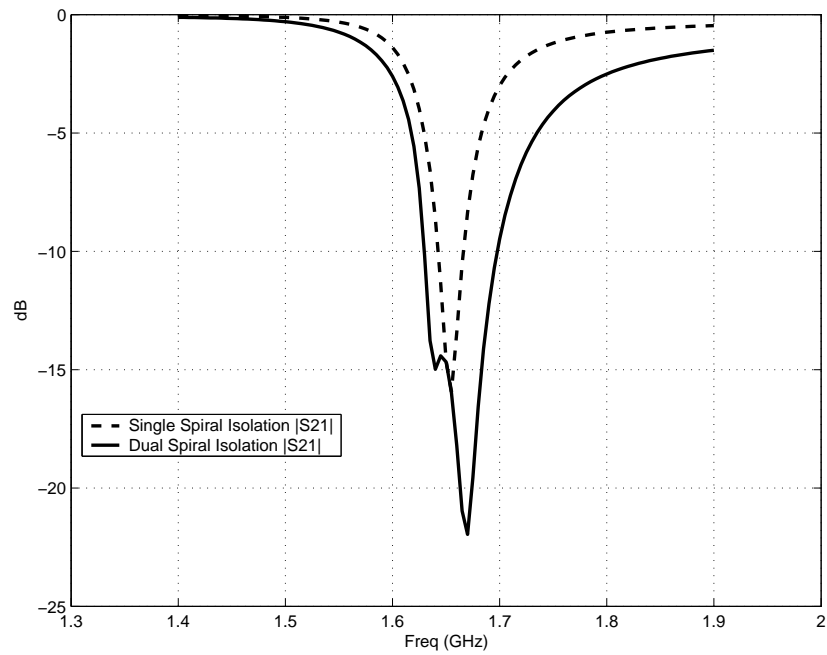


Figure 7.13: Typical insulation provided by an infinite wall of EC spirals. The -10dB isolation bandwidth is more than doubled by adding a second isolation layer tuned to a slightly different frequency.

CHAPTER 8

Metamaterial Insulator Enabled Superdirective Array

Nobody climbs mountains for scientific reasons. Science is used to raise money for the expeditions, but you really climb for the hell of it.

Edmund Hillary

8.1 Chapter Introduction

Metamaterial insulators provide effective isolation between microwave circuit elements such as densely packed antenna array elements. Mutual coupling between array elements is a major source of degradation in array performance and limits the practical packing density of arrays [50]. By decreasing the coupling between adjacent array elements, array element currents can be precisely controlled making advanced beam-forming and superdirectivity practical in densely packed physically small arrays. In this chapter metamaterial insulators are shown to be effective tools for achieving superdirectivity in physically small arrays.

8.2 Motivation and Background

Antenna performance is generally expected to be proportional to antenna size. Generally, physically larger antenna arrays exhibit superior performance characteristics such as high gain, beam-steering, anti-jamming null-steering and other advanced beam-forming compared to their smaller counterparts. It is the challenge of antenna miniaturization to provide these performance characteristics in physically smaller antennas.

For our purposes we propose that the problem of needing large arrays to achieve high performance is more properly considered as a problem of needing many array elements to achieve high performance, rather than needing large physical dimensions. From this perspective array performance is not a problem of total antenna size, but one of packing density.

In microstrip patch arrays, coupling between antenna elements increases with packing density [51]. Mutual coupling is a major source of degradation in array performance, causing distortion of the radiation pattern of the array and is the cause of scan blindness [52].

By controlling the current magnitude and phase on each array element, it is trivial to steer the beam maximum or a null in any chosen direction when mutual coupling can be reduced (that is, 'made negligible'). With a sufficient number of densely packed array elements, beams of arbitrarily high directivity and other complex pattern geometries such as beam and null steering can be achieved regardless of physical array size.

Beam-forming Application

Consider the application of a GPS receiving antenna. Normally the function for such an antenna would be to provide isotropic reception so as to receive signals from as many satellite sources as possible. Such a function can be easily served by a single

well-designed and physically small antenna. In the presence of a jamming source, the function of an intelligent GPS receiving antenna changes drastically. In the presence of a jammer, the array goal is to select the element magnitudes and phases to place an array-factor null in the direction of the jamming source, while retaining near isotropic reception in all other directions.

Suppressing mutual coupling eliminates many bothersome factors for dense arrays such as scan blindness and pattern degradation. In short, suppressing mutual coupling enables high performance in compact arrays.

8.2.1 Superdirectivity

A Superdirective antenna array is an antenna array with a directivity much greater than that of a reference antenna of the same size, usually a uniform array of the same length employing $\lambda_0/2$ element spacing. In a linear array superdirectivity is achieved by inserting more elements within a fixed length (decreasing the spacing) and alternating the sign of the excited currents for adjacent elements [42]. Increasing packing density in this manner leads eventually to the requirement of very large current magnitudes and rapid changes of phase in the excitation coefficients of adjacent array elements [53]. These conditions necessitate a very precise control of the excited currents. We show here that metamaterial insulators effectively isolate densely packed array elements, enabling precise control of excitation values and realizing superdirectivity in practical arrays [47].

While mathematically intriguing and long a popular topic of theoretical papers [54]-[55] close-packed, high gain arrays have generally been impractical for two reasons. Both reasons derive from the fact that to achieve superdirectivity, adjacent elements must be of alternating sign. Therefore the net effective current which produces radiation is quite low, yielding very little radiated power. Consequently, to achieve reasonable radiated power levels the excitation currents are quite high. This

causes the high current amplitudes to result in high ohmic losses for the relatively low level or radiated energy. This ohmic loss is the first reason that superdirective arrays are impractical. The low radiated power level despite high element current amplitudes also indicates a low radiation resistance- sometimes even lower than the ohmic resistances of the radiating elements for aggressively small arrays.

The second reason that superdirective arrays are impractical is because the portion of the current contributing to the net radiated field is quite low relative to the excitation currents, extremely high precision is required in controlling the element excitation current levels. This becomes impossible for closely packed elements due to mutual coupling. Even with perfect control of the excitation voltages at the antenna feed ports, the actual patch currents are strongly affected by the currents on adjacent elements. It is this coupling effect which Metamaterial insulators suppress.

8.2.2 Patch Coupling

A comprehensive study investigating the coupling between adjacent patch elements exists [51]. Except for very closely packed elements the coupling between patches in the E-plane (which decreases as $1/r$) is greater than in the H-plane (which decreases as $1/r^2$) [50]. The scattering matrix coupling level is shown here (Fig. 8.1) for patches aligned along the E-plane and H-planes at 2 GHz, on a thick (7.5mm) high dielectric ($\epsilon_r=15$) substrate. This E-plane geometry represents the element geometry we will be using for our array. This figure is useful in estimating acceptable packing density.

8.2.3 Sensitivity Factor

Due to mutual coupling the current on any radiating patch element in an array is a function not only of the power incident at the elements source port, but also of the currents on all adjacent patches. This condition greatly complicates array design for

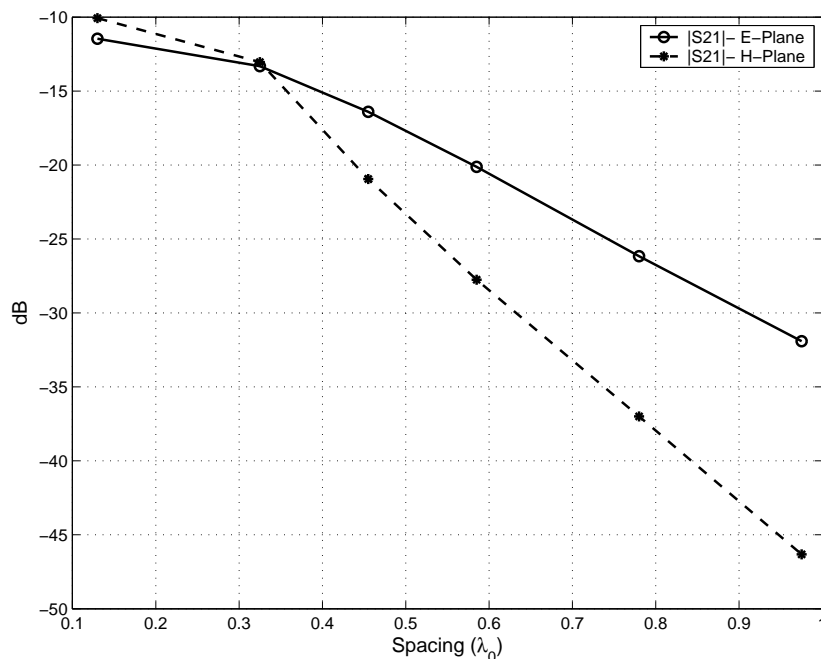


Figure 8.1: Coupling: Scattering parameter S21 measured at the feed ports of two patches in an E-plane orientated array, simulated for various spatial periods.

an array of non-uniform phase and in some extreme cases such as dense superdirective arrays can make it impossible to achieve the desired element currents.

A definition for the sensitivity of an N-element superdirective antenna array to perturbations in the excitation phase and magnitude is published [56]. It should be noted that the point of metamaterial insulators, or indeed any insulators, is not to decrease the sensitivity factor of a superdirective array, but instead to make it easier to achieve the superdirective excitation requirements for a given sensitivity. That is, it does not affect the allowable range of excitation current magnitudes and phases on the array elements, but instead makes it easier to achieve the desired excitation by providing coupling suppressing isolation between adjacent elements.

Metamaterials enable the design of individual array elements in isolation, without the consideration of mutual coupling effects. The previous alternative to this coupling suppression method was to solve and account for the mutual coupling effects either

analytically, which necessitates simple array elements such as monopoles or loops [[57] and [58]], or numerically for more complex array elements such as spirals [59]. It is forseen as a significant benefit to densely packed array design that metamaterial insulators enable the design of array elements without the need to account for mutual coupling effects.

8.2.4 Scan Blindness

Scan blindness is a condition where the *scan reflection coefficient* (Γ_s) is near or equal to unity magnitude for a given scan angle. In such a case, no real power can be delivered to the array. Scan blindness is an extreme case of scan loss, which occurs when $0 < \Gamma_s < 1$. For a linear array the scan reflection coefficient is defined by the scattering matrix of coupling coefficients and the array element excitation factors [50]

$$\Gamma_s = \sum_{n=1}^N S_{0n} \frac{A_n}{A_0}. \quad (8.1)$$

Here S_{0n} is the coupling coefficient between the "0" element, and element "n". The excitation coefficients (A_n and A_0) differ by the progressive scan phase between the two elements and may also differ in amplitude.

It is obvious to observe that if the scattering matrix coupling coefficients are suppressed, such as by the 20-30dB that can be obtained by the metamaterial insulators, the performance degrading effects of scan loss are mitigated.

For an excellent investigation of scan blindness in printed planar arrays, the interested reader is encouraged to see reference [52].

8.3 Design for Superdirective Beam-Forming

8.3.1 Single Element

A single patch situated between two isolation walls is the basic array element (Figure 8.2) for our linear E-plane array. Design and simulation on a typical desktop PC (1.8 GHz) was quite reasonable and achieved in four hours with commercially available FEM code (HFSS). For an aggressively miniaturized $0.11\lambda_0$ patch on a thick ($0.051\lambda_0$), low-loss dielectric substrate ($\epsilon_r=15$, $Tan\delta_e=2\times 10^{-4}$, 1.4 mil thick copper), better than 95% radiation efficiency was observed with a low directivity (near isotropic) frontal radiation pattern with just under 2% -10dB return loss impedance bandwidth. This simulation shows that for our application, the metamaterial insulator does not prohibitively degrade antenna efficiency.

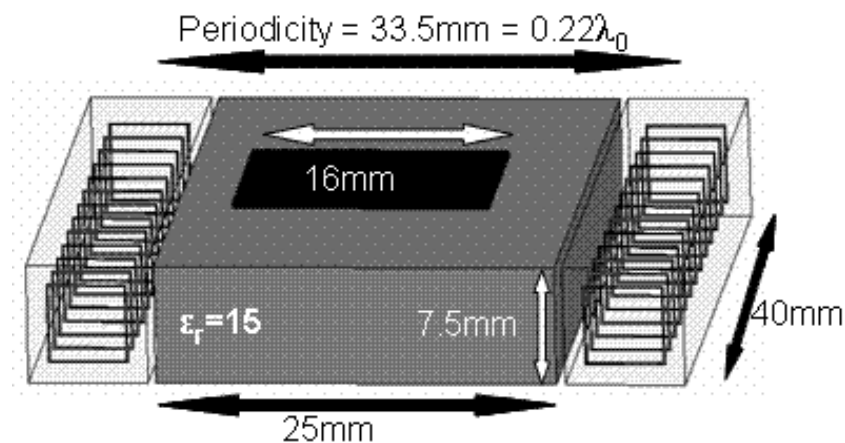


Figure 8.2: A patch antenna between metamaterial insulators is the basic antenna element which will be used to build a densely-packed antenna array. The insulators contain the energy in the local region, improving front-to-back ratio of the individual antenna and preventing mutual coupling in densely packed arrays.

8.3.2 Linear Array

With metamaterial insulators suppressing coupling between array elements, physically small arrays can provide impressive beam-forming. Before fabricating a densely packed five-element physical array, simulations were performed to predict performance.

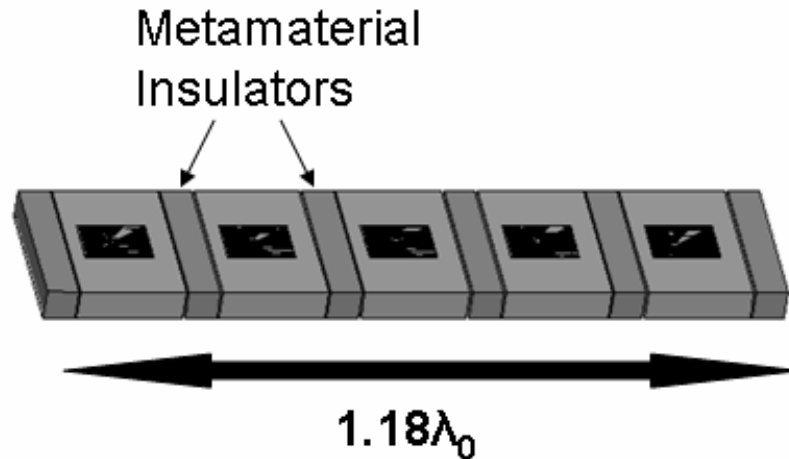


Figure 8.3: A densely packed five element linear patch array $1.18\lambda_0$ with metamaterial insulators to suppress mutual coupling

A single Isolation wall in the array elements of Figure 7.6 and Figure 8.3 incorporates thirteen embedded circuit isolators. Modeling the the spiral resonator involves modeling a very fine feature size, with traces and gap size of only 5mils ($0.007\lambda_0$). To simulate the the metamaterial isolation performance in the array of Figure 8.3 requires the modeling of 78 spiral resonators in an array with a total structure size 1800 times that of the smallest feature size. For arrays, such simulation complexity quickly becomes unmanageable for HFSS. To simplify simulation complexity the polarization dependant equivalent permittivity and permeability of the isolation walls were determined according to the models used to generate Figure 7.2. Blocks with these effective material properties may be used to represent isolation walls, making simulation of larger arrays possible. A five-element array with a total length of $1.18\lambda_0$

was simulated in HFSS using this equivalent material to represent the isolation walls (Figure 8.3).

Simulations indicate that under uniform excitation conditions our array exhibits gain of +6dBi, 142 degree first-null beamwidth and 81% radiation efficiency. This is an important indicator of the impact metamaterial insulators have on the overall array system loss and efficiency. Next we compare the performance of our array to an ideal linear array of five ideal isotropic radiators. Such an ideal array would generate a pattern with a first-null beamwidth of 133 degrees. This is the reference array relative to which superdirectivity is defined. As is predictable, under uniform non-superdirective excitation conditions our five element patch design behaves comparably to this reference array. If the excitation coefficients of our array are then adjusted to achieve a superdirective pattern, a squinted beam with a 65 degree beamwidth and -9.5 dB side-lobe level is achievable (Fig. 8.4).

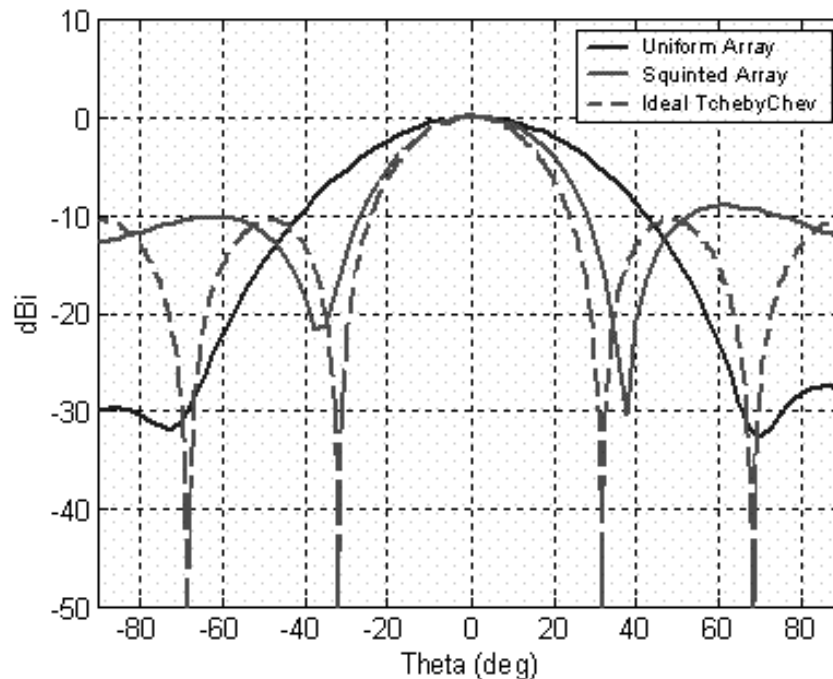


Figure 8.4: The calculated E-field pattern of the array in Fig. 8.3 under uniform excitation and a squinted (superdirective) beam. The response of an ideal 5-element array of isotropic radiators of the same geometry is included for reference

As shown in Fig. 8.4, this squinted pattern is a very close match to the ideal 61 degree beamwidth achievable by a Chebychev array for the same side-lobe level. The same element non-ideality which causes our array to exhibit 142 degree beam-width instead of the ideal 133 degree beamwidth is likely the cause of this non-ideality as well. To understand the reason for this, consider the requirements for an ideal array performance. For the array factor to apply perfectly and predict the overall array pattern, the array elements must be ideal isotropic point-sources [42]. That the array elements are not isotropic radiators is accounted for in the element factor, but the fact that the patch and insulators are not point-sources is not accounted for.

The majority of energy radiated by the antenna element of figure 8.2 is radiated at the edges of the patch itself, which are themselves spatially distributed. Additionally, some portion of the energy incident upon the insulation walls is scatters into the radiating far-field, further spatially distributing the energy in a non-point-source fashion. Therefore, the ideal array factor equation does not apply perfectly, but as we shall show, they are still excellent approximations for predicting array performance.

An ideal Dolf-Chebychev array represents the optimum achievable beamwidth versus sidelobe level trade-off. In figure 8.5 the side-lobe level and first-null beamwidth of an ideal Dolf-Chebychev array is compared with several simulated cases of array excitations for our metamaterial insulated array. Although the ideal performance can not be achieved, the metamaterial insulated array approaches the ideal performance.

As is always the case for all arrays, a beam steered off broadside in a metamaterial insulated array experiences beam widening and simulation validates this. The benefit derived from the metamaterial insulators is that by dramatically reducing mutual coupling, a much narrower beam is achieved than would be possible by an array of the same length composed of elements with the more traditional Nyquist spacing. Additionally, since mutual coupling is suppressed, the adverse effects of mutual coupling such as scan blindness are also prevented.

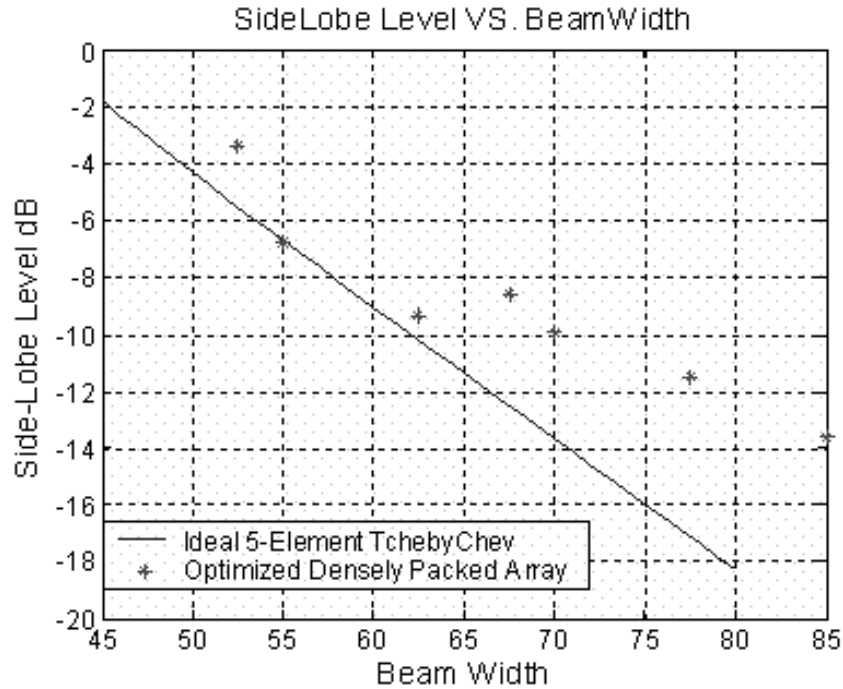


Figure 8.5: The lowest possible SideLobe Level for a given (first null) beamwidth is plotted as the solid line. Several optimized sidelobe levels for a given beamwidth achievable for our metamaterial insulator enabled array is indicated for several beamwidths

Anti-jamming null steering with a near-isotropic frontal pattern was previously discussed. To illustrate the benefits that metamaterial insulators provide towards this end, consider figures 8.6 and 8.7. In figure 8.6 a null is placed at broadside, exhibiting $> 10\text{dB}$ suppression 20 degrees wide. When the null is moved off-broadside as in Fig. 8.7, perhaps to suppress a jamming signal, a receiving pattern within 1 dB of isotropic is achievable in the entire opposing hemisphere of the array front. This is an optimal performance for suppressing a single jamming source.

Lastly, we consider the case of the minimum separation between the desired target and a jamming source. Even with an array only $1.18\lambda_0$ long, metamaterial insulators enable a broadside beam null-to-maximum separation of as little as 25 degrees.

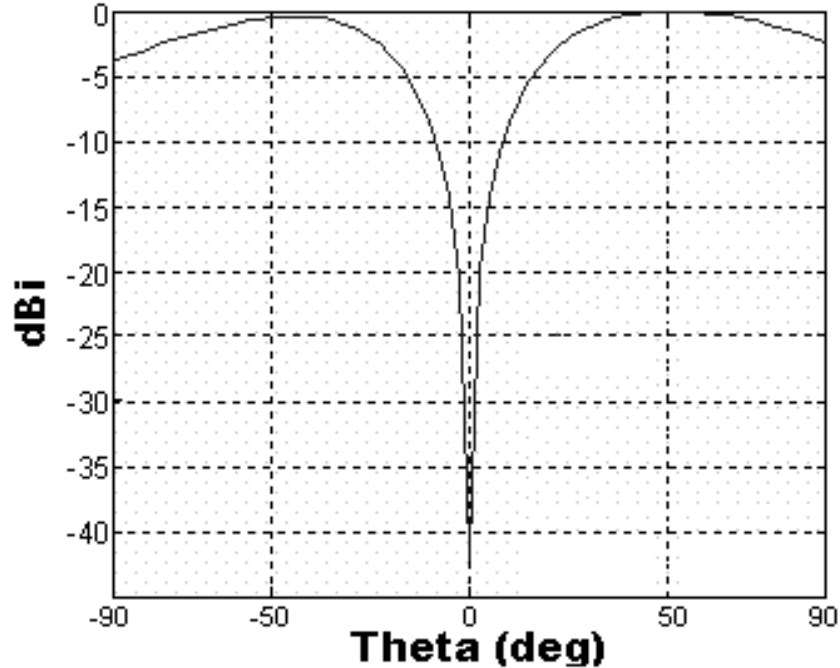


Figure 8.6: Simulations of Anti-Jamming null placement directly at broadside can readily provide 40 dB nulls, with -10dB jamming suppression across a 20 degree beamwidth. Reception in the remainder of the array field of view remains good.

8.4 Array Measurement

To validate the simulations, a single superdirective array and feed network was fabricated and measured (Figure 8.8). The array feed network was fabricated on commercially available Rogers RT/Duroid 5880 ($\epsilon_r=2.2$, $\text{Tan}\delta=0.0009$, Thickness=0.031”) using popular N-way power divider techniques implemented with microstrip transmission lines[[60] and [61]]. The power division was achieved by three such power dividers (One 3-way, and two 2-way), and phase control was achieved with meandering phase delay transmission lines. The array element $0.11\lambda_0$ patches were etched from 1.4 mil thick copper on a thick ($0.051\lambda_0$), low-loss dielectric substrate ($\epsilon_r=15$, $\text{Tan}\delta_e=2\times 10^{-4}$) which was provided custom by the TransTech corporation.

This array, with a superdirective broadside beam was designed to provide 65 degree beamwidth and +10.7 dBi directivity. Upon fabrication, the measured performance

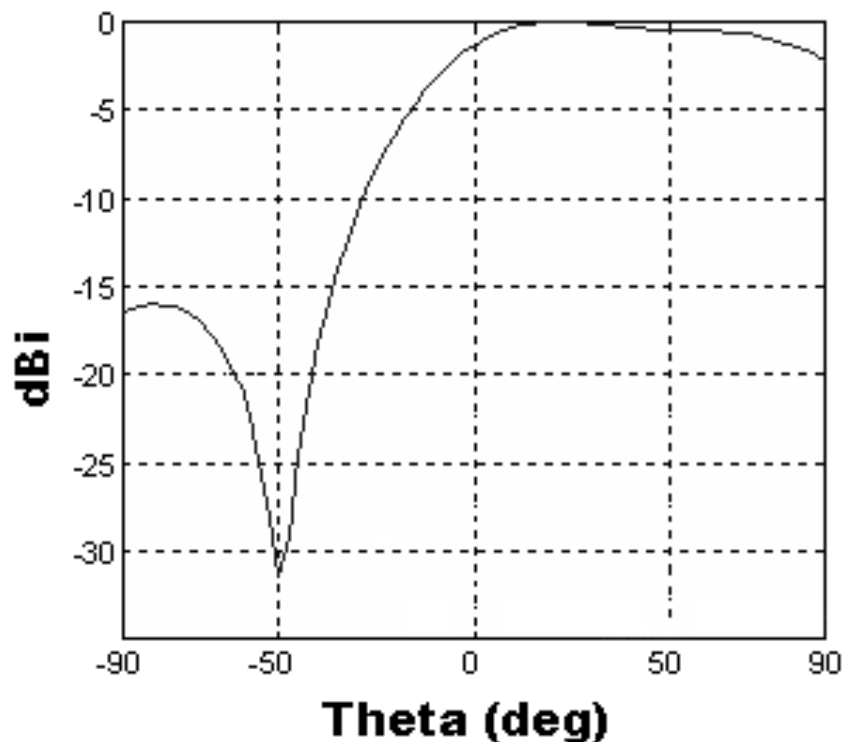


Figure 8.7: The anti-jamming null can be steered to any angle while maintaining an excellent near-isotropic reception pattern in the alternate hemisphere of the antenna field of view

was found to be 75 degree beamwidth and +9.6 dB of Directivity. As shown in figure 8.9, the measured pattern of the array main-beam is very close to the designed array.

8.4.1 Comment on the choice of excitation coefficients

Although the radiating elements are effectively isolated from each other, the isolation wall itself interacts with the trapped substrate surface waves. A portion of this scattered energy is directed broadside and this scattering affects the far-field pattern. This scattered energy must be accounted for in the choice of excitation coefficients. For this reason, a simple and direct implementation of the Dolf-Chebyshev polynomials or similar array factor optimization technique is not satisfactory. Instead, once the complex far-field array pattern response to unitary magnitude and normalized phase excitation at each of the individual array input ports has been identified by

HFSS simulation, the optimal excitation coefficient for the individual array elements must be determined to achieve the desired far-field pattern. The initial guess for the element excitations may be selected by the ideal Dolf-Chebyshev coefficients. System linearity is employed to predict the complex far-field pattern from the port excitations and numerical algorithms based on computationally fast gradient methods are usable to tune the array excitation coefficients to the optimal for the metamaterial insulated array. The predicted far-field pattern for the excitation coefficients selected by this technique proves to be exactly the same as that simulated in HFSS for the same coefficients. This is the mechanism which has been employed here to determine the squinted and steered beam patterns.

8.5 Limits of Superdirectivity

Many excellent papers already exist describing the limits of small antennas, and the interested reader is directed to the literature [62]. The three fundamental limits of electrically small antennas are that they experience high ohmic losses (low efficiency), that they require high precision in their current magnitudes and phase (high sensitivity), and that they are narrow bandwidth due to a high Q-factor. Briefly, the reason for the high Q-factor of superdirective arrays is that they alternating signs of excitation currents creates a strong reactive stored energy around the antenna relative to the radiated field resulting in a very high antenna Q-factor.

Since $Q \propto \frac{1}{\text{Bandwidth}}$ and array Q varies exponentially with directivity, superdirective arrays are expected to have a narrow bandwidth [62].

8.5.1 Efficiency

The superdirective array which was fabricated and measured is shown in Fig. 8.9 exhibited 24% radiation efficiency. The primary source of the efficiency loss in this

array is the ohmic and dielectric losses on the patches themselves. To understand this, we must consider the radiated field at broadside. At the beam maximum, a net effective radiating current equal to $\sum_{n=1}^N I_n$ is observed. Due to the alternation of sign on adjacent patches, the current magnitudes in our array are 10 times that for a uniform array with an equivalent net effective radiating current. Therefore, the ohmic and dielectric losses, which normally create approximately a 10% loss in efficiency are in this case 10 times higher. This is a well established and well understood limitation of Superdirective arrays [62]. There are various techniques for addressing these ohmic losses discussed, including superconducting antennas which result in near 100% antenna efficiency [[55],[57] and [63]] and judicious choice of array function excitation coefficients in dipole and loop arrays which yield up to 20-30% efficiency without superconductors [[57], [64], and [65]] although extremely low efficiencies around 1% or even much less are common without such compensations [[58], [63], and [65]]. This 20-30% efficiency range achieved by small non-superconducting arrays $0.5-2.0\lambda_0$ long (3-11 elements), is the most reasonable direct-comparison of efficiency for our measured efficiency of 24%.

There are three important indications of the acceptable effect of insulators on the overall system efficiency. The first is that in 7.3 we saw that for a plane wave incident on a wall of insulators, about 80% the energy is reflected back. Secondly the the single-patch antenna between of figure 8.2 which serves as our array element also exhibits better than 95% efficiency despite being between two rows of insulators. Thirdly, according to simulations our five-element array should deliver 81% efficiency if operated in a uniform excitation mode. Considering this evidence, it appears likely that approximately 10-20% of the overall efficiency loss of the system is due to the metamaterial insulators, and the remainder of the inefficiency is due to the ohmic losses common to all superdirective arrays.

8.6 Chapter Conclusions

A physically small five-element patch array only $1.18\lambda_0$ long demonstrated superdirectivity, and beam-forming with beam-steering and anti-jamming null-steering. This experiment shows that metamaterial insulators are effective tools in the design of compact arrays.



Figure 8.8: $1.18\lambda_0$ five-element metamaterial enabled patch array for 2GHz operation

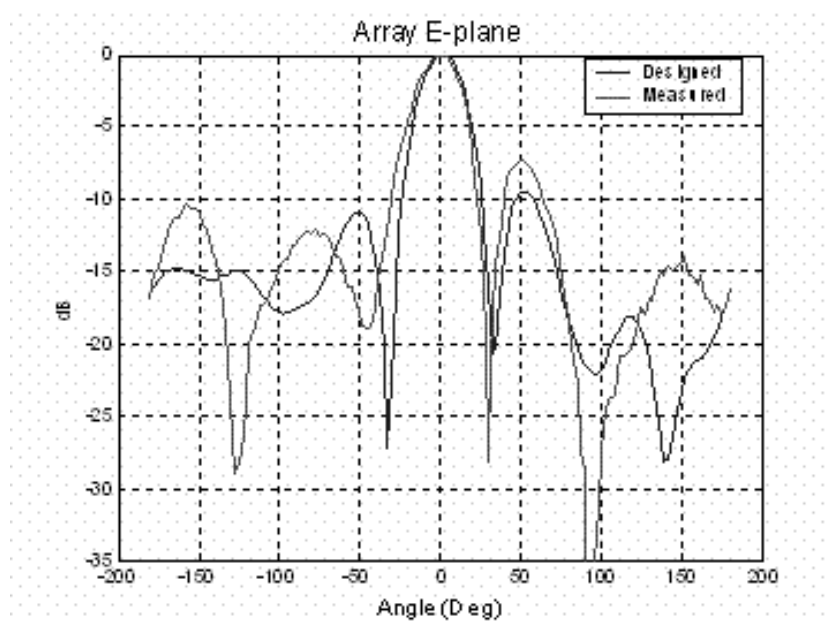


Figure 8.9: The broadside main-beam exhibits superdirectivity at 2.12GHz. Although the antennas and feed network were design for 2.0 GHz, metamaterial insulators resonated at 2.1GHz, so the array was measured untuned in the insulating region at 2.12GHz.

CHAPTER 9

Conclusion

An incremental contribution to the existing body of knowledge.

Kevin Buell

9.1 Summary of Results

Several advances to the existing state of the art have been developed and presented including the development of new materials, new material characterization methods, and new antenna systems not previously available to the field of engineering.

Chapter 2

The limits of pre-existing magnetic materials for microwave applications were investigated and in joint research with the Trans-Tech corporation we were able to provide a new, impedance matched Z-phase hexaferrite ceramic for moderate loss application up to about 400 MHz.

Chapter 3

A new form of metamaterial, the embedded circuit spiral resonator, was developed. A theoretical model describing the metamaterial operation and offering a means of

predicting material properties was advanced. The design process for this new material outlined here yields good predictability in the material performance. The embedded circuit spiral resonator achieved enhancement of electrical permittivity and magnetic permeability. Also of significant value is the negative permeability operating region of the embedded circuit spiral resonator which provides insulating properties, blocking the transmission of electromagnetic energy.

Chapter 4

Microwave characterization methods for magnetic materials were investigated and new techniques were developed. The frequency extended perturbation method is a resonant cavity based method requiring very little computational effort and providing characterization of dielectric or permeable materials over about a 15% bandwidth. The hybrid measurement technique is computationally intensive due to numerical simulation requirements, but this new technique provides accurate measurement of the material loss factors of microwave materials exhibiting both unknown electric and magnetic loss factors.

Chapter 5

A metamaterial substrate was shown to provide a frequency tunable miniaturization factor for planar patch antennas. This experiment validated the effectiveness of metamaterials in providing both permeability and permittivity enhancement, as well as validate the permeability and permittivity predicted by our analytical models presented in chapter 3. Although the metamaterial substrate performed as expected, the measured radiation efficiency of under 40% is too low for most applications.

Chapter 6

By selectively tuning the geometric parameters of a reactive impedance surface (RIS), we were able to achieve an optimal interaction between the RIS and a nearby radiating source element. An aggressively miniaturized patch antenna was designed, fabricated, and measured using this technique and this antenna provided performance which is to our knowledge the highest reported gain and bandwidth for such a small planar antenna.

Chapter 7

The embedded-circuit spiral resonator metamaterial provides excellent insulator performance despite its small size. The primary application investigated was providing isolation between adjacent regions of planar microstrip circuits. In the best case a single layer of metamaterial insulators $0.03\lambda_0$ thick provided 40dB peak isolation, with a 10 dB isolation over 6% bandwidth. Techniques were investigated and presented for increasing bandwidth to meet wider bandwidth goals.

Chapter 8

By employing metamaterial insulators the coupling between adjacent elements in a densely packed array of microstrip patch antennas is dramatically reduced. By reducing the coupling by over 20 dB, precise individual element excitation control is enabled even for densely packed arrays. This development resolves one of the major limiting factors for small superdirective arrays. A small linear superdirective array was designed, fabricated and measured using this insulator technology, validating the effectiveness of embedded circuit spiral resonator metamaterial insulators.

9.2 Future Work

None of the research described herein is the last word on any subject. Currently a great deal of attention is being focused on research in the area of these newly christened 'metamaterials', but in a generation the interest in this topic will likely have waned and the scientific community as a whole will have selected a few small morsels of utility and insight from our current pursuits. When that day comes, I would be very pleased to have one small piece of my work to be one of the pieces to have proven itself useful. Yet, I hold no such unrealistic expectations.

9.3 Closing Thoughts

A doctoral thesis is the result of several years of research dedicated to producing a significant and original contribution to the field of knowledge. More important than the new knowledge that my research has been able to discover and contribute to the world, is what the world has been able to teach me during the course of this research.

A human being should be able to change a diaper, plan an invasion, butcher a hog, conn a ship, design a building, write a sonnet, balance accounts, build a wall, set a bone, comfort the dying, take orders, give orders, cooperate, act alone, solve equations, analyze a new problem, pitch manure, program a computer, cook a tasty meal, fight efficiently, die gallantly. Specialization is for insects.

Robert Heinlein

APPENDIX

APPENDIX

Published Work

CONFERENCE PAPERS

[Best Student Paper: Contest Finalist]

K. Buell, K. Sarabandi "A Method of Characterizing Complex Permittivity and Permeability of Meta-Materials" Antennas and Propagation Society International Symposium, 2002. IEEE ,Volume: 2 , 16-21 June 2002 Pages:408 - 411 vol.2

Sarabandi, K.; Brown, C.G.; Pierce, L.; Zahn, D.; Azadegan, R.; Buell, K.; Casciato, M.; Koh, I.; Lawrence, D.; Park, M. "Calibration and validation of the Shuttle Radar Topography Mission height data for southeastern Michigan" Geoscience and Remote Sensing Symposium, 2002. IGARSS '02. 2002 IEEE International ,Volume: 1 , 24-28 June 2002 Pages:167 - 169 vol.1

K.Buell, K. Sarabandi "Measurement of Meta-Materials Utilizing Resonant Embedded-Circuit For Artificial Permeability By Frequency Extended Perturbation Method" Union of Radio Sciences International (URSI) Symposium, Columbus, Ohio, June 22-27, 2003.

[Best Student Paper: Contest Winner]

K. Buell, D. Cruickshank, H. Mosallaei, K. Sarabandi " Patch Antenna over RIS Substrate: A Novel Miniaturized Wideband Planar Antenna Design" IEEE AP-S International Symposium, Columbus, Ohio, June 22-27, 2003. Pages:269 - 272 vol.4

Buell, K.; Mosallaei, H.; Sarabandi, K. "Embedded-circuit magnetic metamaterial substrate performance for patch antennas" Antennas and Propagation Society Symposium, 2004. IEEE ,Volume: 2 , 20-25 June 2004 Pages:1415 - 1418 Vol.2

Buell, K.; Mosallaei, H.; Sarabandi, K. "Ferroelectrics for Broadband Miniaturization" Union of Radio Sciences International (URSI) Symposium, 2004. 20-25 June 2004

[Best Student Paper: Contest Winner]

Buell, K.; Mosallaei, H.; Sarabandi, K. "Electromagnetic MetaMaterial Insulator To Eliminate Substrate Surface Waves" Antennas and Propagation Society Symposium, July 2005.

[Best Student Paper: Contest Finalist]

Buell, K.; Mosallaei, H.; Sarabandi, K. "Superdirective Array Beam Forming with Metamaterial Insulators" Antennas Applications Symposium, September 2005.

JOURNAL PAPERS

K. Buell, H. Mosallaei, K. Sarabandi "A Substrate for Small Patch Antennas Providing Tunable Miniaturization Factors" submitted (Oct 2004), accepted, and awaiting publication in the journal of the Transactions of the IEEE Microwave Theory and Techniques Society

K. Buell, K. Sarabandi "A Novel Hybrid Method of Characterizing Complex Permittivity and Permeability" work in progress for submission to journal of the IEEE Antennas and Propagation Society

K. Buell, H. Mosallaei, K. Sarabandi "Magnetic MetaMaterials for Isolation of Dense Planar Antenna Arrays" Submitted for publication to journal of the IEEE Antennas and Propagation Society- September 2005

BIBLIOGRAPHY

BIBLIOGRAPHY

- [1] J. Pendry, A. Holden, D. Robbins, and W. Stewart, "Magnetism from conductors and enhanced nonlinear phenomena," *IEEE Transactions on Microwave Theory and Techniques*, vol. 47, pp. 2075–2084, Nov 1999.
- [2] W. D. Callister, Jr, *Materials Science And Engineering: An Introduction*. New York: John Wiley & Sons, Inc, 2000, ch. 21.
- [3] K. Buell, H. Mosallaei, and K. Sarabandi, "Measurement of meta-materials utilizing resonant embedded-circuit for artificial permeability by frequency extended perturbation method," *URSI*, JUN 2003.
- [4] M. Sadoun and N. Engheta, "Theoretical study of electromagnetic properties of non-local 'omega' media," *Progress In Electromagnetic Research (PIER) Monograph Series, Vol. 9*, pp. 351–397, 1994.
- [5] N. Engheta, "Electromagnetics of complex media and metamaterials," *International Conference on Mathematical Methods in Electromagnetic Theory*, vol. 1, pp. 175–180, 2002.
- [6] R. Ziolkowski, "Double negative metamaterial design, experiments, and applications," *IEEE Antennas and Propagation Society International Symposium*, vol. 2, pp. 396–399, Jun 2002.
- [7] S. Suh, W. Stutzman, and W. Davis, "Low-profile, dual polarized broadband antennas," *IEEE Antennas and Propagation Society International Symposium Digest*, vol. 2, pp. 256–259, Jun 2003.
- [8] J. Brown, "Artificial dielectrics having refractive indices less than unity," *Proc. IEEE Monograph no. 62R Pt. 4*, vol. 100, pp. 51–62, 1953.
- [9] J. Brown and W. Jackson, "The properties of artificial dielectrics at centimeter wavelengths," *Proc. IEEE paper no. 1699R*, vol. 102B, pp. 11–21, 1955.
- [10] J. Seeley and J. Brown, "The use of artificial dielectrics in a beam scanning prism," *Proc. IEEE, paper no. 2735R*, no. 105C, pp. 93–102, 1958.
- [11] J. Seeley, "The quarter-wave matching of dispersive materials," *Proc. IEEE, paper no. 2736R*, no. 105C, pp. 103–106, 1958.

- [12] A. Carne and J. Brown, "Theory of reflections from the rodded-type artificial dielectrics," *Proc. IEEE*, paper no. 2742R, no. 105C, pp. 107–115, 1958.
- [13] W. Rotman, "Plasma simulation by artificial dielectrics and parallel-plate media," *IEEE Trans. Antennas Propag*, vol. 10, pp. 82–95, 1962.
- [14] D. Smith, P. Rye, D. Vier, A. Starr, J. Mock, and T. Perram, "Design and measurement of anisotropic metamaterials that exhibit negative refraction," *IEICE Trans. Electron.*, vol. E87-C, no. 3, pp. 359–370, Mar 2004.
- [15] J. Pendry, A. Holden, W. Stewart, and L. Youngs, "Extremely low frequency plasmons in metallic mesostructures," *Phys. Rev. Lett.*, vol. 76, p. 4773, 1996.
- [16] G. Veselago, V., "The electrodynamic of substances with simultaneously negative values of ϵ and μ ," *Soviet Physics Uspekha*, vol. 10, pp. 509–514, Jan./Feb. 1968.
- [17] D. Kern and D. Werner, "The synthesis of metamaterial ferrites for rf applications using electromagnetic bandgap structures," *IEEE Antennas and Propagation Society International Conference*, vol. 1, pp. 497–500, June 2003.
- [18] K. Aydin, K. Mayindir, and E. Ozbay, "Microwave transmission through metamaterials in free space," *Quantum Electronics and Laser Science Conference*, p. 12, May 2002.
- [19] R. Ziolkowski, "Design, fabrication, and testing of double negative metamaterials," *IEEE Transactions on Antennas and Propagation*, vol. 51, pp. 1516–1529, July 2003.
- [20] J. Pendry, "Negative refraction makes a perfect lens," *Physical Review Letters*, vol. 85, no. 18, pp. 3966–3969, Oct 2000.
- [21] R. Ruppin, "Extinction properties of a sphere with negative permittivity and permeability," *Solid State Communications*, no. 116, pp. 411–415, 2000.
- [22] A. Lakhtakia, "On perfect lenses and nihility," *International Journal of Infrared and Millimeter Waves*, vol. 23, no. 3, pp. 339–343, Mar 2002.
- [23] N. Fang and X. Zhang, "Imaging properties of a metamaterial superlens," *Applied Physics Letters*, vol. 82, no. 2, pp. 161–163, Jan 2003.
- [24] A. Grbic and G. Eleftheriades, "A backward-wave antenna based on negative refractive index l-c networks," *IEEE Antennas and Propagation Society International Symposium*, vol. 4, pp. 340–343, June 2002.
- [25] K. Sarabandi and H. Mosallaei, "Electro-ferromagnetic tunable permeability, band-gap and bi-anisotropic meta-materials utilizing embedded circuits," *IEEE AP-S International Symposium Digest*, June 2003.
- [26] D. Pozar, *Microwave Engineering: Second Edition*.

- [27] H. Mosallaei and K. Sarabandi, "Magneto-dielectrics in electromagnetics: Concept and applications," *IEEE Transactions on Antennas and Propagation*, vol. 52, no. 6, Jun 2004.
- [28] N. Panoiu and R. Osgood, "Feasibility of fabricating metamaterials with negative refractive index in the visible spectrum," *Conference on Lasers and Electro-Optics*, vol. 1, pp. 241–242, May 2002.
- [29] K. Buell, H. Mosallaei, and K. Sarabandi, "Embedded-circuit magnetic metamaterial substrate performance for patch antennas," *IEEE Antennas and Propagation Symposium, AP-S. Digest*, vol. 2, pp. 1415–1418, 2005.
- [30] K. Sarabandi and H. Mosallaei, "Design and characterization of a metamaterial with both e-m parameters realized utilizing embedded-circuit artificial molecules," *IEEE Transactions on Antennas and Propagation*, Submitted for Publication Dec 2004.
- [31] A. Nicolson and G. Ross, "Measurement of intrinsic properties of materials by time domain techniques," *IEEE Transactions on Instrumentation and Measurement*, vol. IM-19, pp. 377–382, Nov 1970.
- [32] J. Baker-Jarvis, E. Vanzura, and W. Kissick, "Improved technique for determining complex permittivity with the transmission/reflection method," *IEEE Transaction on Microwave Theory and Techniques*, vol. 38, pp. 1096–1103, Aug 1990.
- [33] A. Boughriet, C. Legrand, and A. Chapoton, "Noniterative stable transmission/reflection method for low-loss material complex permittivity determination," *IEEE Transactions on Microwave Theory and Techniques*, vol. 45, pp. 52–57, Jan 1997.
- [34] W. Weir, "Automatic measurement of complex dielectric constant and permeability at microwave frequencies," *Proceedings of the IEEE*, vol. 62, pp. 33–36, Jan 1974.
- [35] *Agilent 85070E Dielectric Probe Kit 200 MHz to 50 GHz, Technical Overview*. Agilent Technology, 2003.
- [36] R. F. Harrington, *Time-Harmonic Electromagnetic Fields*. New York: McGraw Hill, 1961, ch. 7.
- [37] B. Meng, J. Booske, and R. Cooper, "Extended cavity perturbation technique to determine the complex permittivity of dielectric materials," *IEEE Trans. Microwave Theory Tech*, vol. 43, pp. 2633–2636, Nov 1995.
- [38] J. Baker-Jarvis, R. Geyer, J. G. jr, M. Janezic, C. Jones, B. Riddle, C. Weil, and J. Krupka, "Dielectric characterization of low-loss materials, a comparison of techniques," *IEEE Trans. Dielectrics and Elect. Insulation*, vol. 5, pp. 571–577, 1998.

- [39] J. Krupka and R. Geyer, “Complex permeability of demagnetized microwave ferrites near and above gyromagnetic resonance,” *IEEE Transactions on Magnetics*, vol. 32, no. 3, pp. 1924–1933, May 1996.
- [40] J. Krupka, P. Blondy, D. Cros, P. Guillon, and R. Geyer, “Whispering-gallery modes and permeability tensor measurements in magnetized ferrite resonators,” *IEEE Transactions on Microwave Theory and Techniques*, vol. 44, pp. 1097–1102, Jul 1996.
- [41] D. Kajfez, S. Chebolu, M. Abdul-faffoor, and A. Kishk, “Uncertainty analysis of the transmission-type measurement of q-factor,” *IEEE Transactions on Microwave Theory and Techniques*, vol. 47, no. 3, pp. 367–371, Mar 1999.
- [42] A. Balanis, C., *Antenna Theory Analysis and Design*. New York: John Wiley & Sons, Inc, 1997, ch. 99, pp. 306–309.
- [43] J. McVay, A. Hoorfar, and N. Engheta, “Radiation characteristics of microstrip dipole antennas over a high-impedance metamaterial surface made of hilbert inclusions,” *IEEE MTT-S International Microwave Symposium Digest*, vol. 1, pp. 587–590, June 2003.
- [44] J. Colbum and Y. Rahmat-Samii, “Patch antennas on externally perforated high dielectric constant substrates,” *IEEE Trans. Antennas Propagat.*, vol. 41, no. 12, Dec 1999.
- [45] H. Mosallaei and Y. Rahmat-Samii, “Broadband characterization of complex periodic ebg structures: An fdtd/prony technique based on the split-field approach,” *Electromagnetics J.*, vol. 23, no. 2, Jan-Feb 2003.
- [46] H. Mosallaei and K. Sarabandi, “A novel artificial reactive impedance surface (ris) for miniaturized wideband planar antenna design: Concept and characterization,” *Antennas and Propagation Society International Symposium*, 2003.
- [47] K. Buell, H. Mosallaei, and K. Sarabandi, “Electromagnetic metamaterial insulator to eliminate substrate surface waves,” *IEEE Antennas and Propagation Symposium, AP-S. Digest*, 2005.
- [48] —, “Superdirective array beam forming with metamaterial insulators,” *Antennas Applications Symposium Digest*, 2005.
- [49] —, “A substrate for small patch antennas providing tunable miniaturization factors,” *IEEE Transactions on Microwave Theory and Techniques*, An article submitted for publication.
- [50] R. C. Hansen, *Phased Array Antennas*. New York: John Wiley & Sons, Inc, 1998, ch. 7.

- [51] A. H. Mohammadian, N. Martin, and D. Griffin, "A theoretical and experimental study of mutual coupling in microstrip antenna arrays," *Trans of the IEEE Antennas And Propagation Society*, vol. AP-37, pp. 1217–1223, Oct 1989.
- [52] D. M. Pozar and D. Schaubert, "Scan blindness in infinite phased arrays of printed dipoles," *Trans of the IEEE Antennas And Propagation Society*, vol. AP-32, pp. 602–610, June 1984.
- [53] O. Ishii, K. Itoh, Y. Nagai, and K. Kagoshima, "Miniaturization of array antennas with superdirective excitation," *IEEE Antennas and Propagation Symposium, AP-S. Digest*, vol. 3, pp. 1850–1853, 1993.
- [54] C. Dolph, "A current distribution for broadside array which optimizes the relationship between beamwidth and sidelobe level," *Proceedings of the IRE*, vol. 34, no. 6, 1946.
- [55] A. B. Bloch, R. Medhurst, S. Pool, and W. Knock, "Superdirectivity," *Proceedings of the IEE*, vol. 48, p. 1164, 1960.
- [56] E. H. Newman, J. H. Richmond, and C. H. Walter, "Superdirective receiving arrays," *IEEE Transactions on Antennas and Propagation*, vol. 26, no. 5, pp. 638–639, 1965.
- [57] G. Cook and S. K. D. Bowling, "Improving efficiencies of superdirective arrays of monopoles over lossy groundplanes by using superconducting disc overlays," *IEE Proceedings on Microwave Antenna Propagation*, vol. 142, no. 6, 1995.
- [58] D. Bowling, D. Banks, D. Kinman, A. Martin, R. Dinger, R. Forse, and G. Cook, "A three-element, superdirective array of electrically small, high-temperature superconducting half-loops at 500-mhz," *IEEE Antennas and Propagation Symposium, AP-S. Digest*, vol. 3, pp. 1846–1849, 1993.
- [59] R. Waldron and G. Cook, "Computer model for the simulation of printed superdirective hts spiral antennas," *Third International Conference on Computation in Electromagnetics*, pp. 332 – 337, 1996.
- [60] H. R. Ahn and I. Wolff, "General design equations, small-sized impedance transformers, and their application to small-sized three-port 3-db power dividers," *Trans of the IEEE Microwave Theory and Techniques Society*, vol. MTT-49, no. 7, pp. 1277–1288, July 2001.
- [61] H. R. Ahn, K. Lee, and N. Myung, "General design of n-way power dividers," *Microwave Theory and Techniques Symposium Digest*, 2004.
- [62] C. Hansen, R., "Fundamental limitations on antennas," *Proceedings of the IEEE*, vol. 69, no. 2, pp. 170–182, 1981.
- [63] G. Walker and C. H. O. Ramer, "Superconducting superdirectional antenna arrays," *IEEE Trans. on Antennas and Propagation*, vol. 25, no. 6, p. 885, 1977.

- [64] M. Dawoud, M., Y. Abdel-Magid, and A. Ismail, "Design and simulation of superdirective adaptive antenna arrays," *IEEE Antennas and Propagation Symposium, AP-S. Digest*, vol. 4, pp. 1700–1703, 1990.
- [65] M. M. Dawoud and A. Anderson, "Design of superdirective arrays with high radiation efficiency," *IEEE Transactions on Antennas and Propagation*, vol. AP-26, pp. 819–823, 1978.